ENGINEERING OPTICAL PROPERTIES USING PLASMONIC NANOSTRUCTURES

by

VENKATA ANANTH TAMMA

B. E., Electronics and Communication Engineering,
Visvesvaraya Technological University, 2004

M.S., Electrical Engineering,
University of Colorado Boulder, 2009

A thesis submitted to the
Faculty of the Graduate School of the
University of Colorado in partial fulfillment
of the requirement for the degree of
Doctor of Philosophy
Department of Electrical, Computer and Energy Engineering
2012

This thesis entitled:

Engineering Optical Properties using Plasmonic Nanostructures

written by Venkata Ananth Tamma

has been approved for the Department of Electrical, Computer and Energy Engineering

_____

Prof. Wounjhang Park

_____

Prof. Edward F. Kuester

Date _____

The final copy of this thesis has been examined by the signatories, and we find that both the content and the form meet acceptable presentation standards of scholarly work in the above mentioned discipline

Tamma, Venkata Ananth (Ph.D., Electrical Engineering)

Engineering Optical Properties using Plasmonic Nanostructures

Thesis directed by Prof. Wounjhang Park

Plasmonic nanostructures can be engineered to take on unusual optical properties not found in natural materials. The optical responses of plasmonic materials are functions of the structural parameters and symmetry of the nanostructures, material parameters of the nanostructure and its surroundings and the incidence angle, frequency and polarization state of light.

The scattering and hence the visibility of an object could be reduced by coating it with a plasmonic material. In this thesis, presented is an optical frequency scattering cancelation device composed of a silicon nanorod coated by a plasmonic gold nanostructure. The principle of operation was theoretically analyzed using Mie theory and the device design was verified by extensive numerical simulations. The device was fabricated using a combination of nanofabrication techniques such as electron beam lithography and focused ion beam milling. The optical responses of the scattering cancelation device and a control sample of bare silicon rod were directly visualized using near-field microscopy coupled with heterodyne interferometric detection. The experimental results were analyzed and found to match very well with theoretical prediction from numerical simulations thereby validating the design principles and our implementation.

Plasmonic nanostructures could be engineered to exhibit unique optical properties such as Fano resonance characterized by narrow asymmetrical

lineshape. We present dynamic tuning and symmetry lowering of Fano resonances in plasmonic nanostructures fabricated on flexible substrates. The tuning of Fano resonance was achieved by application of uniaxial mechanical stress. The design of the nanostructures was facilitated by extensive numerical simulations and the symmetry lowering was analyzed using group theoretical methods. The nanostructures were fabricated using electron beam lithography and optically characterized for various mechanical stress. The experimental results were in good agreement with the numerical simulations. The mechanically tunable plasmonic nanostructure could serve as a platform for dynamically tunable nanophotonic devices such as sensors and tunable filters.

To My Parents, Sister and Family.

ACKNOWLEDGMENTS

First, I would like to express my profound thanks and gratitude to my parents, sister and family. I could not have accomplished this without their support, encouragement and love. I would like to thank all my teachers and professors for teaching me all that I know.

I would like to thank my advisor Dr. Wounjhang Park for his guidance and support during my Ph.D. study.

I would like to thank Prof. Edward F. Kuester for his advice and guidance during my study at CU Boulder. I am grateful to Prof. Rafael Piestun for letting me use his lab and equipment during my thesis work. I would like to acknowledge the rest of my committee, Prof. Garret Moddel and Dr. Chris Holloway for their valuable comments and inputs.

I would like to acknowledge present and former group members and co-workers who have helped me during the course of my study. I would also like to acknowledge Prof. J. B. Lee and Kyung-hak Choi at University of Texas at Dallas for their help with fabrication and Prof. Yeshaiahu Fainman and Maurice Ayache at University of California at San Diego for their help with the setup of the heterodyne near-field scanning optical microscope.

Finally, I would like to thank my dear friends everywhere for their support and encouragement.

Table of Contents

TABLE OF FIGURES

CHAPTER I

INTRODUCTION AND BACKGROUND MATERIAL

A. Introduction

Engineered photonic structures have garnered attention worldwide due to their unusual optical properties generally unavailable in nature. Photonic crystal structures mimic crystal lattice structures and are made up of periodic obstacles where the periodicity is comparable to the wavelength of light. On the other hand, metamaterial nano-structures mimic the averaged optical response of atoms and molecules present in natural materials. Both these contrasting approaches have been used in the past to demonstrate many novel effects.

Although such artificial dielectric media were well known in the past in the microwave regime, recent advances in nanofabrication technologies have enabled the demonstration of photonic crystals and metamaterial structures in the optical regime. Initially, interest in artificial photonic structures was generated due to their promise of negative refractive index at optical frequencies. Negative refraction is an unusual phenomenon that is not observed in natural materials. It was proposed that a perfect lens made of negative index material could have the ability to achieve resolution much smaller than that obtainable with a conventional lens. In addition to negative refraction, optical invisibility cloaking is another hallmark

area of application for metamaterial structures and has attracted research attention worldwide.

Currently, research into artificial photonic nanostructures has diversified into broader areas such as sensing, next generation solar cells, efficient light generation and detection, nano-medicine, imaging and on-chip communication. Recently, huge strides have been made in understanding the optical properties of engineered plasmonic nanostructures. The extreme localization of light in metallic nanostructures generated a lot of interest in the use of plasmonic nanostructures for chemical and bio-sensing. These plasmonic nanostructures could also be used as meta-atoms to make a more complex metamaterial or plasmonic molecule to obtain engineered optical properties. Given that light-matter interactions are essentially nanoscale processes and the bulk of the electronic and vibrational processes in materials occur in the optical regime, the study of artificial photonic structures like plasmonic nanostructures could prove profitable due to their ability to control and manipulate light at the nanoscale. It is hoped that this ability could translate to better devices for the end user in terms of efficiency, cost etc.

In this dissertation work, two novel artificial photonic structures are presented along with details of their design, fabrication and characterization. First, metamaterial-based scattering cancelation structure is presented. These structures could have applications in optical invisibility cloaking and sensing. Also presented is a tunable Fano resonance in plasmonic nanostructures fabricated on flexible substrates. This structure holds tremendous promise in a wide variety of

applications including sensors, optical filters and modulators, etc. The role of symmetry in achieving tuning of the Fano resonance is discussed.

B. Maxwell's Equations

Maxwell's equations are a set of four differential equations which summarize the behavior of electromagnetic waves in nature [1]. They can be written in the following differential form

$$\nabla \cdot E = \frac{\rho}{\varepsilon_0}$$

$$\nabla \cdot B = 0$$

$$\nabla \times E + \frac{\partial B}{\partial t} = 0$$

$$\nabla \times B - \mu_0 \varepsilon_0 \frac{\partial E}{\partial t} = \mu_0 J \tag{1.1}$$

where, E and B represent the electric field intensity (in SI units of V/m) and magnetic field density (in SI units of T [Tesla]), J represents the total current density (in SI units of A/m^2) and ρ represents the total charge density (in SI units of C/m^3). ε_0 is a physical constant also known as the permittivity of free space and is approximately 8.85419×10^{-12} F/m. μ_0 is a physical constant commonly known as vacuum permeability and is exactly $4\pi \times 10^{-7}$ H/m.

It can be clearly seen from Eqn. 1.1 that all electromagnetic fields are ultimately due to charges and currents, which are also influenced by the fields. All natural materials consist of free and bound charges and hence it is expected that they both interact with electromagnetic radiation. The total charge density (ρ) and

the total current density (J) in Eqn. (1.1) contain both the bound and free terms and hence (1.1) are also commonly known as the 'microscopic' Maxwell's equations. The 'macroscopic' Maxwell's equations are obtained by considering only the free charges and currents explicitly. The differential form of (1.1) is re-cast as

$$\nabla \cdot D = \rho_f$$

$$\nabla \cdot B = 0$$

$$\nabla \times E + \frac{\partial B}{\partial t} = 0$$

$$\nabla \times H - \frac{\partial \mathrm{D}}{\partial t} = J_f \tag{1.2}$$

where, ρ_f represents the free charge density (in SI units of C/m^3), J_f represents the free current density (in SI units of A/m^3), D represents the electric displacement field (in SI units of C/m^2) and H represents the magnetic field intensity (in SI units of A/m). D and H are defined as

$$D \equiv \varepsilon_0 E + P$$

$$H \equiv \frac{B}{\mu_0} - M \tag{1.3}$$

where, P represents electric polarization density (in SI units of C/m^2) and M represents magnetic polarization density (in SI units of A/m). P and M are related to the bound charge density ρ_b and bound current density J_b by

$$\nabla \cdot P = -\rho_b$$

$$\nabla \times M = J_b \tag{1.4}$$

It must be emphasized that Eqn. (1.1) and (1.2) are the same fundamental equations written in different ways. A constitutive relation accounts for the material properties and in general is

$$D = \varepsilon E$$

$$H = \frac{B}{\mu} \tag{1.5}$$

The ε and μ in Eqn. (1.5) depend on the nature of the material and in general are functions of frequency. In addition to the differential form, Eqn. (1.1) and (1.2) can also be written in integral form. As Maxwell's equations are differential equations, boundary conditions and initial conditions need to be specified in order to obtain a unique solution. Thus, the use of Eqn. (1.2) and (1.5) in conjunction with necessary boundary and initial conditions would completely describe the electromagnetic fields in a given region of space.

From the curl relations in Eqn. (1.1) or (1.2) and for source free regions, the coupled differential Maxwell's equations are decoupled to yield two separate second order partial differential equations, one each in E and B known as the wave equations shown below

$$\nabla^2 E = \mu\varepsilon \frac{\partial^2 E}{\partial t^2} \tag{1.6a}$$

$$\nabla^2 B = \varepsilon\mu \frac{\partial^2 B}{\partial t^2} \tag{1.6b}$$

with the speed of light in the medium given by $c = 1/\sqrt{\varepsilon\mu}$.

For time-harmonic fields of the form $E = E_0 \exp(-i\omega t)$, Eqn. (1.6a) can be written as

$$\nabla^2 E + k^2 E = 0 \tag{1.7}$$

where, the wave number in the medium k = ω/c and ω is the angular frequency.

The magnitude and direction of the rate of energy transferred by electromagnetic waves as they propagate through a medium is given by the Poynting vector S = E X H with SI units of W/m^2. The Poynting vector S is an instantaneous value and most detectors including the human eye only detect the time averaged value of Poynting vector. For such cases, the averaged Poynting vector is defined for time harmonic fields as

$$< S >= \frac{1}{2} Re\{E \times H^*\} \tag{1.8}$$

where, E and H denote the complex phasor fields.

C. Absorption, scattering and extinction of light by particles

Let us consider an arbitrarily shaped object O placed in a non-absorbing medium with homogenous and isotropic dielectric constants εb and μb as shown in Fig. I-1. The object is assumed to be composed of a homogenous medium with dielectric constants ε and μ. Let us assume that the object is placed in the path of a beam of light with irradiance I and is propagating along the direction shown in Fig. I-1. We assume that the light originates at a distance far away from the object. The detector is also placed at a distance much larger than the wavelength of light in the background medium, say air.

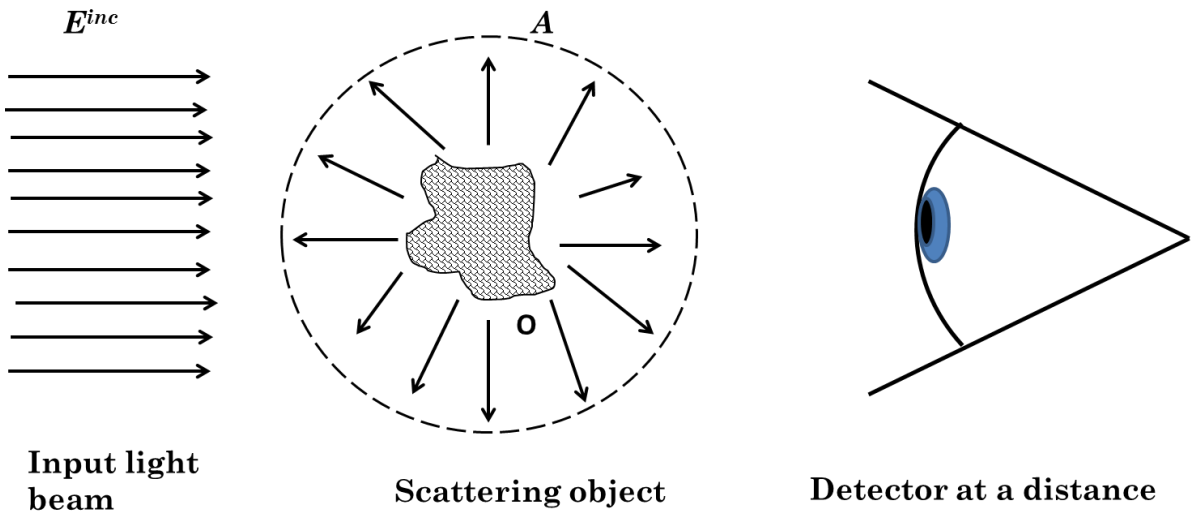

Figure I-1: Schematic showing the scattering of incident electromagnetic wave by an arbitrary object O.

The electromagnetic power received by the detector in absence of the object in all directions would be larger than the power received in presence of the object. Here, we do not consider objects such as optical lenses or metallic focusing elements that focus energy to a small volume. Therefore the presence of the object causes *extinction* of the incident beam as seen at the detector. This difference in power flow is accounted for by the power *absorbed* by the object and power *scattered* by the object in all directions. The optical *extinction* by the object depends on the size, shape and orientation of the object, dielectric properties of the object (arising from either structural or chemical composition), the dielectric properties of the surrounding medium and the polarization state and frequency of the incident light beam. To quantify the absorption, scattering and extinction of light by an object, an imaginary sphere of radius r (radius larger than object size) and surface A is

constructed around the object. The total electric field could be expressed as a sum of the incident and scattered field and similarly for the magnetic field.

$$E_{total} = E_{inc} + E_{scatt}$$

$$H_{total} = H_{inc} + H_{scatt} \tag{1.9}$$

Therefore the rate of energy extinction could be written as a sum of the energy absorption rate and energy scattering rate.

$$W_{ext} = W_{abs} + W_{scatt} \tag{1.10}$$

where,

$$W_{abs} = \int_V \frac{1}{2} Re\{\sigma(\omega) E \cdot E^* - j\omega E \cdot D^*\} d$$

$$W_{scatt} = \int_A S_{scatt} \cdot \hat{e}_r dA \tag{1.11}$$

where $\hat{\boldsymbol{e}}_{\boldsymbol{r}}$ is the unit outward radial normal to the surface A of the imaginary sphere. σ(ω) is the AC conductivity of the material composing the object and V is the volume of the object. The time averaged scattered power is given by

$$< S_{scatt} >= \frac{1}{2} Re\{E_{scatt} \times H^*_{scatt}\} \tag{1.12}$$

The absorption, scattering and extinction cross-sections (units of m^2) are given by

$$C_{abs} = \frac{W_{abs}}{I} = \frac{\int_V \frac{1}{2} Re\{\sigma(\omega) E \cdot E^* - j\omega E \cdot D^*\} dV}{I} \tag{1.13a}$$

$$C_{scatt} = \frac{W_{scatt}}{I} = \frac{\int_A S_{scatt} \cdot \hat{e}_r dA}{I} \tag{1.13b}$$

$$C_{ext} = C_{abs} + C_{scatt} \tag{1.13c}$$

Scattering of light by particles is a very important problem in electromagnetics as light scattering is a fundamental physical process in nature and further details can be found in [2, 3].

The artificial electromagnetic structures presented in this thesis: scattering cancelation device and plasmonic nanostructures, are well characterized by their cross-sections. Therefore, most of the numerical simulations performed in this thesis were devoted to computing the absorption, scattering and extinction cross-sections for the scattering cancelation device and plasmonic nanostructures. The Eqns. (1.13) were used to obtain the various cross-sections from the field data exported from simulations. The simulations used to compute the cross-sections were performed by the finite-element method using the commercial code COMSOL V3.5a.

D. Optical properties of materials

The formulation of Maxwell's equations presented in Eqn. (1.1) to (1.5) makes it abundantly clear that the macroscopic (bulk) optical properties are a consequence of microscopic charges and currents, both free and bound. The macroscopic optical constants of materials have been extensively measured at various frequency ranges and tabulated [4]. In the classical model developed to explain the optical properties of materials, a medium consisting of atoms and molecules is represented as a collection of different types of oscillators, each with their own characteristic resonance frequency [5]. The oscillator model was first introduced by Henrik Lorentz on the assumption that a negative charge (electron) is held in stable orbit around a positive charge (nucleus). The mass of the nucleus (M) is assumed to be

much larger than that of the electron (m). The reduced mass of the system (M_r) is the harmonic mean of M and m and M_r ~ m as M >> m. Physically, an incident oscillating electric field would cause oscillations of the atomic dipole. The nucleus due to its larger mass is assumed to be stationary whereas the lighter electron oscillates back and forth about its equilibrium position at the frequency of the incident light. Thus the oscillating electron and fixed nucleus constitute an oscillating dipole which re-radiates the field with a time/phase lag. This time/phase lag is further characterized in terms of the refractive index of the medium. Lorentz modeled the displacement of atomic dipoles as harmonic oscillators with damping. The damping was introduced to account for any losses that may be present in the system. The Lorentz model for dielectrics predicts the frequency dependent permittivity function as

$$\varepsilon(\omega) = \varepsilon_\infty + \frac{Ne^2}{\varepsilon_0 m_r} \frac{1}{(\omega_0^2 - \omega^2 - i\gamma\omega)} \tag{1.14}$$

where, $\varepsilon_\infty = \varepsilon(\omega = \infty)$ is the high frequency response of the medium, N is the number of dipoles per unit volume or the atomic density, m_r is the reduced mass of the system and e is the charge associated with the electron. γ is the damping rate and characterizes the rate of energy loss from the oscillator. ω_0 is the resonant frequency corresponding to one of the many natural frequencies of the atom (corresponding to frequencies of atomic transition) and is proportional to

$$\omega_0 \propto \sqrt{\frac{K}{m_r}} \tag{1.15}$$

where K is the Coulomb restoring force between the nucleus and the electron and m_r is the reduced mass of the system.

The classical Lorentz oscillator model can predict the optical dielectric function of materials very accurately. As the reduced mass of bound electron system is approximately the mass of an electron and hence very small, it can be expected that the optical responses due to bound electrons occur at the ultra-violet and visible frequency ranges. Since atoms absorb and emit light at multiple discrete transition frequencies, it can be expected that the dielectric function includes contributions from multiple oscillators. In the case of multiple oscillators, Eqn. (1.14) is modified as

$$\varepsilon(\omega) = \varepsilon_\infty + \frac{Ne^2}{\varepsilon_0 m_r} \sum_j \frac{f_j}{(\omega_{0j}^2 - \omega^2 - i\gamma_j \omega)} \tag{1.16}$$

where, ω_{0j} and γ_j are the frequency and damping associated with discrete transition j. f_j is the oscillator strength for transition j.

Vibrational oscillators too can be modeled using the Lorentz oscillator model. Vibrational oscillators are different from bound electron oscillators as they arise from the oscillations of atoms and ions. Vibrational oscillators typically occur in ionic crystals and polar molecules which contain oppositely charged ions. An oscillating dipole is produced when these ions vibrate from their equilibrium positions leading to an optical response. Since the atoms and ions have much larger mass than electrons, it can be expected that the reduced mass of such a system would be larger than the bound electron system. Hence, optical responses due to

vibrational oscillators tend to occur at lower frequencies falling in the infrared region of the optical spectrum.

The optical response due to free electrons could be modeled by modifying the Lorentz oscillator model. In metals and doped semiconductors, the free electrons make dominant contributions to the optical properties. For free electrons, the restoring force between nucleus and free electron, $K = 0$, and thereby the resonance frequency ω_0 is also zero. Hence, Equation (1.14) is re-cast as

$$\varepsilon(\omega) = 1 - \frac{\omega_p^2}{(\omega^2 + i\gamma\omega)} \tag{1.17}$$

where, ω_p is known as the plasma frequency and γ the damping rate and

$$\omega_p = \sqrt{\frac{Ne^2}{\varepsilon_0 m}} \tag{1.18}$$

This model is known as the Drude-Lorentz model and explains the high reflectivity of metals at optical frequencies. Typically, for a metal N is on the order of 10^{28} m^{-3} and this leads to the plasma frequency to occur in the ultra-violet regime. In the work presented in this thesis, gold has been extensively used to fabricate plasmonic metamaterial structures. Fig. I-2 compares the experimentally measured complex dielectric constants of gold with those obtained from the Drude-Lorentz model (here and elsewhere in this thesis, the relative dielectric constant is to be understood). Gold is a noble metal with valency of 1 and electron density of ~5.9×10^{28} m^{-3} giving a plasma frequency, $\omega_p/2\pi \sim 2.18 \times 10^{15}$ Hz. The damping rate, $\gamma/2\pi$ is roughly 4.35×10^{12} Hz. These parameters were used to compute the dielectric

response using the Drude-Lorentz model. The experimental values were extracted from the data tabulated in [6].

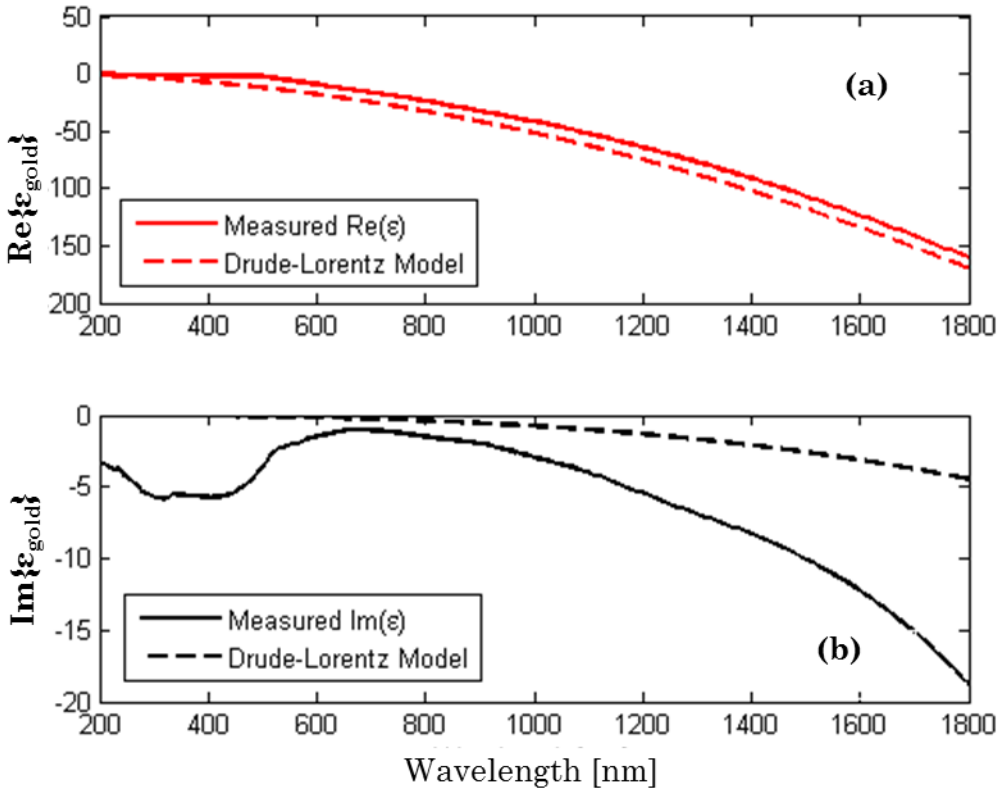

Figure I-2: Comparison of (a) real part and (b) imaginary part of gold dielectric function between measured data from Ref. 6 and Drude-Lorentz model.

The Drude-Lorentz model is a good approximation to the experimental data at frequencies well below the plasma frequency, and the metal behaves like a perfect electric conductor at microwave and radio frequencies. In the visible region, the metal becomes lossy due to inter-band transitions and this causes the measured data to deviate from the model based on a purely free electron system. At frequencies higher than the plasma frequency the metal becomes transparent and

behaves like a lossy dielectric material in accordance with the Lorentz-Drude model.

It can be observed from Fig I-2 (a) that the Re{ε} obtained using Drude-Lorentz model agrees reasonably with experimental data. However, the experimentally measured Im{ε} plotted in Fig. I-2 (b) deviates widely from the theoretical predictions. This is because the simple Drude-Lorentz model fails to account for inter-band transitions in gold. It is however possible to account for interband transitions and obtain an exact fit to the experimental data using multiple Lorentz oscillator terms in addition to the Drude-Lorentz term. Ref. [7] models optical functions for several commonly used plasmonic materials such as gold, silver and copper among others by use of additional Lorentz oscillator terms. Therefore, it would be advisable to use the experimentally measured permittivity values of gold for all nanophotonics applications. In all the numerical modeling work presented in this thesis, the complex dielectric constants of gold used were obtained from the experimentally measured data tabulated in [6].

E. Optical near-field characterization

In conventional optical microscopy, the object under inspection is imaged using a lens system which acts as a low-pass spatial frequency filter. The higher spatial frequency information of the object is lost during the near-field ($d < \lambda$) to far-field ($d >> \lambda$) transformation of light. This is the fundamental reason behind the diffraction limit that imposes a lower bound on achievable spatial resolution in conventional optical microscopy [8, 9]. The high-frequency spatial information of the object is

carried by evanescent waves which spatially decay very rapidly in the vicinity of the object. It was proposed by Synge in 1928 that a subwavelength aperture in metal could be brought close to the object to collect the near-field information thereby improving the optical resolution [10] and the theory behind the idea was later confirmed [11]. Synge's idea was not immediately implemented due to technological challenges faced in placing a subwavelength aperture in the vicinity (<10 nm) of the object. The concept was demonstrated at microwave frequencies for λ=3 cm with λ/60 resolution [12]. It was only in 1984 that this concept was demonstrated at optical frequencies [13, 14], and the technique is now known as scanning near-field optical microscopy (SNOM) or near-field scanning optical microscopy (NSOM). A review of the theoretical background and technological details of NSOM are detailed in [15].

Synge's idea was to use an aperture of diameter 100 nm in a metal film to probe the near-field of the object. Practically, the idea is implemented by milling a small subwavelength aperture in a metal coated tapered optical fiber probe. The probe is then brought into very close proximity (<10 nm) to the surface of the sample under investigation using a piezo driver under feedback (see [15]). The tapered optical fiber is fabricated either by pulling under heat [16] or chemical etching [17]. The probes are then coated with metal (usually gold, silver or aluminum) and subwavelength apertures of diameters > 50 nm are milled in the metal layer by use of a focused ion beam milling machine. The tapered probe is then mounted on a tuning fork probe mount. Optical microscope images and scanning electron micrographs (SEM) of some aperture probes are shown in Fig. I-3. Fig. I-3 (a) shows the optical microscope image of a tuning fork mount with the bent tapered

metalized probe below the tuning fork. Fig. I-3 (b) shows a higher magnification image of the bend in the tapered optical probe with red light emitted from the tip of the probe. Fig. I-3 (c) shows the SEM image of the tip of a metalized probe with a 50 nm aperture and Fig. I-3 (d) shows the shows the SEM image of the tip of a metalized probe with a 110 nm aperture. Due to the small aperture size, the NSOM probe typically has a wavelength dependent collection efficiency in the order of 10^{-5} to 10^{-6} and therefore control over the aperture size is critical [18].

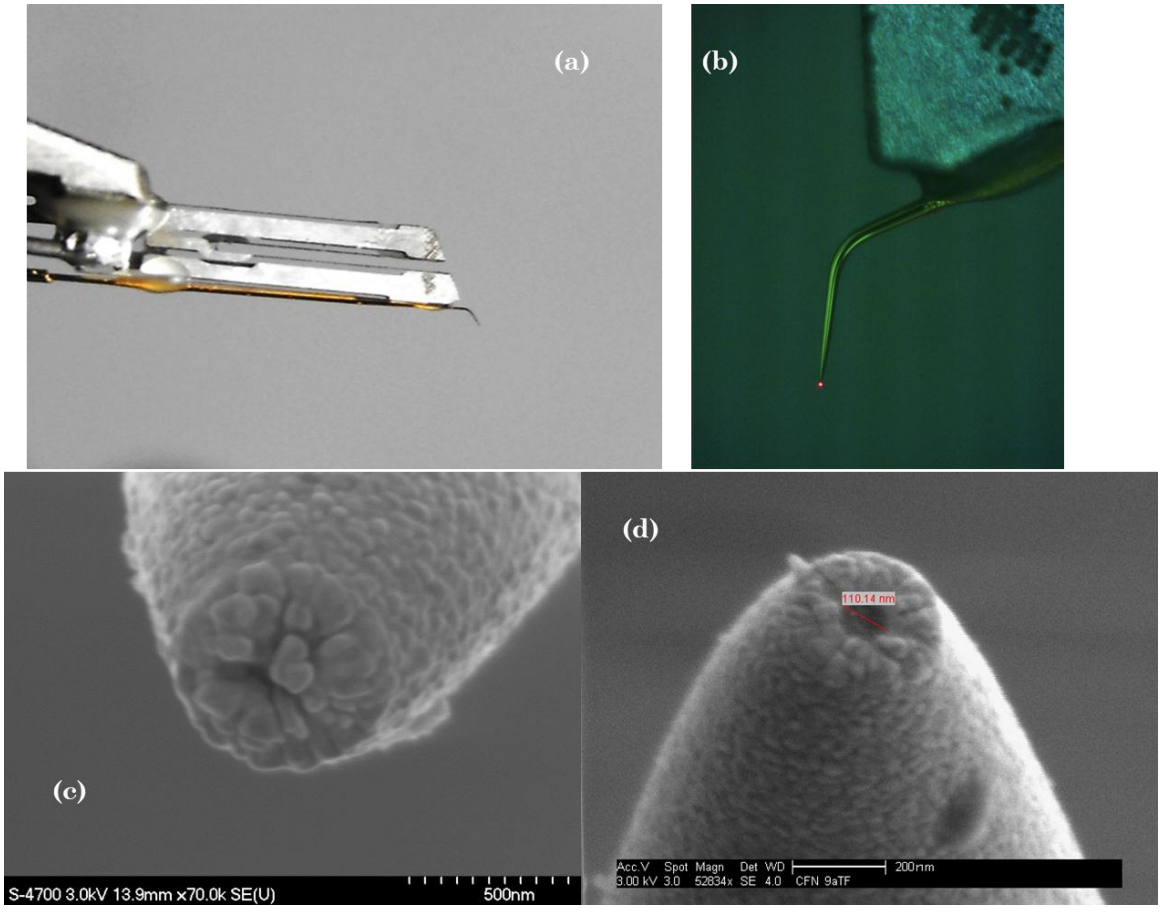

Figure I-3: Optical and SEM images of NSOM probes mounted on tapered metalized optical fibers. The bend in the fiber can be clearly seen in (a) and (b). Images (c) and (d) show the apertures at the tip of the probe.

The NSOM can be operated in multiple modes as detailed in Fig. I-4. The three basic modes: illumination, collection and reflection are illustrated in Figs. I-4 (a, b and c) respectively.

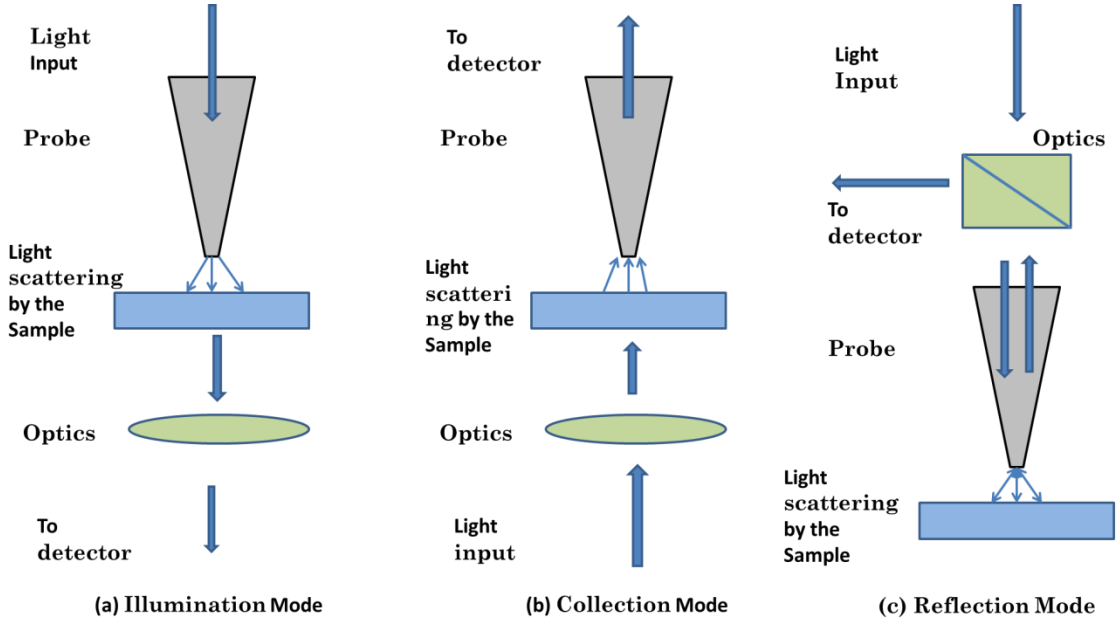

Figure I-4: Schematic showing the various operating modes of the NSOM. (a) Illumination mode (b) collection mode and (c) reflection mode

Many other modes are possible, but they would be a combination or variation of the three basic modes of operation. Fig I-4 (a) details the illumination mode which was the original mode of operation proposed by Synge. The NSOM probe is used to illuminate the sample and the scattered light is collected in the far-field. Fig. I-4 (b) shows the setup for collection mode. The sample is illuminated with light and the scattered light is collected by the NSOM probe. This method also works for photonic crystal or metamaterial samples like the scattering cancelation device sample presented later in the thesis. We typically operate the NSOM in the collection mode.

Fig. I-4 (c) shows the setup for NSOM operation in reflection mode and is similar to operation in illumination mode.

In any mode of operation, the probe is brought into contact with the sample and the sample is scanned point-by-point in a raster scan or in a free-form scan depending on the application. The tuning fork mount is a popular method to control the motion of the NSOM probe. The arrangement of the probe on the mount is clearly shown in Figs. I-3 (a, b). When the probe is brought in contact with the sample, the spacing between the probe and sample is very small (<10 nm). At these distance scales, the atomic forces play an important role and these separation dependent forces could be either attractive or repulsive. By monitoring the frequency and phase of the tuning fork in a feedback loop, the NSOM probe can be well controlled using dedicated hardware and software.

A heterodyne near-field scanning optical microscope (H-NSOM) setup was used in the experiment presented in the thesis. The H-NSOM enhanced the capability of the traditional NSOM by addition of heterodyne interferometric detection. The H-NSOM was built around the commercial NSOM head Multiview 2000 from Nanonics Imaging, Israel [19]. Briefly, the Multiview 2000 has two computer controlled 3-axis stages which allow for independent position control of the sample and the probe. The sample is placed on the bottom scanner (3-axis stage) and the probe is fixed to the top scanner. The NSOM probes used in the experiments were manufactured by Nanonics and optical and SEM images of some representative probes are shown in Fig. I-3. The tapered optical fiber was manufactured by pulling

an optical fiber under heat. Later, the fiber was bent and chromium (adhesion layer) and gold metal layers were coated by evaporation. Focused ion beam milling was used to create the apertures at the tip of the probe. The probe was then mounted onto the tuning fork mount. The Lab view based control software NanoWorkShop V1760 was used to control the piezo drivers which determine the position of the probe.

The NSOM setup was connected into an arm of an all fiber Mach-Zehnder interferometer to enable heterodyne detection of the signals. A schematic of the H-NSOM is shown in Fig. I-5.

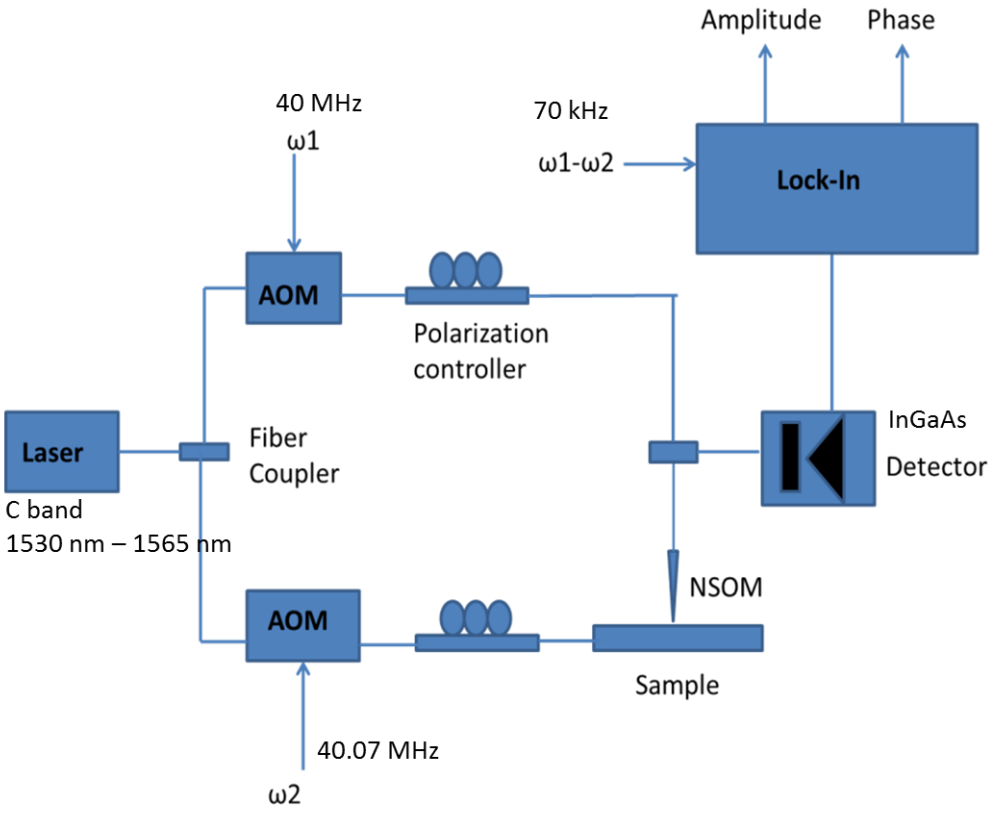

Figure I-5: Schematic of the H-NSOM system used for optical characterization of photonic structures.

The H-NSOM setup was designed to operate at the telecom wavelength of 1550 nm. The bandwidth of the H-NSOM is limited by the bandwidths of the optical elements in the interferometer. The input light from a laser (C-band: 1530 nm to 1565 nm) was fed to a 90/10 fiber coupler which then branched out into the two arms of the interferometer. Both the arms were loaded with an Acousto-Optic Modulator (AOM) and polarization paddle. In our setup, ω_1 = 40 MHz and ω_2 = 40.070 MHz giving a difference frequency of 70 kHz. The signal arm of the interferometer also included the NSOM and received 90% of the input light power.

The output of the NSOM probe was directly connected to a 99/1 fiber coupler whose other input was connected to the reference arm. The reference arm was connected to the 1 % input of the fiber coupler. The output of the fiber coupler was then connected to an InGaAs detector. The output of the detector was connected to a Lock-in amplifier (Stanford Research Systems SR530) which was also fed with the difference signal generated by an RF mixer. The lock-in then outputted two voltage signals which were proportional to the amplitude of the measured optical signal and the relative phase of the measured signal in relation to the reference signal. The analog outputs of the lock-in and the feedback data (topology) were then converted into digital form and inputted into a computer for further analysis.

The use of heterodyne interferometric detection has many advantages. First, normal detectors respond to the time averaged Poynting vector (proportional to $|E|^2$) and thereby phase information is lost. However, using the interference phenomenon, the phase information can be embedded in the amplitude term of the

total interference signal. Hence, the heterodyne interferometry technique could be used to obtain both the phase and amplitude (|E|) information. The Mach-Zehnder interferometry setup was implemented entirely using optical fibers. This made the setup sensitive to thermal currents. Therefore, to ensure the stability of the interferometry setup, the entire H-NSOM setup including the NSOM head was placed in custom built plastic boxes.

The main advantage of the heterodyne system is the improvement of the signal to noise ratio of the optical signal due to the use of a lock-in. The lock-in essentially behaves as a very high gain amplifier. In H-NSOM setup, the weak signal collected from the probe is interfered with a strong reference signal. The signal information is now encoded into the amplitude variations of the interference signal. The total signal gain is approximately given by $\sqrt{|E_{ref}|/|E_{signal}|}$, where, $|E_{ref}|$ is the amplitude of reference and $|E_{signal}|$ is the signal amplitude. The gain could be large as the signal power is typically in the nW range and the reference power could be much higher (in the mW range).

CHAPTER II

SCATTERING CANCELATION DEVICE

A. Introduction

Invisibility cloaking devices have a long history of enthralling aficionados of fantasy and science fiction. Recent advances in metamaterial technology and nanofabrication techniques have helped realize invisibility cloaking devices with an eye towards practical applications. Despite being in a nascent stage, scientific literature on invisibility cloaking devices, both electromagnetic and acoustic, has grown by leaps and bounds. Recently, a variety of invisibility cloaking devices designed using different approaches have been explored. In particular, electromagnetic invisibility cloaking devices designed using techniques such as transformation optics [20-23], scattering cancelation [24, 25], transmission line networks [26, 27] and anomalous resonances [28-30] have been proposed at both microwave and optical frequencies. Despite the variation in techniques, all electromagnetic invisibility cloaking devices attempt to render the cloaked object invisible to electromagnetic radiation over a finite frequency bandwidth by suppressing the scattered fields produced by the object in all directions with zero or minimal power absorbed by the cloaking device itself.

Recently, transformation optics has been used to design and demonstrate a variety of metamaterial based invisibility cloaks [20-23]. Invisibility cloaks designed

using transformation optics have the ability to cloak large objects with sizes much larger than the wavelength and are practically insensitive to the shape and dielectric constants of the object to be cloaked. Although transformation optics has proved to be a powerful design tool, its requirement of anisotropic materials with extreme values of optical constants places makes it difficult to implement using the metamaterial structures. Subsequently, a new cloak design was proposed to hide objects in front of a mirror plane [31]. This ground plane cloak was designed using a non-Euclidean conformal mapping technique and required a modest range of optical constants with minimal anisotropy making it highly suitable for implementation at optical frequencies [32]. Many groups have demonstrated two-dimensional (2D) implementations of the ground plane cloak at optical frequencies [33-35]. In addition, using near-field microscopy, it was demonstrated that the operational bandwidth of such 2D implementations was limited by waveguide dispersion thereby restricting the inherent broadband behavior expected from the original design using transformation optics [36]. In this regard, a generally applicable technique was suggested to extend the bandwidth of such 2D implementations by conformal deposition of a dielectric layer. Recently, three-dimensional (3D) implementations of the ground plane cloak have been demonstrated at both microwave [37] and optical frequencies [38, 39]. In addition, the intrinsic anisotropy in certain uniaxial crystals was also used to demonstrate three-dimensional cloaking at visible frequencies [40, 41].

In contrast to the invisibility cloaks designed using transformation optics, the cloaks designed using the scattering cancellation technique are highly dependent on the shape and dielectric properties of the object to be cloaked and typically the entire structure has to be smaller than the wavelength. Previously, the concept of scattering cancellation has been applied to invisibility cloaks [24, 42, 43] and minimal scattering antennas [44]. Also, artificial electromagnetic surfaces have been used to reduce forward scattering from cylindrical objects [45]. However, the recent spurt of scholarly interest in metamaterials and plasmonic materials has led to a renewed interest in scattering cancellation technique applied to invisibility cloaking. Recently, it was shown that the scattering cross-section of spherical and cylindrical objects could be drastically reduced when covered with plasmonic and metamaterial coatings [25, 46]. In particular, it was shown that the dominant dipolar contribution to the scattering from a spherical or cylindrical dielectric objects could be canceled out when coated by a layer of material with negative or very low values of real part of permittivity. Also, the higher order multipole contributions could be suppressed albeit at the cost of design complexity.

Later, the theory was extended from isolated spherical or cylindrical objects to collections of closely spaced particles with sizes larger than the wavelength [47]. Although this technique is inherently non-resonant, the operational bandwidth of objects covered by a single layer of plasmonic material is limited by the dispersion of the plasmonic cover. It was shown that the operational bandwidth could be extended by use of multiple layers of plasmonic covers [48]. Recently, cylindrical

objects coated with plasmonic covers were studied under broadband non-monochromatic illumination and the cloak performance was evaluated [49]. Also, the scattering cancellation technique has been extended to study plasmonic cloaking of irregularly shaped objects with anisotropic scattering properties [50]. It has also been theorized that instead of covering an object with a plasmonic cloak, similar scattering reduction could be obtained by surrounding the object with suitably designed discrete satellite plasmonic scatterers making the entire system of particles invisible to an observer [51].

Potential applications for plasmonic cloaking have included cloaked sensors and antennae [52, 53], cloaked near-field probes [54, 55] and reduction of optical forces exerted on plasmonic cloaks [56]. It has been proposed to use parallel plate metamaterial structures to achieve plasmonic cloaking at microwave frequencies [57] and the concept has been extended to infrared and optical frequencies [58]. Recently, plasmonic cloaking of a cylindrical object using parallel plate metamaterials in two-dimensional waveguide geometry was experimentally demonstrated at microwave frequencies [59]. More recently, plasmonic cloaking of a finite cylindrical object in free space was experimentally demonstrated at microwave frequencies [60]. At optical frequencies, the proposed methods to achieve plasmonic cloaking include the use of metamaterial inclusion based cylindrical cloaks for TE and TM polarization [61], concentric shells made up of thin layers of different materials as a plasmonic cover around a spherical or cylindrical object

[62], and the use of a shell of nanoparticles to surround a spherical or cylindrical object [63, 64].

Presented in this chapter is an experimental demonstration of scattering reduction by use of plasmonic covers at optical frequencies. A cylindrical object was designed to be reduced scattering at 1550 nm by a plasmonic cover made up of gold grating structure. The structure was fabricated using a combination of electron beam lithography and focused ion beam milling. The optical responses at 1550nm of the structure as well as a control bare cylinder with no plasmonic cover were directly visualized using a heterodyne near-field scanning optical microscope (H-NSOM). The measured characteristics were found to agree well with the simulated results thereby validating the design principle and the present implementation.

B. Theoretical background: Scattering by infinite dielectric cylinder

The scattering cancellation theory could be applied to reduce the scattering cross-section of small objects. This could be achieved by covering the object with single or multiple layers of plasmonic materials. The permittivity and thickness of the cover are designed such that they scatter out of phase with the dielectric object. This is due to the opposite dipole moments induced in the cover and the object that cancel each other resulting in reduced scattering leading to reduced visibility of the object. A very simple heuristic analysis of the scattering cancelation phenomenon was presented in [25] and is re-drawn in Fig. II-1 below.

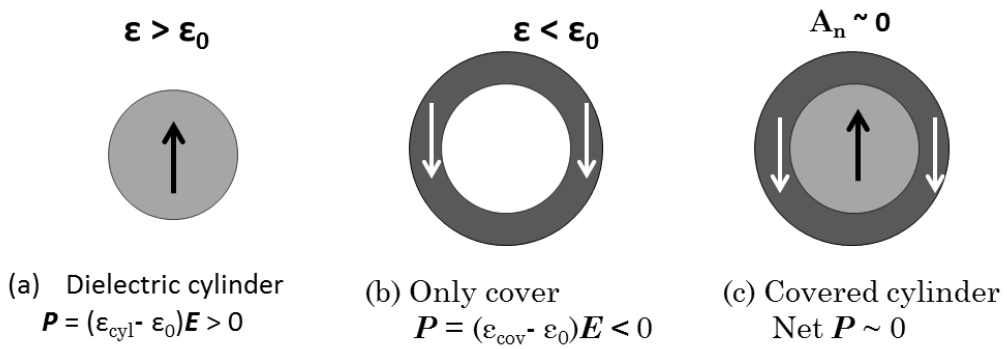

Figure II-1: Schematic describing the heuristic analysis of the scattering reduction phenomenon by use of plasmonic covers. The white and black colored arrows show the dipole moments induced in the cover and object respectively. For suitable values of cover thickness and permittivity, these opposing dipoles cancel out each other rendering the object invisible.

In the heuristic analysis presented in Fig. II-1, we use quasi-static approximation and assume identical incident field conditions in all cases. An incident exciting field induces a local polarization $\boldsymbol{P}$ in the dielectric cylinder. When integrated over the volume of the cylinder, the polarization yields a dipole moment which consequently causes scattering. Under identical incidence conditions, the cover would show a local polarization field which is opposite in direction to that induced in the cylinder. When the cylinder and cover are combined, we can then expect that the dipole moment induced in the cylinder cancels the moment induced in the cover thereby reducing the scattering of the combined system.

Scattering by spherical and cylindrical objects are canonical problems in electromagnetic scattering theory, as exact solutions to Maxwell's equations can be directly obtained [2, 3]. Initial solutions to scattering of light by spherical objects

(easily extended to infinite cylinders) were obtained by Ludvig Lorenz and Gustav Mie and hence known as the Lorenz-Mie solution to Maxwell's equations. Exact solutions to Maxwell's equations could also be obtained for stratified/coated spheres and infinite cylinders. Since the scattering cancelation theory proposed to reduce scattering of an electrically small object by coating it with single or multiple layers of plasmonic materials, it can expected that exact solutions to the present design problem could be obtained by application of Lorenz-Mie theory. The possibility of achieving reduced visibility by use of such coatings was theoretically predicted in the past [2, 24] (See Ref. 2, Page 149, Eqn. 5.36).

A brief discussion of the scattering by an infinite dielectric cylinder coated by a thin layer of homogenous material is presented below. The structure and field polarizations under consideration are shown in Fig. II-2. The problem is divided into three regions with Region I representing the homogenous background medium with permittivity ε_1, Region II representing the homogenous dielectric cover with permittivity ε_2 and Region III representing the homogenous dielectric medium composing the cylinder with permittivity ε_3. In all cases, the material is assumed to be non-magnetic ($\mu = \mu_o$), as most materials are non-magnetic at optical frequencies. In the i^{th} region, the wavenumber k_i is related to angular frequency ω by the dispersion relation $k_i^2 = (\omega/c)^2\varepsilon_i$ where ε_i is the permittivity function associated with that region.

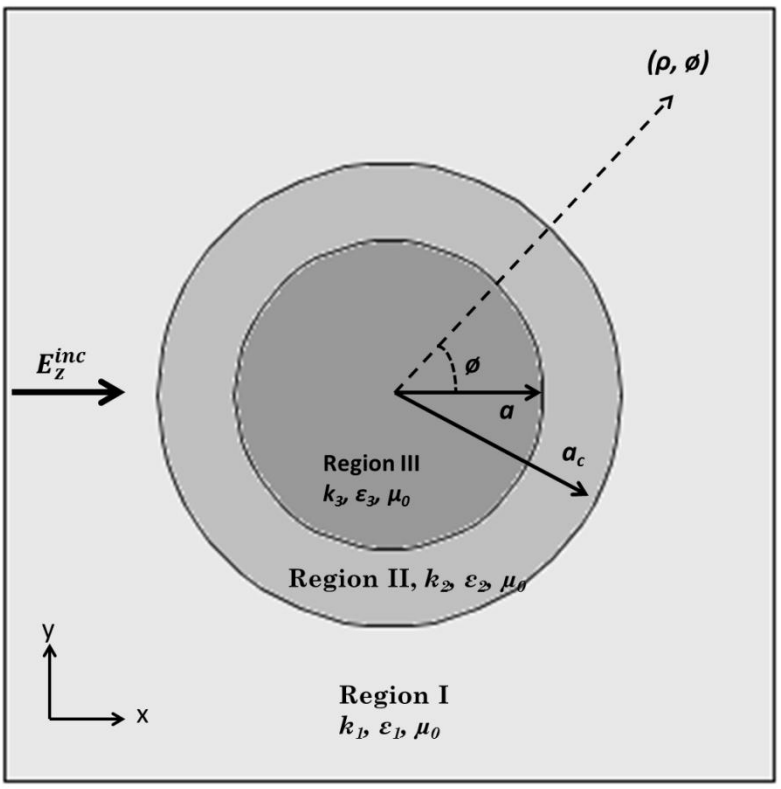

Figure II-2: Schematic showing the structure and field orientations for the analytical solution. A cylindrical object with radius a and permittivity ε_3 is coated with a cover of thickness (a_c-a), where ac is the total radius of the cylinder with plasmonic cover. The cover permittivity is ε_2 and the background medium has a permittivity ε_1.

The input electric field is polarized along the z direction (parallel to the axis of the infinite cylinder) and is denoted as the transverse magnetic (TM) polarization. In the following, the time dependence $e^{i\omega t}$ is assumed throughout.

An input plane wave in region I can be expanded into cylindrical harmonics as

$$E_{z,1}^{inc} = E_0 \sum_{n=-\infty}^{\infty} i^n J_n(k_1\rho) e^{in\varphi} \tag{2.0}$$

Let $E_{z,i}^{scatt}$ be the scattered field in the i^{th} region. Then both $E_{z,1}^{inc}$ and $E_{z,i}^{scatt}$ satisfy the wave equation in the i^{th} region.

$$\nabla^2 E_z + k_i^2 E_z = 0 \tag{2.1}$$

Solving the above equation in the three regions yields general solutions as follows.

In Region I,

$$E_{z,1}^{scatt} = E_0 \sum_{n=-\infty}^{\infty} i^n A_n H_n^1(k_1\rho) e^{in\varphi} \tag{2.2}$$

in Region II,

$$E_{z,2}^{scatt} = E_0 \sum_{n=-\infty}^{\infty} i^n \{B_n H_n^2(k_2\rho) + C_n H_n^1(k_2\rho)\} e^{in\varphi} \tag{2.3}$$

and in Region III,

$$E_{z,3}^{scatt} = E_0 \sum_{n=-\infty}^{\infty} i^n D_n J_n(k_3\rho) e^{in\varphi} \tag{2.4}$$

Here J is the Bessel function of the first kind and H^1 and H^2 are Hankel functions of the first and second kind, respectively. Once the electric fields are determined, the magnetic fields can be obtained by using the Maxwell's equations in time-harmonic form

$$H = \frac{-i}{\omega\mu_0} \nabla \times E \tag{2.5}$$

Application of the boundary conditions at $\rho = a$ and $\rho = a_c$ for both the electric and magnetic field components yields the following set of linear equations

$$\begin{bmatrix} H_n^1(k_1a_c) & -H_n^2(k_2a_c) & -H_n^1(k_2a_c) & 0 \\ k_1H_n^{1'}(k_1a_c) & -k_2H_n^{2'}(k_2a_c) & -k_2H_n^{1'}(k_2a_c) & 0 \\ 0 & H_n^2(k_2a) & H_n^1(k_2a) & -J_n(k_3a) \\ 0 & k_2H_n^{2'}(k_2a) & k_2H_n^{1'}(k_2a) & -k_3J_n'(k_3a) \end{bmatrix} \begin{bmatrix} A_n \\ B_n \\ C_n \\ D_n \end{bmatrix} = \begin{bmatrix} -J_n(k_1a_c) \\ -k_1J_n'(k_1a_c) \\ 0 \\ 0 \end{bmatrix} \tag{2.6}$$

As we are interested in the behavior of the scattered field in Region I (background medium), we proceed to find only A_n using the determinant method.

$$A_n = \frac{\begin{vmatrix} -J_n(k_1a_c) & -H_n^2(k_2a_c) & -H_n^1(k_2a_c) & 0 \\ -k_1J_n'(k_1a_c) & -k_2H_n^{2'}(k_2a_c) & -k_2H_n^{1'}(k_2a_c) & 0 \\ 0 & H_n^2(k_2a) & H_n^1(k_2a) & -J_n(k_3a) \\ 0 & k_2H_n^{2'}(k_2a) & k_2H_n^{1'}(k_2a) & -k_3J_n'(k_3a) \end{vmatrix}}{\begin{vmatrix} H_n^1(k_1a_c) & -H_n^2(k_2a_c) & -H_n^1(k_2a_c) & 0 \\ k_1H_n^{1'}(k_1a_c) & -k_2H_n^{2'}(k_2a_c) & -k_2H_n^{1'}(k_2a_c) & 0 \\ 0 & H_n^2(k_2a) & H_n^1(k_2a) & -J_n(k_3a) \\ 0 & k_2H_n^{2'}(k_2a) & k_2H_n^{1'}(k_2a) & -k_3J_n'(k_3a) \end{vmatrix}} \tag{2.7}$$

The total field in Region I is given by the sum of incident field and scattered field in region I as

$$E_{z,1}^{tot} = E_0 \sum_{n=-\infty}^{\infty} i^n \{J_n(k_1\rho) + A_nH_n^1(k_1\rho)\}e^{in\varphi} \tag{2.8}$$

In order to achieve scattering cancelation, we want the scattered field in region I to vanish

$$E_{z,1}^{scatt} = E_0 \sum_{n=-\infty}^{\infty} i^n A_nH_n^1(k_1\rho)e^{in\varphi} = 0 \tag{2.9}$$

This is possible if $A_n = 0$ for some n at a certain frequency. This means that the numerator in Eqn. (2.7) must be zero for certain values of n

$$\begin{vmatrix} -J_n(k_1a_c) & -H_n^2(k_2a_c) & -H_n^1(k_2a_c) & 0 \\ -k_1J_n'(k_1a_c) & -k_2H_n^{2'}(k_2a_c) & -k_2H_n^{1'}(k_2a_c) & 0 \\ 0 & H_n^2(k_2a) & H_n^1(k_2a) & -J_n(k_3a) \\ 0 & k_2H_n^{2'}(k_2a) & k_2H_n^{1'}(k_2a) & -k_3J_n'(k_3a) \end{vmatrix} = 0 \tag{2.10}$$

A_n can easily be evaluated numerically for various parameter values. Once A_n is obtained, then we can numerically obtain the total field in Region I.

The scattering cross-section of the entire structure is obtained using

$$C_{scatt} = \frac{2}{k_1}\left[|A_0|^2 + 2\sum_{n=0}^{\infty}|A_n|^2\right] \tag{2.11}$$

The A_0 coefficient corresponds to the n=0 or dipolar term. For subwavelength particles, it is expected that the dipolar term dominates over the higher order terms.

We study the effect of scattering reduction at λ = 1 m by analyzing the various the A_n coefficients as functions of cover thickness for a bare cylinder of radius 5 cm in the air background medium and for the same cylinder coated with a plasmonic material of different permittivity. The summation in Eqn. (2.11) was terminated when the error in scattering cross-section was < 1 % after multiple summations and this generally corresponded to 4 terms in the summation. In the Figs. II-3 (a-c), we plot $|A_n|$ for n = 0, 1 and 2 as a function of the cover thickness. The y axis has been plotted in logarithmic scale to include the n=1 and n=2 terms. The uncoated cylinder case is plotted in Fig. II-3 (a) and the A_n coefficients are constant throughout as expected. Fig. II-3 (b, c) plots the response of the A_n coefficients when the cylinder is coated with a cover of permittivity of -2 and -8, respectively, with no loss.

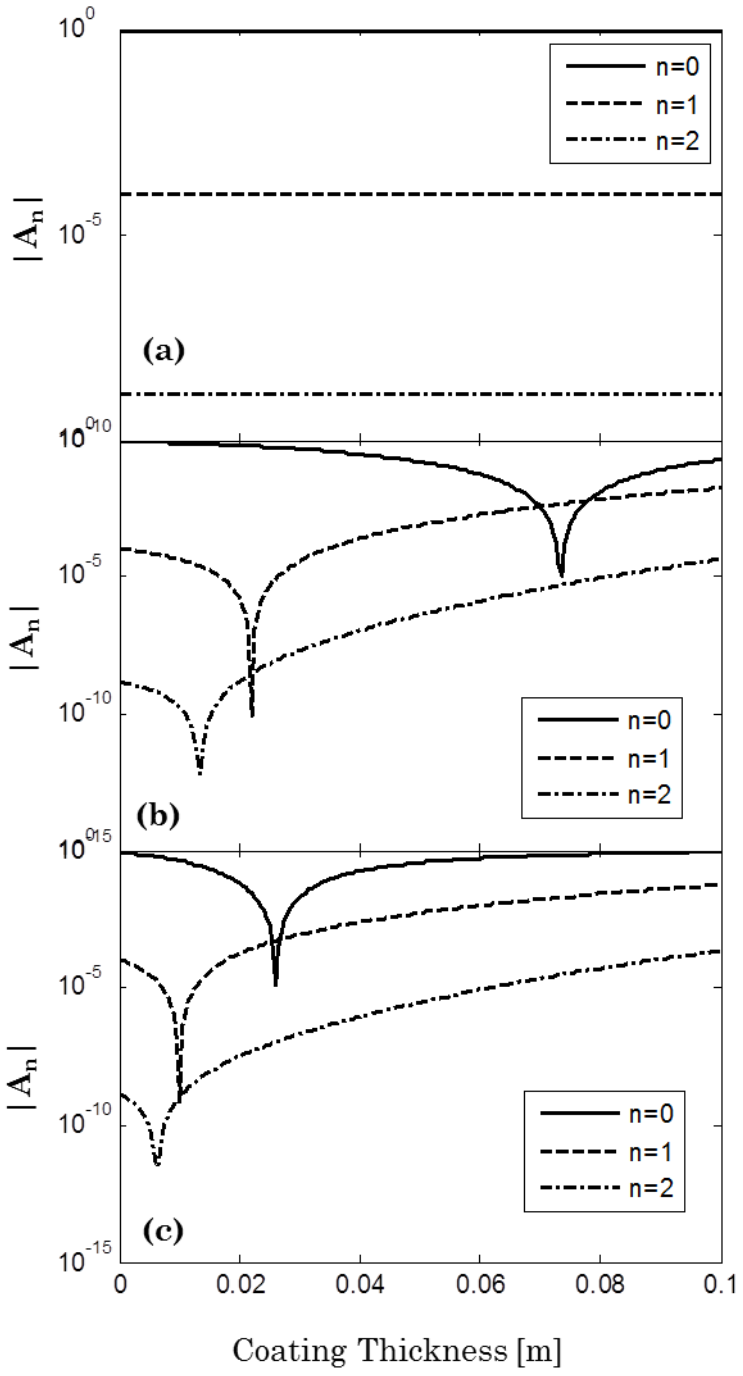

Figure II-3: Plots of scattering coefficients as a function of cover thickness for various lossless cover permittivity values of (a) 1 (uncoated rod) (b) -2 and (c) -8.

The plots show that the higher order modes (multipolar modes) too could be minimized due to the cover but with a different cover thickness. However, the value of the A_1 and the A_2 terms are generally small enough to be neglected. But comparing the solid line (dipolar term) across Fig. II-3 (a-c), it can be confirmed that the scattering due to dipolar term could be reduced by covering the cylinder with a plasmonic material. An interesting point to note is that the A_1 and the A_2 terms are modified due to the presence of the cover. Although the cover was primarily designed to reduce the dipolar scattering, it tends to reduce the higher order terms as well although not by a lot. By suitably engineering a cover or layers of covers, it might be possible to null all the terms in the scattering expansion. But with a single cover, the higher order terms could limit the achievable scattering reduction for larger cylinder sizes and thicker covers. The cover permittivity values of -2 and -8 require a cover thickness equal to or greater than the cylinder radius. This tends to increase the total particle size thereby increasing the values of the higher order terms.

C. Design and parametric analysis

The final goal was to implement the scattering cancelation structure at optical frequencies and characterize it using the heterodyne-NSOM setup. Since the heterodyne setup operates at a wavelength of 1550 nm, the design wavelength of minimal scattering was chosen to be 1550 nm. The radius of the cylinder was chosen to be 100 nm (~ λ/16 at 1550 nm) which would a reasonable size to fabricate

using electron-beam lithography. The diameter of the cylinder would then be 200 nm or ~λ/8 and hence would be sub-wavelength in size.

The key variables which affect the design of the system are the radius and permittivity of the dielectric cylinder, the thickness and permittivity of the cover and the permittivity of the background medium. An understanding of the relationship between the parameters might help simplify the design process. Based on the heuristic analysis presented earlier, we can compare the volume integrals of polarization between the cylinder and cover and seek the conditions that would make them equal in magnitude and opposite in sign. In the two-dimensional geometry, volume which reduces to area is proportional to the square of the radius. Since the polarization is proportional to the permittivity, we can expect that the cylinder radius/cover thickness and material permittivity will be inversely related to each other. A thicker cover would require lower cover permittivity and vice versa.

Fig. II-4 (a) plots the scattering cross-section (C_{scatt}) as a function of the coating thickness for different values of cover permittivity with no loss and Fig. II-4 (b) plots the Scattering cross-section (C_{scatt}) as a function of cover permittivity for different values of the cover thickness. In both cases, the cylinder radius and cylinder permittivity are kept constant at 100 nm and 9 respectively. The background permittivity is also kept constant at 2.25. All three constant values are readily achievable at optical frequencies. The wavelength at which the calculations were carried out was 1550 nm.

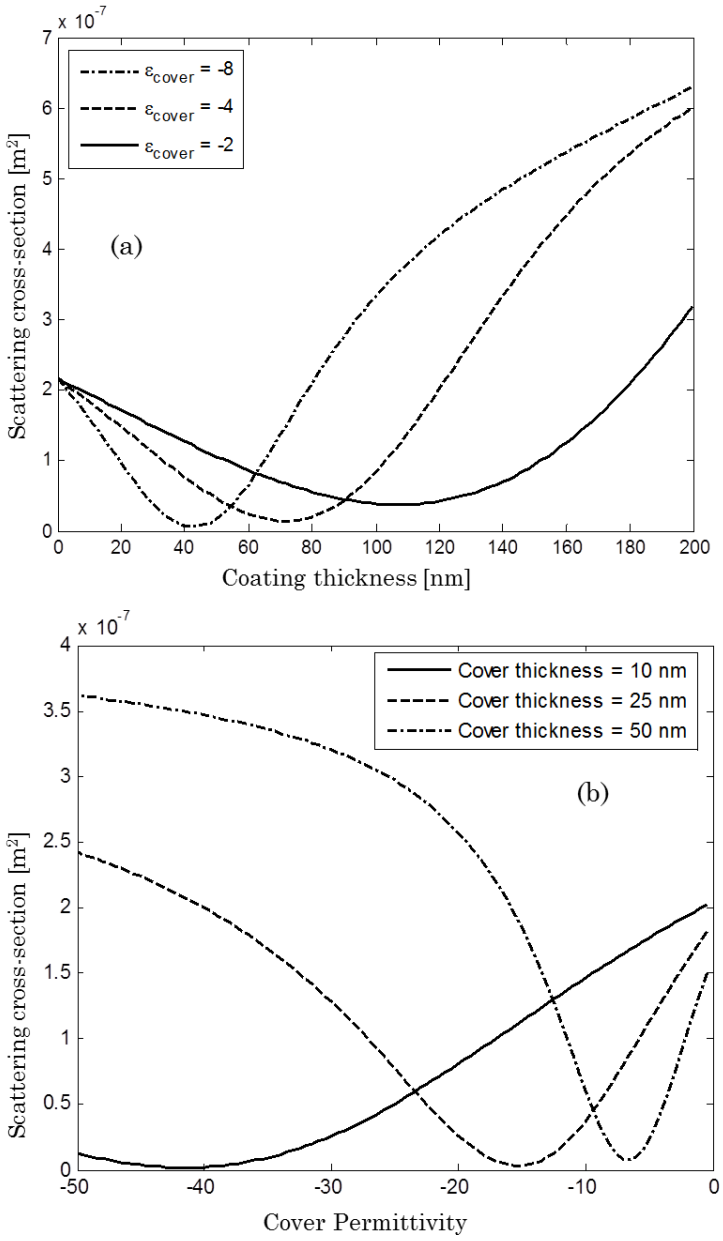

Figure II-4: (a) Plot of scattering cross-section as a function of coating thickness for cover permittivity values of -2, -4 and -8. (b) Plot of scattering cross-section as a function of cover permittivity for various coating thickness. In both cases, the cylinder radius and cylinder permittivity were 100 nm and 9 respectively. The permittivity of the background medium was 2.25. The wavelength at which the calculations were carried out was 1550 nm.

From Fig. II-4, it can be observed that as predicted by the heuristic analysis, the thickness of the cover that results in minimum scattering is inversely related to the cover permittivity. Thinner covers need a smaller value of cover permittivity while thicker cover films need a larger value of permittivity. It can also be observed that the minimum value of scattering cross-section becomes smaller as the cover thickness is reduced since the total size is smaller for thinner cover, thereby making the dipole term dominant. With a thicker cover, the higher order modes would contribute more to the total scattering and these higher order modes would not be nulled by the dipole cancelling mechanism. The scattering cancellation technique is inherently non-resonant which leads to design flexibility in the choice of cover thickness and permittivity values as seen in Fig. II-4. However, the use of resonant plasmonic metamaterial structures as covers would destroy the non-resonant behavior and make the system narrow-band. Hence, it would be advisable to implement the plasmonic metamaterial structure as a non-resonant system.

In practice, a cover made up of a plasmonic material would have some loss. The loss in the cylinder dielectric can be ignored as it would typically be much smaller than the loss in the plasmonic material. Fig. II-5 (a) repeats the results of Fig. II-4 (a) the $\mathrm{Re}(\varepsilon_{cover}) = -2$ case with loss ($\mathrm{Im}\{\varepsilon\}$) values of 0.5 and 1 and Fig. II-5 (b) repeats the results of Fig. II-4 (a) for $\mathrm{Re}(\varepsilon_{cover}) = -8$ with loss ($\mathrm{Im}\{\varepsilon\}$) values of 2 and 4.

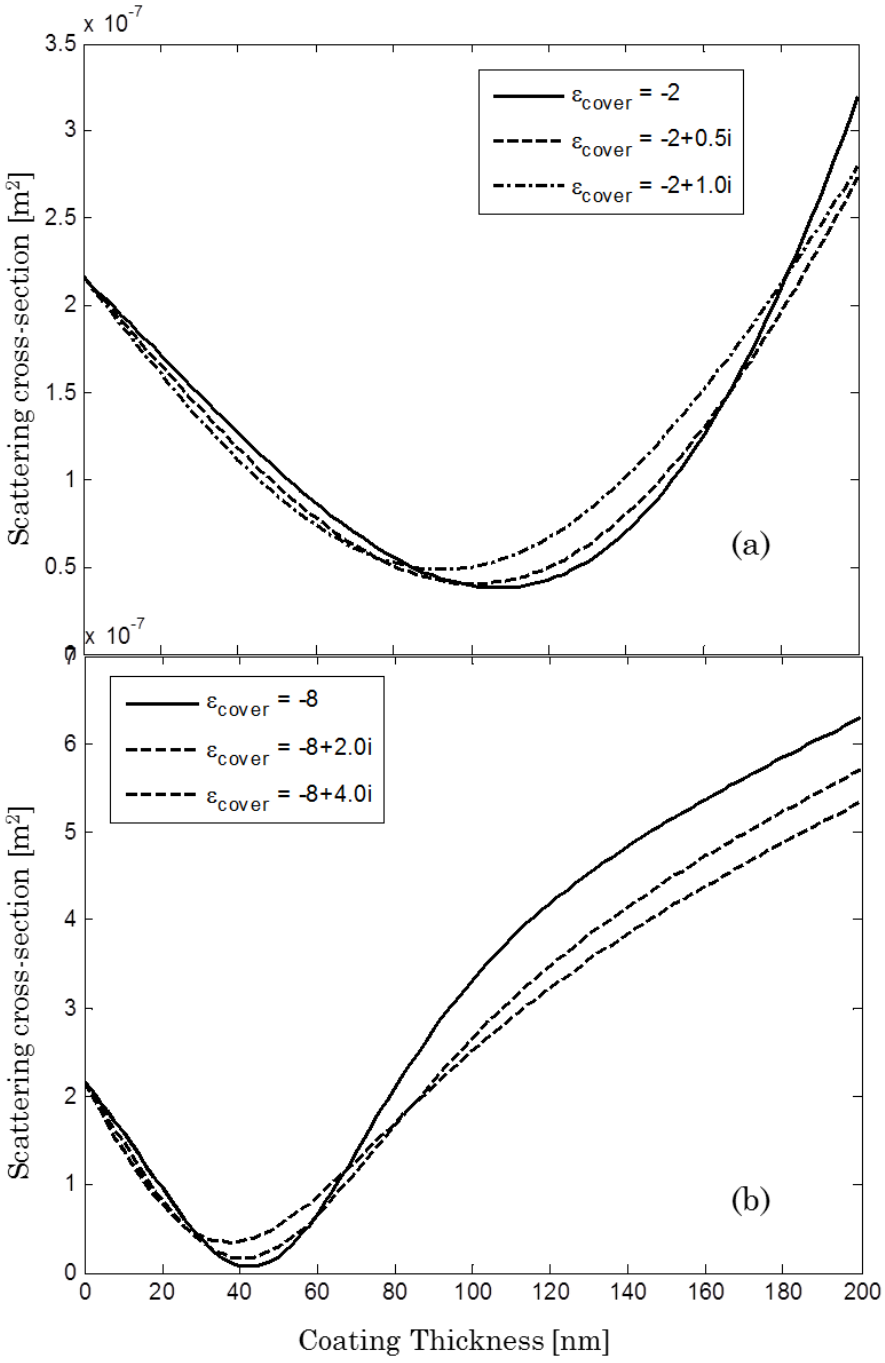

Figure II-5: (a) Plot of scattering cross-section as a function of coating thickness for cover permittivity values of -2 with loss (Im{ε}) values of 0.5 and 1 (b) Plot of scattering cross-section as a function of coating thickness for cover permittivity values of -8 with loss (Im{ε}) values of 2 and 4.

Despite the large ohmic loss added, it can be seen that the scattering cross-section is not dramatically altered. This is an important consideration as practical plasmonic materials composed of very thin metal layers can have increased losses compared to bulk materials, due to surface scattering. The loss could be amplified in resonant systems, but the non-resonant nature of the scattering cancellation method makes it less sensitive to the loss in plasmonic materials.

So far, the analysis has been performed at a single wavelength for a non-dispersive cover permittivity. However, practical implementations would need to use natural or engineered plasmonic materials whose dielectric function could typically be described by the Drude-Lorentz model. At optical frequencies, commonly used plasmonic materials include noble metals such as gold and silver. These materials have a negative real part of permittivity at wavelengths above their plasma wavelength. Hence, these materials may possibly be directly used as plasmonic covers for scattering cancelation devices operating at visible wavelengths.

However, at near infrared frequencies gold has a very large negative real part of permittivity. This would imply that the cover thickness would need to be very small. We investigate this further by tabulating the required cover thickness for a variety of metals using their experimentally measured dielectric constants at 1500 nm [4, 6]. The dielectric cylinder radius was chosen to be 100 nm and the cylinder permittivity was chosen as 9. The permittivity of the background medium was

chosen to be 2.25. Also tabulated is a figure of merit named '*Scattering Reduction* (SR) indicating the scattering cancelation performance and is defined as

$$SR = 10\log_{10}\frac{C_{scattering}(Bare\ Cylinder)}{C_{scattering}(Cloaked\ Cylinder)} \tag{2.12}$$

Metal	Re(ε) at λ = 1550 nm	Im(ε) at λ = 1550 nm	Thickness (nm)	*SR (dB)*
Gold	-108	10	4	17
Silver	-122	3	3.6	20
Copper	-106	14	4	15
Titanium	-7	33	10	2
Chromium	-3	30	11	2.5
Iron	-17	32	10	3.5
Nickel	-48	46	6	5

Table II-1: Tabulation of required cover thickness for thin films of metals used as covers.

Based on the results in Table II-1, it would be optimum to use silver, gold or copper due to their large *Scattering Reduction* values. However, the cover would need to be extremely thin due to the large negative values of the real part of permittivity. Reliable deposition of such thin films is generally difficult to achieve. Therefore, it is necessary to design a suitable, low loss plasmonic metamaterial

structure to achieve reduced visibility due to scattering reduction at near-infrared frequencies.

The reason that gold, silver and copper have such large negative values of real part of permittivity at around 1550 nm is due to the fact that their plasma frequency is in the ultraviolet regime. From the previous studies of cover permittivity and cover thickness, we observe that $-5 \leq \mathrm{Re}(\varepsilon_{cover}) \leq -15$ could be considered an optimum range for the cover permittivity. This would mean that the plasmonic metamaterial structure would need to have a plasma frequency closer to 1550 nm. As the plasma frequency is proportional to the square root of the free electron density, reducing the free electron density would lower the plasma frequency. This could be thought of diluting the free electron density and hence we could think of this metamaterial as a dilute metal. Previously, different types of artificial structures with a Drude-Lorentz type permittivity response have been proposed. Brown [65], Rotman [66] and Golden [67] demonstrated that the "Rodded Medium", composed of thin metallic wires embedded in a dielectric background, behaved as artificial plasma with behavior similar to that of metals at visible frequencies. Recently, Pendry proposed a similar structure now well known as the wire medium [68]. The wire medium is inherently non-resonant and therefore broadband.

We chose to implement the dilute metal as a gold grating etched around the circumference of the cylinder (nanorod). This method was chosen to leverage the high resolution milling capabilities of the Focused Ion Beam (FIB) machine. A

simple theoretical model for the dilute metal composed of a gold grating structure is outlined below and further details can be found in [69]. We start by considering the optical properties of the stratified/layered composite material. Fig. II-6 shows the geometry of the problem.

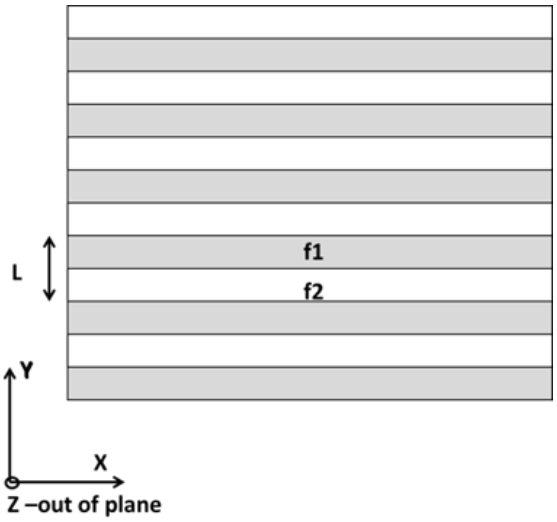

Figure II-6: Geometry of the simple layer/stratified medium used to model the dilute metal.

Let us consider a structure composed of multiple thin layers of two different materials stacked on top of each other. Let the period of stacking be L and f_1 and f_2 be the fill fractions of the two layers. In the above example, we consider only two material layers with the restrictions that the thickness of each layer be much less than the wavelength of light inside the material and the sum of fill fractions is unity ($f_1+f_2=1$). This technique can be easily extended to multiple layers provided the restrictions on thickness and fill fractions are satisfied [69]. Let us assume for now that both layers are made of non-magnetic materials. Let the darker bar (with

fill fraction f_1) represent gold and we use a Drude-Lorentz type permittivity function to model its dielectric response, $\varepsilon_{gold}(\omega)$,

$$\varepsilon_{gold}(\omega) = 1 - \frac{\omega_p^2}{(\omega^2 + i\gamma\omega)} \tag{2.13}$$

where, ω_p represents the plasma frequency and γ represents the damping rate. Let the lighter bar (with fill fraction f_2) represent a dielectric material (also called the host material) with permittivity function ε_d. From the geometry of the problem, we can visualize two principal polarizations and each polarization is associated with a corresponding effective permittivity representing the dielectric response of the entire stratified structure. When the incident electric field is in the *xz* plane, we observe that the field is always parallel to the interface between the two films. We choose to call this the parallel polarization and the effective permittivity is labeled as ε_p. When the incident electric field is along the *y* direction, we observe that the field is always perpendicular to the interface between the two films. We choose to call this the perpendicular polarization and the effective permittivity is labeled ε_s.

For parallel polarization, the electric field in all the layers is the same according to the boundary conditions imposed by the Maxwell's equations. But the electric flux density $\boldsymbol{D}$ is not constant throughout. Taking an averaged value for the polarization, we get

$$\varepsilon_p(\omega) = f_1\varepsilon_{gold} + f_2\varepsilon_d \tag{2.14}$$

For perpendicular polarization, the electric flux density would be continuous across the interface. Hence by the constitutive relations the electric field would be

discontinuous across the interface. Taking an averaged value for the polarization, we obtain a harmonic mean

$$\varepsilon_s(\omega) = \frac{\varepsilon_{gold}\varepsilon_d}{\mathrm{f}_2\varepsilon_{gold} + f_1\varepsilon_d} \tag{2.15}$$

Substituting Eqn. (2.13) into (2.14) and noting that f_1+f_2 = 1, we obtain the following results

$$\varepsilon_p(\omega) = \varepsilon_d + f_1(1 - \varepsilon_d) - \frac{f_1\omega_p^2}{(\omega^2 + i\gamma\omega)} \tag{2.16}$$

Let us write,

$$\varepsilon_d' = \varepsilon_d + f_1(1 - \varepsilon_d) \tag{2.17}$$

And let us call ω_{pd} as the dilute plasma frequency given by

$$\omega_{pd} = \sqrt{f_1}\omega_p \tag{2.18}$$

Then Eqn. (2.18) can be rewritten as

$$\varepsilon_p(\omega) = \varepsilon_d' - \frac{\omega_{pd}^2}{(\omega^2 + i\gamma\omega)} \tag{2.19}$$

Eqn. (2.19) has the same form as Eqn. (2.13); the Drude-Lorentz model. When f_1 << 1, then we can see that the dilute plasma frequency ω_{pd} is less than ω_p. Thus, by controlling the fill fraction of gold in the composite we can tune the plasma frequency of the composite material.

Repeating the procedure for the effective permittivity for perpendicular polarization we find

$$\varepsilon_s(\omega) = \frac{\varepsilon_d\left(1 - \frac{\omega_p^2}{(\omega^2 + i\gamma\omega)}\right)}{\varepsilon_d'' - \frac{f_2\omega_p^2}{(\omega^2 + i\gamma\omega)}} \tag{2.20}$$

where,

$$\varepsilon_d'' = \varepsilon_d + f_2(1 - \varepsilon_d) \tag{2.21}$$

The results of Eqn. (2.20) show that $\varepsilon_s(\omega)$ has both a pole and a zero. The zero occurs at a plasma frequency similar to the normal metal. However, the permittivity function exhibits a resonance when the denominator is zero. This would be possible at the resonance frequency ω_0 given by

$$\omega_0 = \sqrt{\frac{f_2}{\varepsilon_d''}}\,\omega_p \tag{2.22}$$

Results of a numerical example are presented in Fig. II-7 with the x axis is reversed and in a logarithmic scale. Let us assume $\varepsilon_d = 2.25$, $f_1 = 0.2$ and therefore $f_2 = 0.8$; the plasma frequency ω_p is assumed to be 1 rad/s and damping rate is assumed to be zero (lossless system). The solid line plots the permittivity function of the pure metal notated as ε_{metal}. The dashed line plots the permittivity function of the dilute metal notated as ε_{dilute}. From the above equations, the plasma frequency of the dilute metal is calculated to be 0.45 rad/s and is more than halved from the original value. The dotted line plots the response of the resonant effective permittivity for the perpendicular polarization and is denoted as ε_{res}. From the above equations, the resonant frequency is calculated be 0.54 rad/s and lower than the real metal plasma frequency.

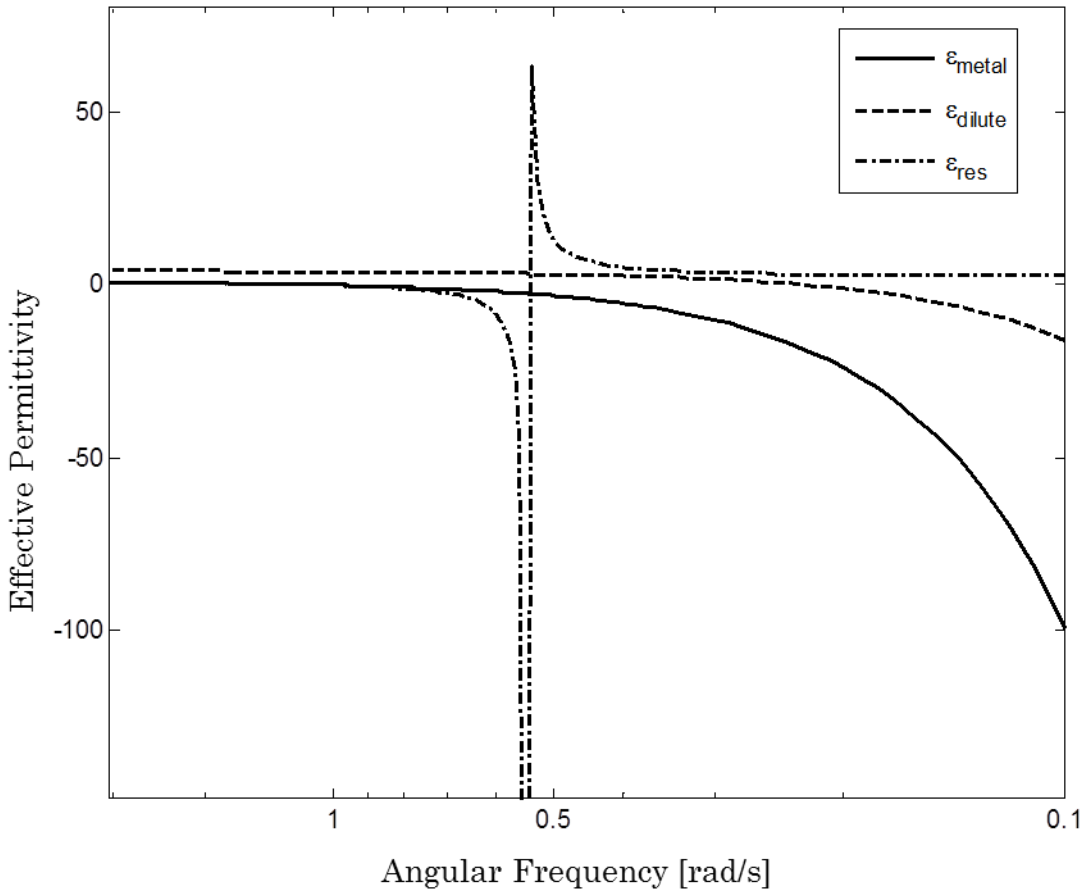

Figure II-7: Results of a design example for layered effective media plotting the effective permittivity for the parallel and perpendicular polarizations.

A schematic of the grating structure used as the plasmonic metamaterial is shown in Fig. II-8. The periodicity of the grating structure was P and the fill fraction of gold is determined by the grating width W. The grating height H entered the scattering cancelation device model as the cover thickness. The incident wave was along the y direction and the electric field along the z direction. The dark color represents the gold grating and white color a dielectric material like silicon dioxide

and was different from the background material. The choice of gold metal and silicon dioxide surrounding the gold grating was dictated by the fabrication procedures as detailed later.

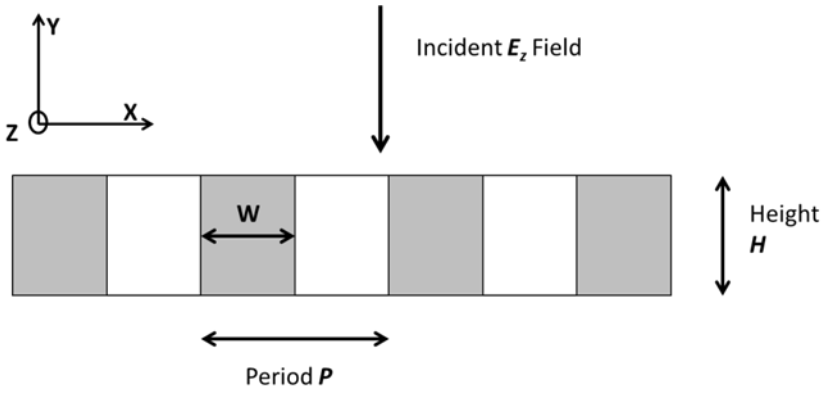

Figure II-8: Schematic of gold grating structure used for analytical calculation of effective permittivity of gold grating structure.

The effective permittivity for the above structure was calculated using Eqn. (2.16) after substituting $f_1 = W/P$. The complex dielectric constants of gold used were obtained from the measured data tabulated in [6] and the refractive index of silicon dioxide was assumed to be 1.45. This effective cover permittivity was used in the scattering cancelation device model developed earlier. To obtain the periodicity of the grating, we assume the center rod of diameter to be180 nm, surrounded by eight gold gratings. The periodicity was calculated to be 70 nm from the center rod diameter of 180 nm. The thickness of the cover was chosen to be 15 nm and the grating width was varied until the scattering cross-section minimum occurred at 1550 nm. The permittivity of the cylinder was assumed to be 9 and the permittivity of the background was assumed to be 2.25.

Plotted in Fig. II-9 are the results obtained from the analytical method (using Eqns. (2.7), (2.11), (2.19) and (2.20)) confirming the scattering reduction due to the plasmonic metamaterial cover for TM polarization. The solid line plots the scattering cross-section of the bare cylinder, and the dashed line plots the scattering cross-section of the scattering cancelation device (SRD).

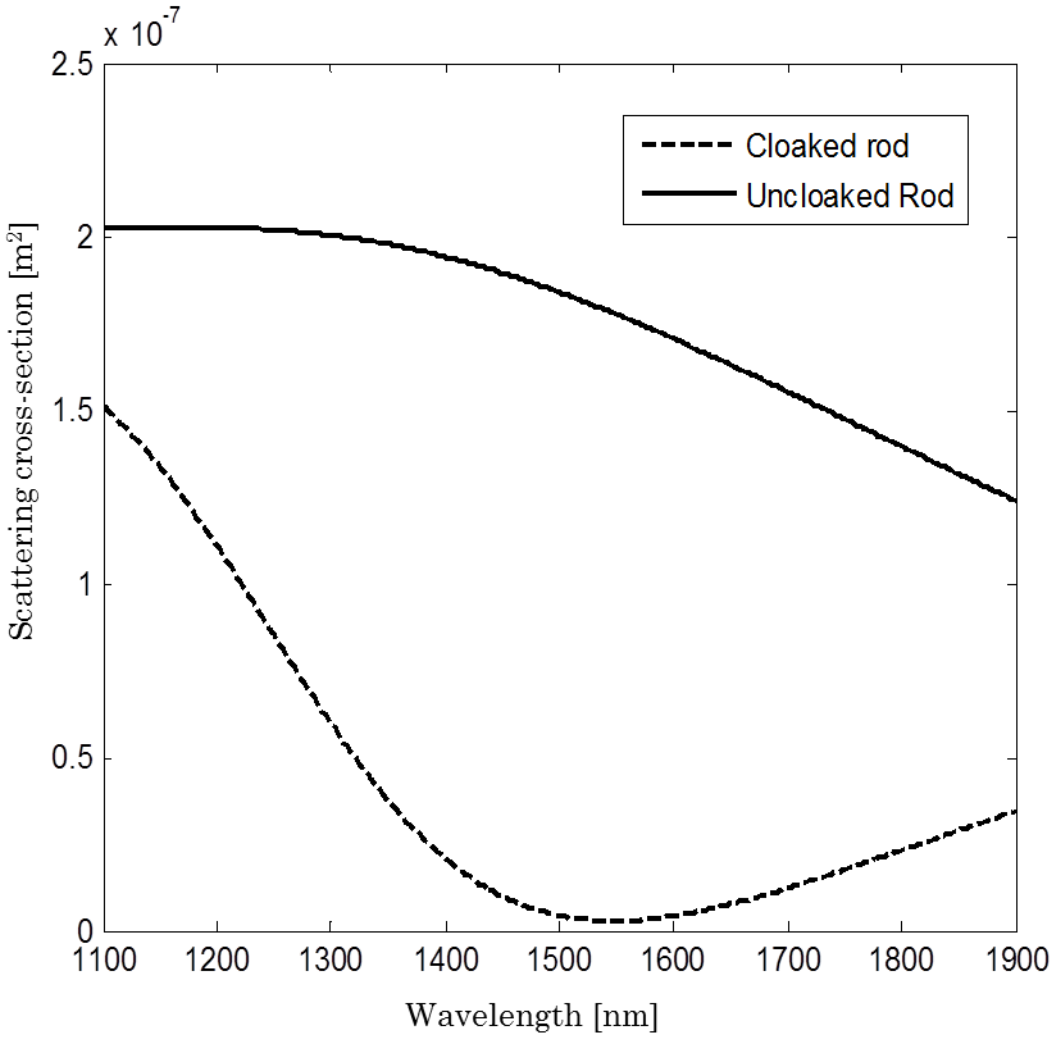

Figure II-9: Scattering cross-section as a function of wavelength for bare and scattering cancelation device. The bare rod diameter was chosen to be 180 nm. The plasmonic material consisted of eight gold gratings each of width 15 nm and periodicity of 70 nm. The gold thickness was 13 nm.

The bare rod diameter was chosen to be 180 nm so that it would still be subwavelength (~λ/8.6 at 1550 nm). To obtain the minimum scattering cross-section at 1550 nm, the gold grating width was found to be 15 nm. The *SR* value at 1550 nm was 19 dB. The value of the effective permittivity at 1550 nm was -22.3+2.3*i* and much larger than the optimum value between -5 and -15. To obtain a smaller value of effective permittivity would require either an increase of periodicity or a reduction in the gold grating width (also called fin width). From initial experiments with the Focused Ion Beam (FIB) machine, it was found that 15 nm was the minimum attainable fin width and the above design already used that value. Therefore, the only recourse would be to increase the diameter of the cylinder and thereby increase the periodicity to maintain at least eight grating periods around the rod.

Plotted in Fig. II-10 is the real part of effective permittivity as a function of periodicity for various fin widths. In order to achieve $\mathrm{Re}(\varepsilon_{\mathrm{eff}}) \sim -10$ with the least periodicity, the fin width would need to be 10 nm. Fin widths of 10 nm would be very difficult to fabricate. If we choose a fin width of 20 nm, which could be easier to fabricate, the periodicity would need to increase to ~150 nm. This translates to a rod diameter of 380 nm or λ/4 at λ=1550 nm. At such large rod sizes, the dipolar mode is no longer the dominant scattering mode and therefore the *SR* would be very small. We observe that the diameter of the rod (and thereby the periodicity) and the fin width are thus constrained within a narrow range of allowable values. Hence, the

cover thickness is an important and easily controllable parameter to tune the minimum of the scattering cross-section.

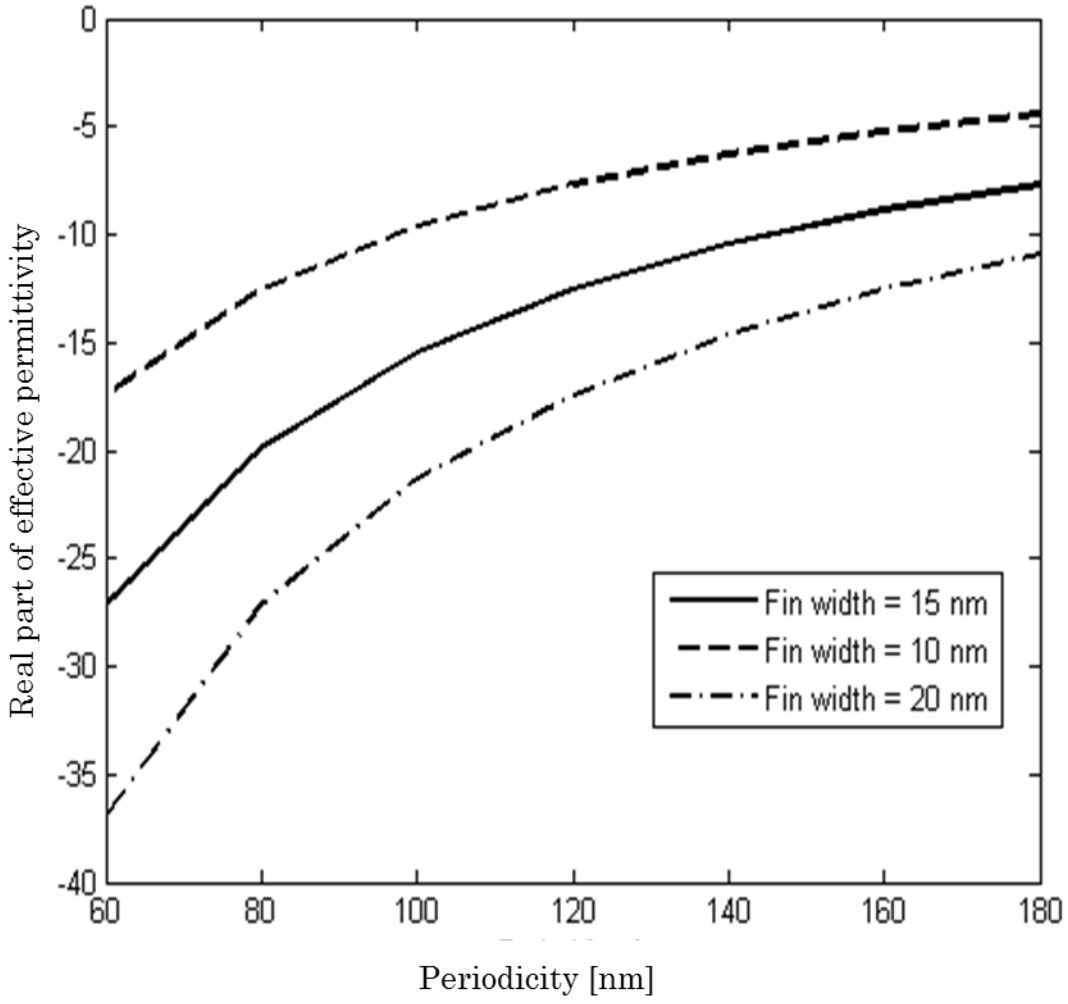

Figure II-10: Plot of real part of effective permittivity as a function of period for various fin widths.

Plotted in Fig. II-11 is the scattering cross-section for various gold coating thicknesses with constant fin width of 15 nm and periodicity of 70nm. The variation of gold thickness by 10 nm tunes the minimum of scattering cross-section by around

400 nm. The value of scattering cross-section was 4.5×10^{-8} m^2 at 1400 nm and 1.6×10^{-8} m^2 at 1800 nm.

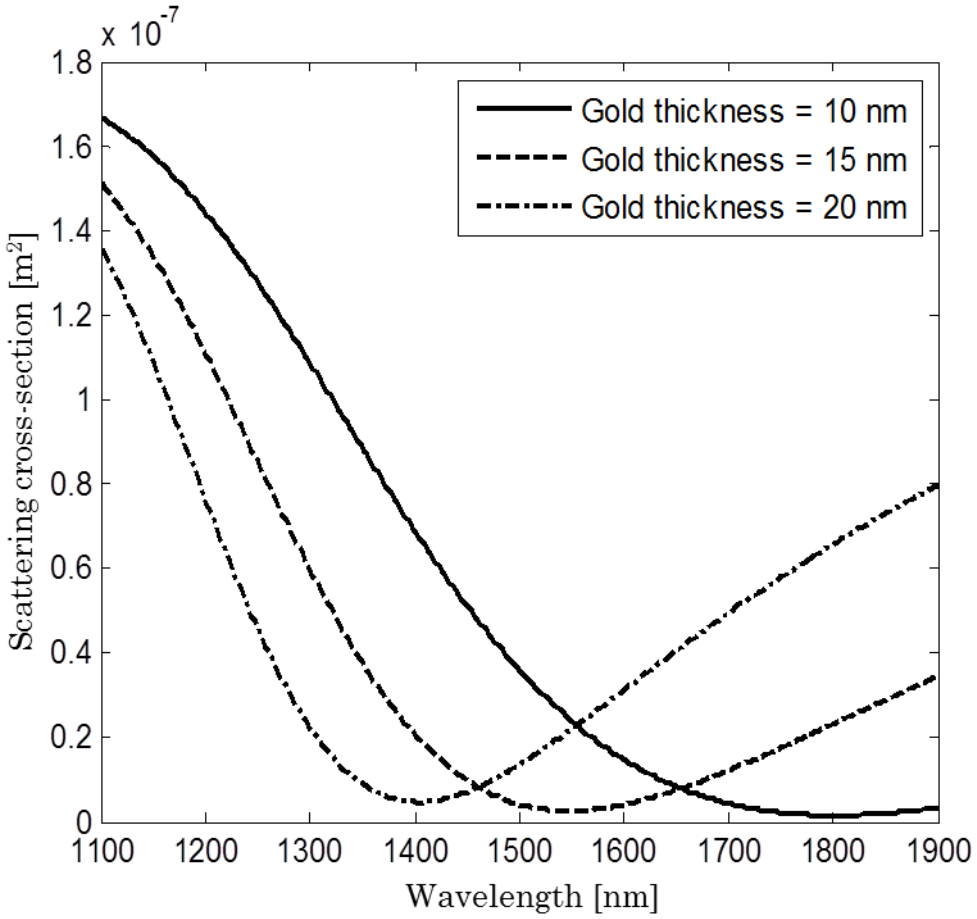

Figure II-11: Plot of wavelength dependent scattering cross-section for various gold thicknesses of 10 nm, 15 nm and 20 nm a constant fin width of 15 nm and periodicity 70 nm.

The above analytical technique for calculation of frequency dependent scattering parameters based on effective permittivity is only an approximate method as it does not take into account the curvature of the cylindrical rod. A study taking into account the curvature was done in [57] and a technique for obtaining the

effective parameters has also been proposed. However, the proposed technique would complicate the fabrication procedures and hence we obtained the solution to the fabricated SC device structure by the Finite Element Method (FEM) using the commercial solver COMSOL V3.5a.

D. Implementation of scattering cancelation device at optical frequencies

The design strategies of such complicated nanostructures are guided by the capabilities and limitations of the fabrication and characterization techniques. Therefore, the design of the scattering cancelation device (SCD) followed the fabrication closely so as to arrive at the right design parameters which could then be fabricated. As discussed earlier, we decided to characterize the SCD using the Heterodyne-NSOM setup. The H-NSOM setup is optimized to operate in collection mode using metal coated tapered aperture probes at infrared wavelengths. Therefore, we chose to design the SCD for operation in the near-infrared spectrum for transverse magnetic (TM, electric field perpendicular to the device) polarization in a quasi-two-dimensional waveguide geometry. The structure was fabricated on a silicon-on-insulator (SOI) wafer consisting of a 340 nm thick single crystalline silicon layer on top of a 2 μm thick silicon dioxide (SiO2) over a bulk silicon substrate.

As described previously, the SCD structure consisted of a silicon nanorod, 340nm high with a design diameter of 180 nm surrounded by a plasmonic nanostructure made up of eight gold fins surrounded by silicon dioxide. A 10 μm

wide silicon waveguide was used to illuminate the SCD structure by a plane wave. The structure was placed 5 µm from the edge of the waveguide. The entire structure was coated with a 370 nm thick layer of SU8 photoresist which was hard baked. The SU8 photoresist served as a background medium in which light could propagate and also served as a surface over which NSOM scans could be reliably performed. In addition, the SU8 surface served to isolate the gold nanostructure from the metal coated NSOM probe thereby preventing any unwanted interactions which could potentially lead to artifacts in the NSOM scan. After curing and hard baking the SU8, the sample was then cleaved so that light could be coupled into the device by butt-coupling (also known as end-coupling) an optical fiber. The fabrication of the SCD nanostructure was performed using electron beam lithography to define the rod and focused ion beam milling to define the gold grating structure. A schematic of the entire structure is shown in Fig. II-12.

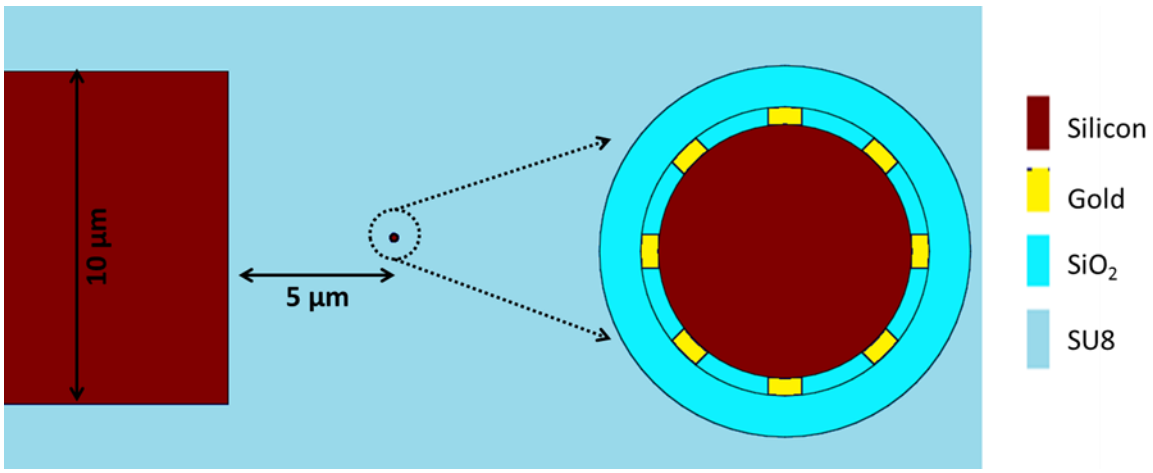

Figure II-12: Schematic of the fabricated scattering cancelation device structure and the 10 µm wide input waveguide. The distance between the edge of waveguide and center of rod is 5 µm.

The fabrication process began by photo-lithographically defining the 10 μm wide input waveguide and alignment marks for future patterning of the rod by electron beam lithography. Then, the pattern on the resist was transferred to a 100 nm thick chromium mask using a lift-off procedure. A thin layer of PMMA positive electron beam resist was spin coated. Using the previously defined alignment marks, the silicon nanorod was defined using electron beam lithography. After developing the PMMA resist, a protective layer of 20 nm thick chromium was deposited and lift-off was performed to transfer the rod pattern to the 20 nm thick chromium layer. Reactive ion etch of silicon was carried out with the combined 120 nm chromium protection layer. This step etched away silicon in all areas except those below the chromium layer and thereby shaped the input waveguide and the rod simultaneously. The chromium layer was then dissolved using a chromium etchant to reveal the bare rod. At this point, the structure was imaged using scanning electron microscopy to verify the size of the fabricated rod, and one such image is shown in Fig. II-13. The sidewall of the fabricated rod was not exactly vertical and had a small slope. The diameter at the top of the rod was measured to be ~160 nm and the diameter at the bottom was measured to be ~200 nm. The sidewall angle was calculated to be ~86.5° from the horizontal. Due to the sidewall angle being so close to 90°, the non-vertical sidewall was ignored as it was assumed that it would not cause any appreciable deviations in the scattering response.

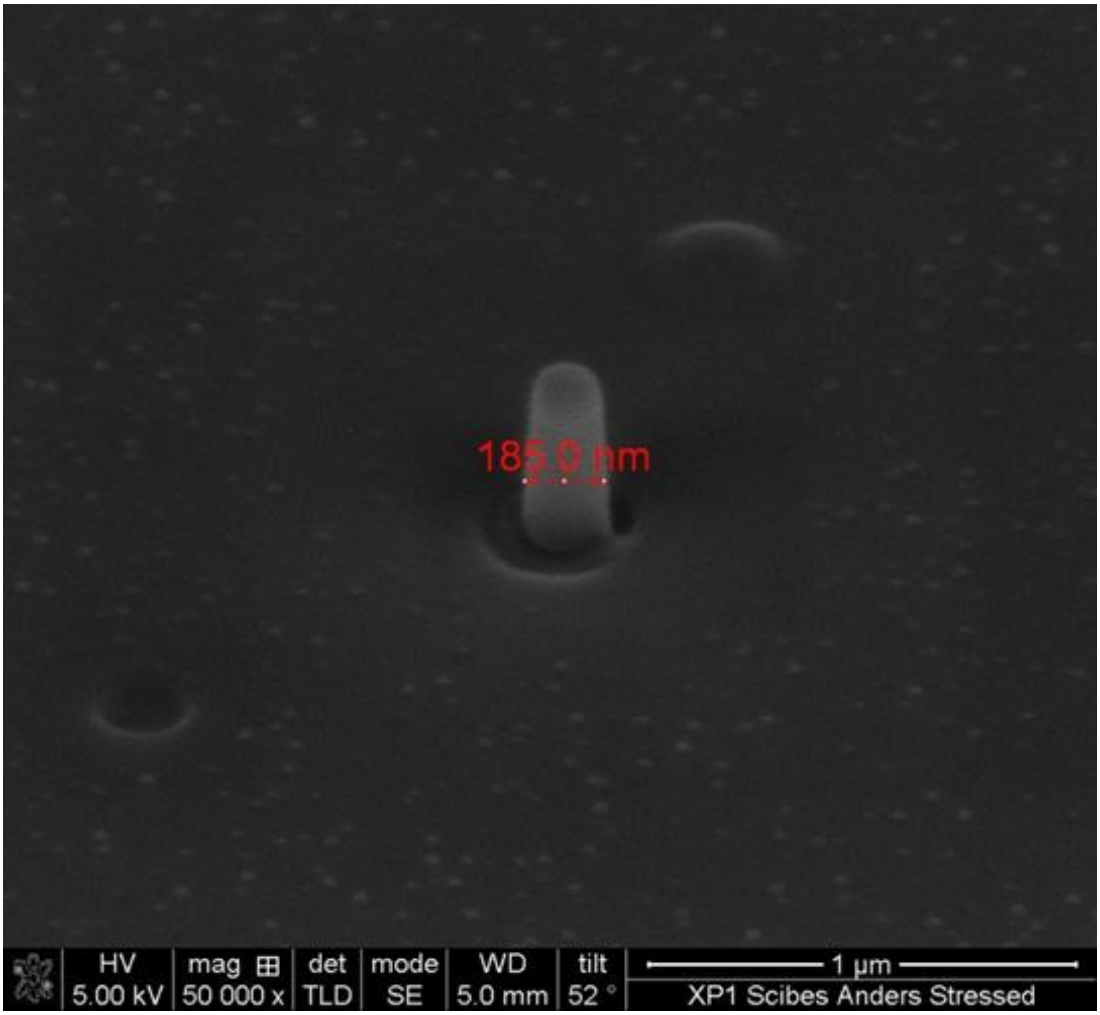

Figure II-13: Scanning electron micrograph showing a fabricated bare rod. The average rod diameter measured near the vertical center was ~185 nm.

Future work could consider the perturbation in the scattering cross-sections due to the non-vertical sidewall. As shown in the Fig. II-13, an average diameter of 185 nm was measured near the vertical center of the rod, and this value was used in further calculations.

Based on numerical simulations performed using COMSOL (to be presented later), the thickness of the gold layer was designed to be 13 nm assuming a 20 nm

fin width. From the initial experiments using FIB, we found that gold had a tendency to melt under even a light dose of gallium ions. In order to protect the gold film, it was coated with a layer of chromium as a protection layer since chromium was found to withstand milling by gallium ions. Once the combined gold and chromium layer was milled to the required dimension, the chromium was chemically etched leaving behind only the required gold nanostructure. Gold was found to be resistant to the chromium etchant while silver was etched away. It is for this reason that the combination of gold and chromium was chosen despite silver being a material with lower optical loss as tabulated in Table II-1.

Based on the above information and some experimentation, it was decided to deposit a 13 nm thick layer of gold followed by a 10 nm thick chromium layer. In a standard line-of-sight deposition system, the metal would not be deposited on the sidewalls of the rod. Therefore, in order to also deposit the metals on the sidewall, the evaporation was performed in an off-axis rotating evaporator. Both the metals were evaporated with a slow deposition rate in the same run without breaking vacuum. Slow deposition rate was required for such low thickness values to obtain good quality uniform films. Formation of non-continuous particulate films would significantly increase the optical losses. The rods were imaged using the scanning electron microscope and the rod size carefully measured to verify the deposited thickness. This process was repeated a couple of times until the desired results were obtained. Fig. II-14 shows an image of the bare rod shown in Fig. II-13 after coating by gold and chromium layers.

Figure II-14: Scanning electron micrograph showing the metal coated bare rod with a net diameter of ~230 nm measured near the vertical center of the rod giving a gold thickness of 13 nm.

The diameter at the top of the rod was ~ 205 nm and the diameter at the bottom was measured to be ~ 245 nm indicating that the combined thickness of the metals was about 26 nm and matched the thickness required by design. An average diameter of 231 nm was measured near the vertical center of the rod.

Next, the gold fins were defined by using the focused ion beam to mill the gold. The gallium ion beam came in from the top of the rod to obtain more control while

milling. This was the most delicate and labor intensive task of the entire process. A series of dose tests was performed to ensure minimal fin width variation. After the metal layers had been milled to the required size, the chromium layer was removed using the chemical etchant and the structure was imaged using the scanning electron microscope. An image of the coated rod (shown in Fig. II-14) after completion of the milling and etching process is shown in Fig. II-15.

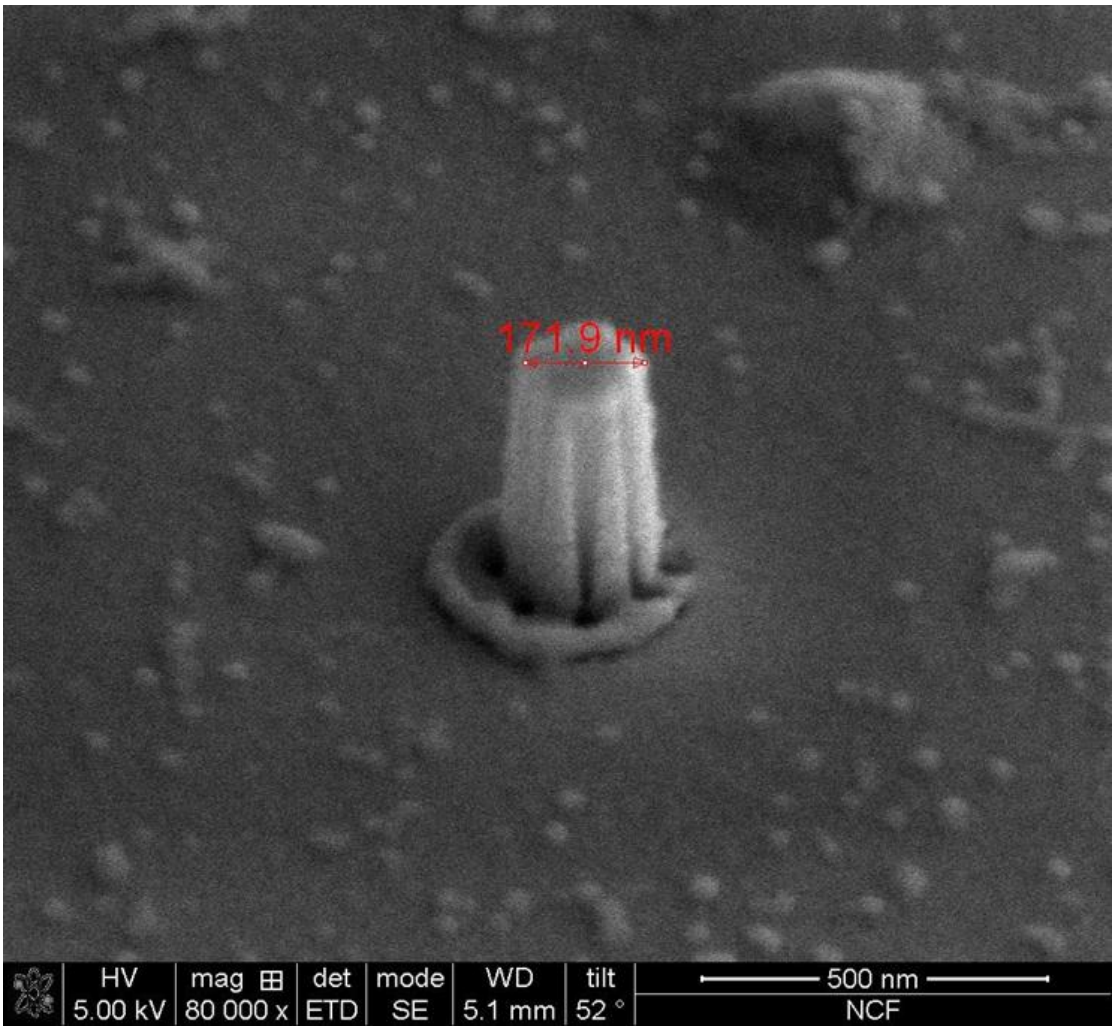

Figure II-15: Scanning electron micrograph showing the rod after FIB milling. The diameter at the top of the rod was measured to be ~172 nm giving a gold thickness of 12 nm.

Fig. II-16 (a) shows a low magnification scanning electron micrograph of a top view of the fabricated structure and Fig. II-16 (b) displays a lower magnification scanning electron micrograph showing both the fabricated rod as well the 10 µm wide input waveguide.

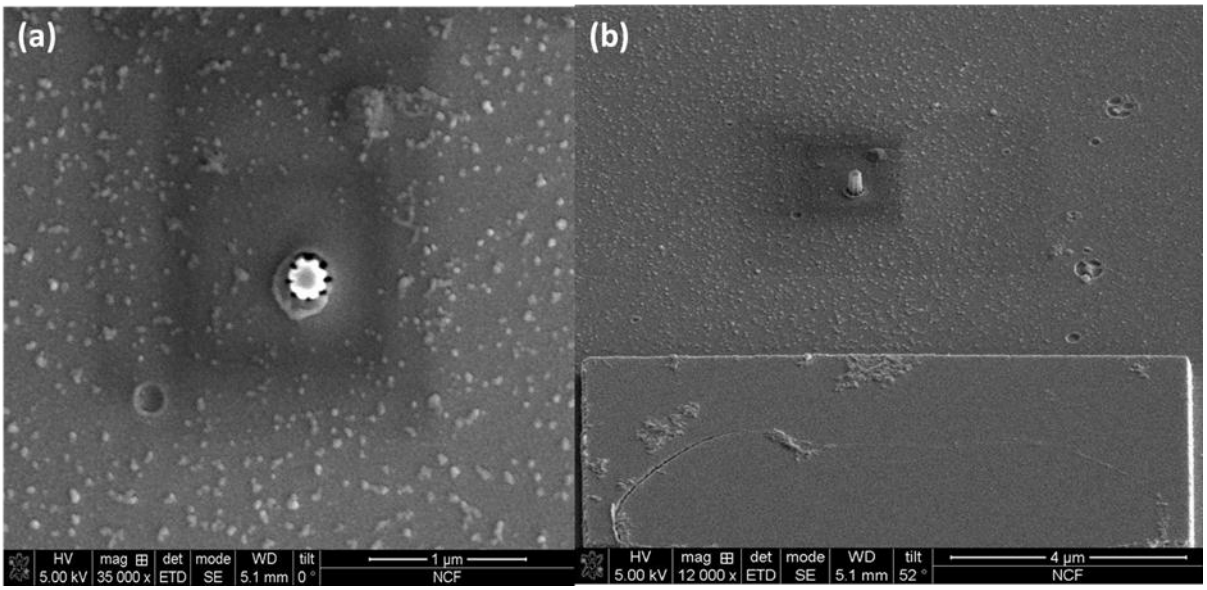

Figure II-16: (a) low magnification scanning electron micrograph image of top view of the fabricated structure and (b) lower magnification scanning electron micrograph image showing both the fabricated rod as well the 10 µm wide input waveguide.

Some important data were extracted from the images in Fig. II-15 and II-16 (a). From Fig. II-15 it can be seen that the fin width is not uniform throughout the height of the rod. The fin width is smaller at the top and larger at the bottom of the rod. The measured diameter at the top of the rod is ~ 172 nm which indicates that the thickness of gold grating structure at the top is about 12 nm compared to the

design value of 13 nm. The varying fin width cannot be directly estimated from Fig. II-15 due to the angle at which the image was taken. However, the gap between the fins could be estimated reasonably accurately as the gap was almost in a frontal position to the detector.

The gap at the bottom of the device was measured to be ~20 nm and at the top was measured to be ~50 nm. As the periodicity was ~70nm, the fin widths could be back calculated to be ~20 nm at the top of the rod and ~50 nm at the bottom of the rod. The fin width at the bottom of the rod could be further verified by the measurements of fin width from Fig. II-16 (a). Due to the tapering of the rod, the top view image should indicate the maximum fin width which corresponded to the fin width at the bottom of the rod.

Averaged measurements over all the fins in Fig. II-16 (a) indicated that the fin width at the bottom of the rod was ~50 nm in agreement with the measurements made from Fig. II-15. From the measurement, the sidewall angle of the fin was measured to be ~ 2.5°. Previously, vertical FIB milling was used to fabricate a three-dimensional (3D) optical metamaterial with negative refraction at visible frequencies [70]. The side wall angle reported was 4.3°. Similarly, photonic crystals fabricated using vertical FIB milling reported sidewall angles varying between 5° to 1.5° [71]. Therefore, the measured sidewall angle was found to be in the same range as the previously reported sidewall angles.

From the reported fin width variation and slope, the fin width at the center of the rod was calculated to be ~35 nm and would exceed the design value of 20 nm by

15 nm. This changed the SC device performance as the minimum value of scattering cross-section would blue shift down to lower wavelengths. Due to this, the figure of merit *SR* might also decrease implying that the SCD would only partially suppress the scattering. As explained previously, the principle of operation of the device was to surround a dielectric volume (area) by a certain amount of plasmonic volume (area) so that the oppositely induced dipoles in the dielectric and plasmonic materials cancel each other. From the fabricated structure, it is observed that the dielectric volume (rod) is still surrounded by a certain volume of plasmonic material and thereby we still expect the SCD to function with degradation in performance. The increase in volume could be calculated to be approximately 38 %.

Also, we found that the sidewall angle could be further reduced in rods with increased diameters showing that the fabrication method holds promise. Fig. II-17 shows scanning electron microscope images of such fabricated structures with larger rod diameter and increased fin widths. The devices would still function as scattering cancelation devices at wavelengths other than 1550 nm.

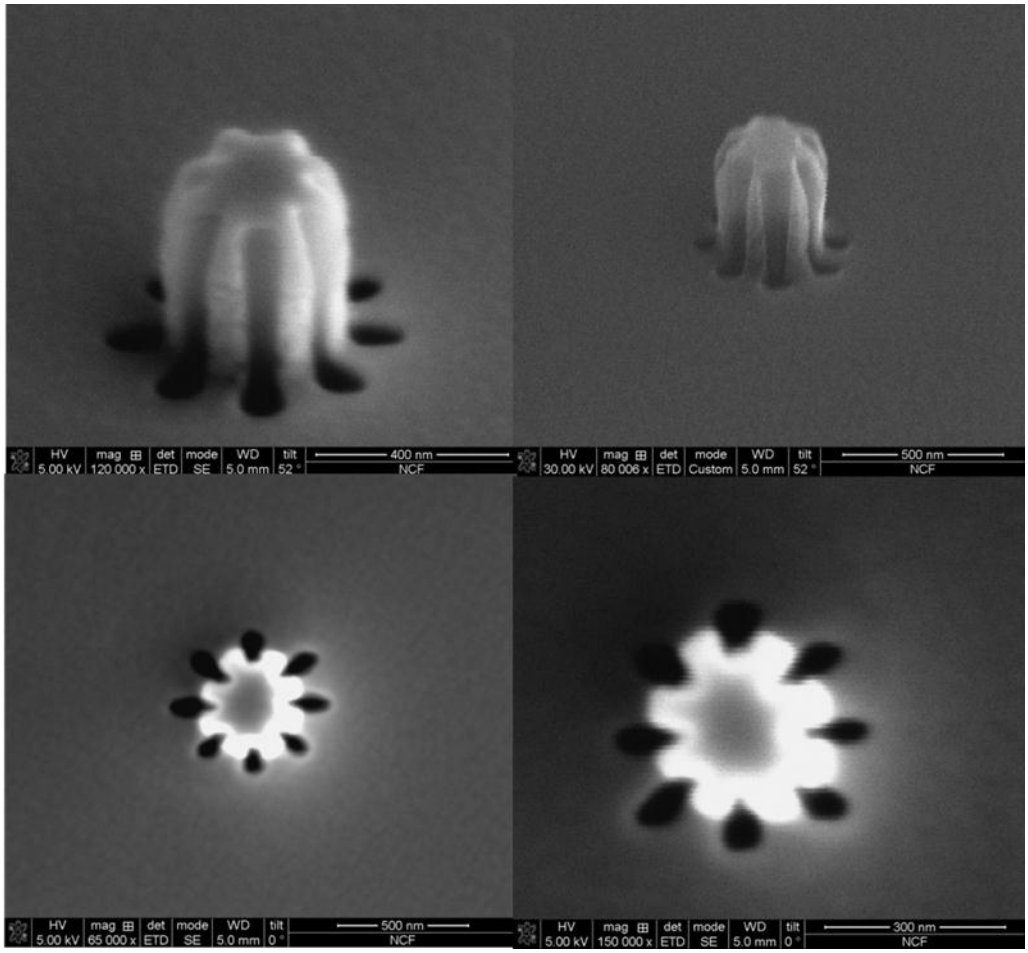

Figure II-17: Scanning electron micrographs of fabricated devices with larger diameter and increased fin widths showing reduced sidewall angles.

The penultimate step of the fabrication process included the removal of the gold from all areas of sample excluding the plasmonic gold nanostructure. In order to protect the gold nanostructure from the chemical etchant, a thin layer of silicon dioxide was coated over the combined silicon nanorod and gold grating structure using the probe deposition system within the focused ion beam machine. It is for this reason that in the effective medium analysis we assumed a silicon dioxide background medium. Fig. II-18 shows scanning electron micrograph of the structure

after coating with a thin layer of silicon dioxide and the thickness of the deposited layer was estimated to be ~20 nm after comparing with the rod size in Fig. II-16 (a).

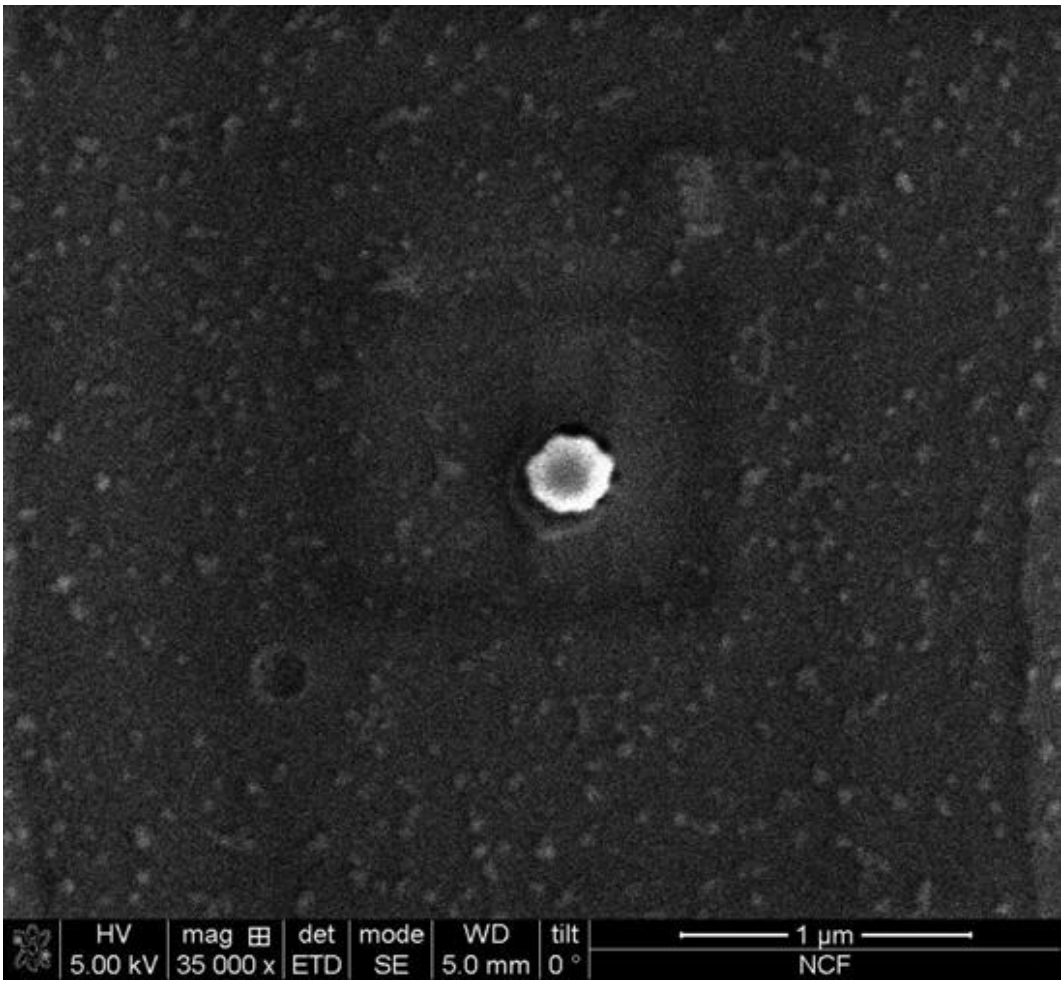

Figure II-18: Low magnification scanning electron micrograph of the scattering cancelation structure after silicon dioxide coating.

In the final step of the fabrication procedure, the entire sample was coated with a thin film of SU8 photoresist. After curing and hard bake, the sample was cleaved to expose the silicon waveguide to enable butt-coupling of light from a fiber. The thickness of the SU8 layer was estimated to be 370 nm.

In addition to the SCD sample, a control sample was also fabricated to compare with the performance of the SCD. The control sample consisted of a bare silicon rod with diameter 240 nm. The total diameter of the SC device structure including silicon dioxide coating was 250 nm and hence the diameter of the bare rod was chosen to be close to 250 nm. Scanning electron micrographs of the bare rod control sample is shown in Fig. II-19.

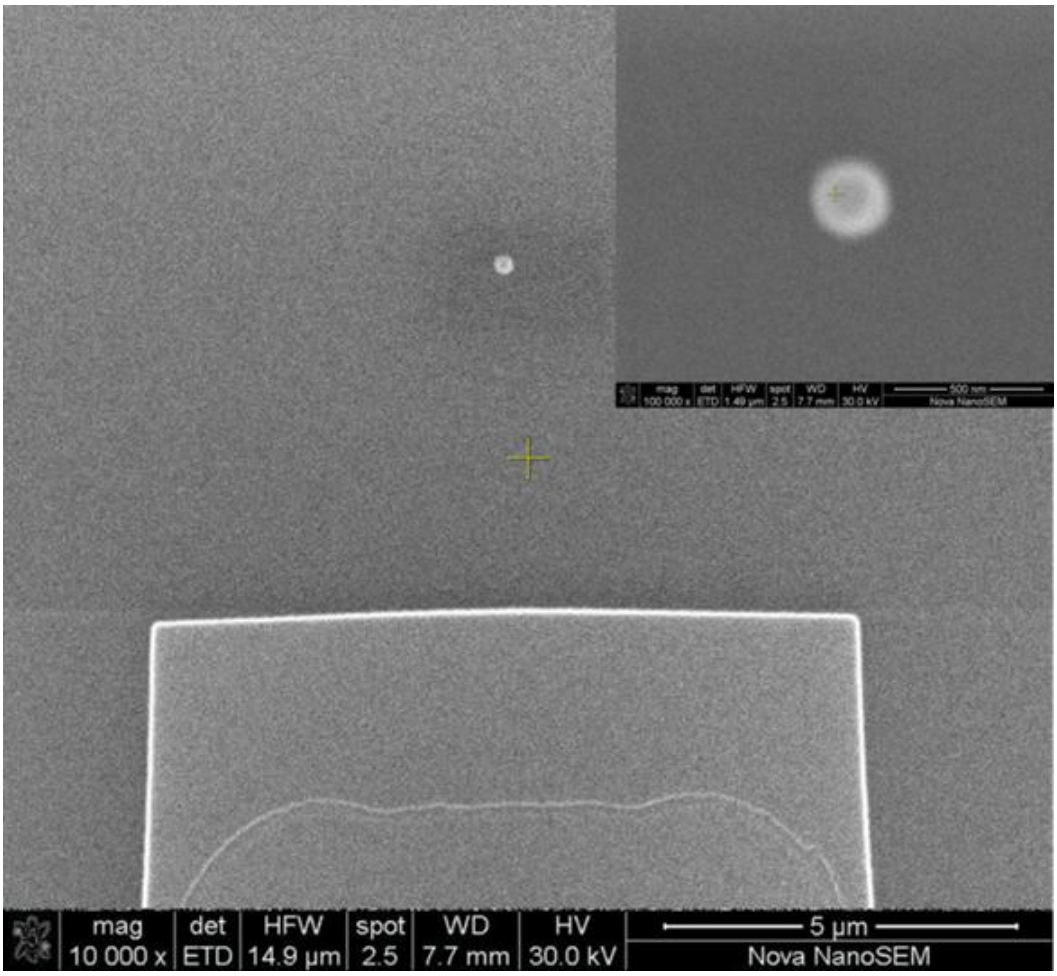

Figure II-19: Scanning electron micrograph showing the fabricated bare rod as well the 10 µm wide input waveguide. Inset shows a higher magnification image of the bare rod.

In order to obtain an estimate of the scattering reduction performance we ran numerical simulations using COMSOL in a 2D geometry. The structural and refractive index parameters were re-estimated based on the analysis of fabricated structure. The dielectric constants of bulk silicon were obtained from [4] and the refractive index data of SU8 was obtained directly from the manufacturer [72]. As the device was fabricated on 340 nm thick silicon on insulator wafer with SU8 over coating, the effective index of the guided TM_{01} mode was obtained at various wavelengths. The obtained wavelength dependent effective index was used to describe the optical properties of the nanorod in a 2D geometry. Although such thin films with low refractive indices do not support a bounded mode, wave propagation such media is still possible with a weak unguided mode that could be described by a small range of effective indices. An 'effective' refractive index of 1.48 was obtained by conducting NSOM measurements on a test sample. By direct visualization of light propagating through the SU8 medium, the phase information from many measurements was averaged to obtain the 'effective' index. Subsequent investigations using numerical simulations revealed little difference between the simulations with 'effective' index of 1.5 and 1.48 respectively. However, the value of 1.48 was used as it was measured experimentally.

Plotted in Fig. II-20 (a) is a comparison of the scattering cross sections for SCD rods with averaged silicon rod diameter of 185 nm and measured gold thickness of 13 nm for various measured fin widths. In addition to comparing the averaged rod diameter and measured fin widths, we compare scattering cross-sections for the rod

diameter and fin width combinations measured at various points along the rod height. The comparison is plotted in Fig. II-20 (b). In both cases, for comparison, the scattering cross-section of a bare rod with diameter 240 nm is also plotted.

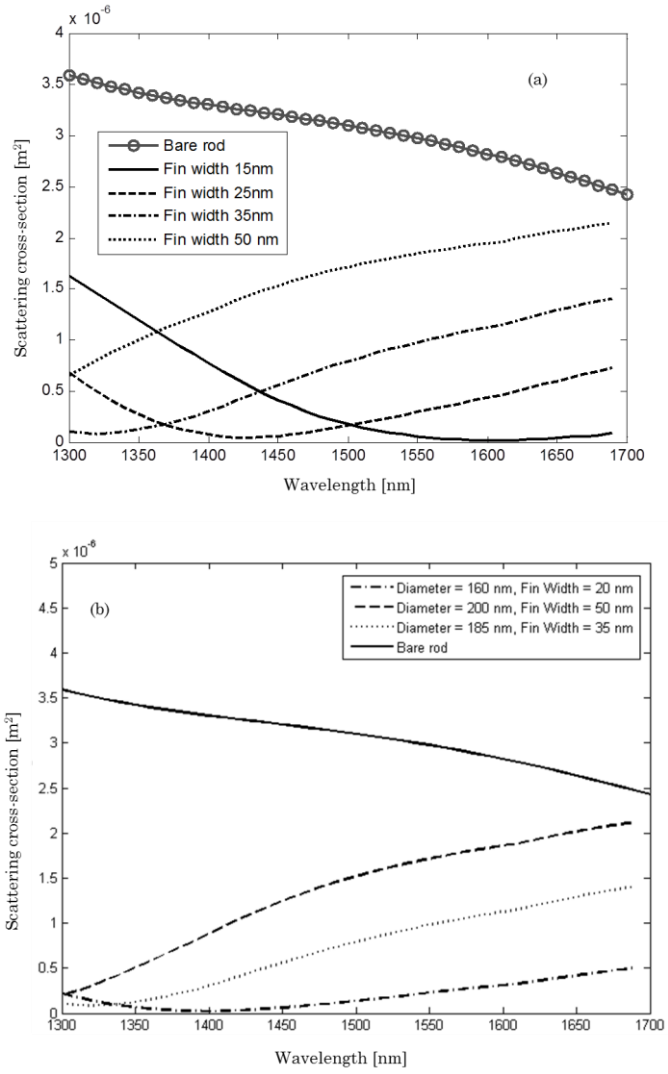

Figure II-20: Comparison of scattering cross-section obtained from simulations of SCD rod with averaged diameter of 185 nm and measured thickness of 13 nm for varying fin widths from 15 nm to 50 nm (b) Plot of scattering cross-section for rod diameters and fin widths values measured at various points along the rod height. In both cases, the scattering cross-section of a bare rod with diameter 240 nm is also plotted for comparison. The *SR* values for each curve are tabulated in Table II-2.

From Fig. II-20 (a), the response of the averaged fin width of 35 nm has blue shifted by around 200 nm compared to the design wavelength of 1550 nm. Table II-2 lists the values of *scattering reduction* for SC devices with the given rod diameter and fin width combinations taken from the curves plotted in Fig. II-20 (a, b) in relation to the scattering cross-section of the bare rod of diameter 240 nm. The wavelength for comparison is 1550 nm. The gold thickness is 13 nm in all cases.

Rod Diameter (nm)	Fin Width (nm)	Scattering Reduction (dB)
160	20	11.2
185	15	17
185	25	10
185	35	4.8
185	50	2.1
200	50	2.4

Table II-2: Scattering Reduction at 1550 nm for various Rod diameter and finwidth pairs extracted from Fig. II-20. The gold thickness in all cases was 13 nm.

As seen in Figs. II-14 and II-15, the variation in rod diameter and fin width with height was uniform and linear without any abrupt jumps. Therefore, the scattering cross-section for the entire structure would lie within the bounds set by the scattering cross-section curves for rod diameter & fin width sets of (160 nm, 20 nm) and (200 nm, 50 nm), i.e between ~11.2 dB to ~ 2.4 dB. As seen from Fig. II-20

(b), the scattering cross-section plots for the SCD with measured rod diameter and grating widths are deviated from the plots for the original design. The minima of the scattering cross-section occur at wavelengths below 1420 nm for all the three cases of measured rod diameter and grating widths. However, as seen in Fig. II-25 (b), the scattering cross-section values for the three cases at 1550 nm are well below that of the bare rod indicating that the SC device would have a degraded performance when compared to the wavelengths at which the SR is the maximum (or minima of the scattering cross-section curve).

E. Results of optical characterization and analysis of experimental data

The scattering cancelation device structure was designed such that its performance could be directly visualized using the heterodyne near field scanning optical microscope (H-NSOM). Fig. II-21 shows a cartoon describing the physical process causing the scattering and the expected output from the H-NSOM. The total field is a sum of the incident plane wave and the scattered spherical wave. However, as detectors measure only the electric field squared ($|E|2$), the actual perturbed electric field (E) distribution cannot be directly discerned. The electric field amplitude ($|E|$) and phase distribution can be obtained using a heterodyne interferometry setup.

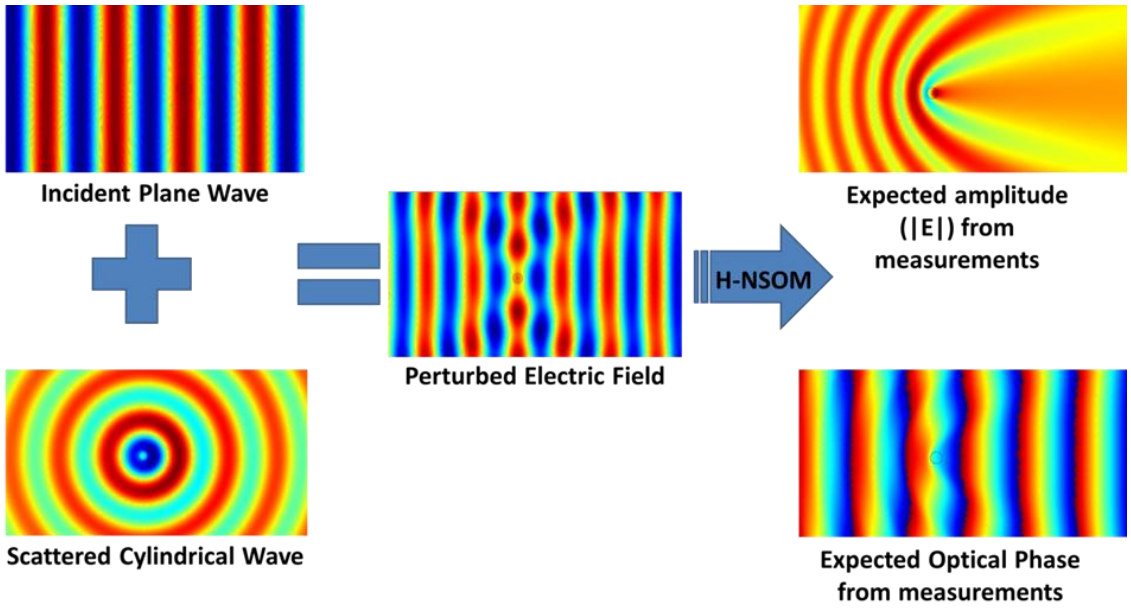

Figure II-21: Cartoon depicting the scattering process and the expected measurement results. The total field is a sum of the incident plane wave and the scattered spherical wave.

We expect the measured field amplitude and phase for the bare rod sample to look like the plots shown on the right hand side of Fig. II-21. The measured amplitude would contain the typical parabolic fringe pattern due to the interference between incident plane wave and scattered cylindrical wave [73].

As mentioned earlier, the concept of invisibility cloaking by scattering reduction has been demonstrated earlier at microwave frequencies [59] and the *scattering reduction* of the cloak was verified by calculating the scattering cross-section from experimentally measured field data. In order to calculate the scattering cross-section, the complex scattered fields and the incident power need to be known accurately. The complex scattered field could be calculated from the incident and

measured total electric field. At optical frequencies, the measured complex scattered field could be obtained using heterodyne interferometry techniques. The exact incident power over multiple sample measurements could be easily calculated at microwave frequencies by proper calibration of the source. The detector collection efficiency can also be more carefully calibrated in microwave frequency measurement setups. However, such conditions would be very difficult to achieve in the proposed optical measurements due to the many uncertainties in measurements.

The bare rod and the SCD samples were fabricated on two different wafers. It would be very difficult to achieve exactly same butt-coupling efficiency in both the two cases due to the two different cleave conditions and manual fiber alignment. Multiple probes of similar aperture dimensions were used to visualize the near-field performance of the SC Device and bare rod and collection efficiency varied among the probes. Due to the probe fabrication technique, the size of the aperture varies widely and this variation affects the wavelength dependent collection efficiency of the probe [18]. Due to these issues, it would not be possible to arrive at a precise value of input power for the two samples and hence the measured scattering cross-section of bare rod and SCD sample could not be calculated accurately. Therefore, the SCD performance would need to be verified by comparison of certain key parameters between experimental and simulation data. From the Fig. II-21, it could be expected that the fringes extracted from the field amplitude data may be used to characterize the scattering performance. In particular, as the fringes contain

information regarding the scattered fields and could be measure accurately, more emphasis was given to the characterization of the fringes.

The relation between the fringe curvature and scattering cross-section is further investigated. Similar to the results of the numerical example presented in Fig. II-4 (b), the SR at 1550 nm of the coated cylinder is plotted in Fig. II-22 (a) for varying cover permittivity with cover thickness of 20 nm. To calculate SR, the scattering cross-section of the coated cylinder was normalized with respect to the scattering cross-section of a bare rod with diameter 240 nm. The SR is seen to have a peak at a cover permittivity of about -18. The cylinder permittivity was chosen to be 8 as it is close to the TM effective permittivity of silicon at 1550 nm and the cylinder diameter was chosen to be 180 nm. From the simulations, the |E| field was plotted and the fringe curves were extracted for various permittivity values. Fringe curves for some selected permittivity values are plotted in Fig. II-22 (d) and the fringe curves are seen to fit a parabolic shape. The fringe curves extracted form simulations were all centered (offset removal) such that the minimum of the parabola occurred at (x, y) = (0,0). The curvature parameter C (in units of m^{-1}), which is indicative of the curvature of the parabola, was calculated from the fringe curves for various permittivities at x = -1 μm. The Fig. II-22 (b) plots the curvature parameter C as a function of the cover permittivity. The data in Figs. II-22 (a, b) were combined and Fig. II-22 (c) plots the SR as a function of the curvature parameter C.

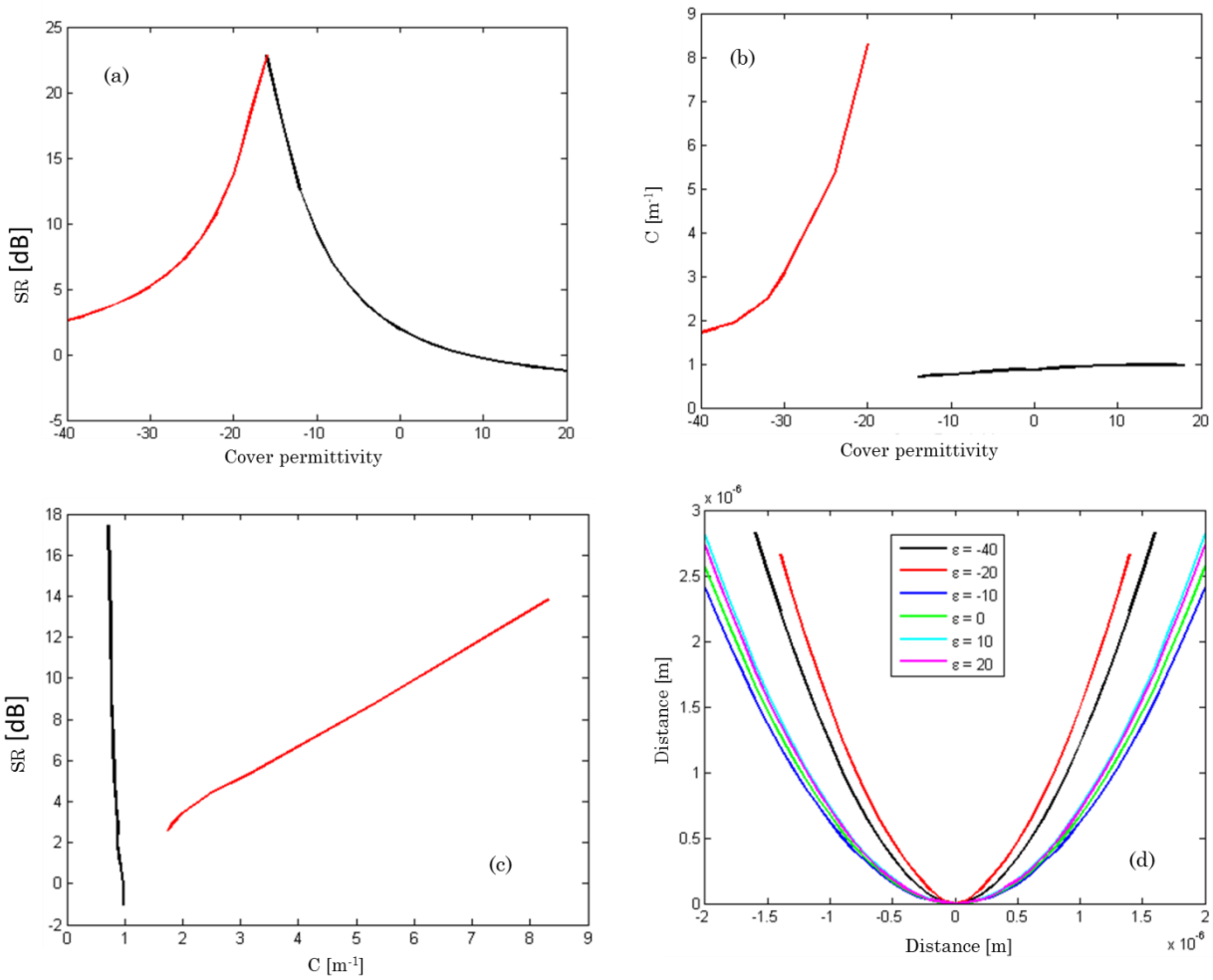

Figure II-22: (a) Plot of scattering cross-section at 1550 nm with varying cover permittivity obtained from simulations of coated cylinder with cylinder permittivity 8. (b) Plot of curvature parameter C as a function of cover permittivity. (c) Plot of SR in dB as a function of the curvature parameter C and (d) plots of fringe curves for various cover permittivities.

In Fig. II-22 (c), the black curve is seen to have a steeper and more negative slope compared to the red curve indicating that the fringe curvature has a more rapid change for cover permittivities greater than -18 and the fringe curvature can

be expected to vary slowly cover permittivities more negative than -18. It is clear from Figs. II-22 (b, c) that the fringe curvature is linearly related to the *scattering reduction* (in dB) and thereby the scattering cross-section of the bare rod/SCD. The analysis presented used a lossless cover permittivity. In practice, the cover permittivity would have some loss. Future work could consider performing the analysis with loss. However, we expect that addition of reasonably small loss would not change the data very much.

The experiment was performed using the Heterodyne-NSOM setup described in Section I-E. All measurements were performed at 1550 nm and a C band laser (1530 nm to 1565 nm) was used as the light source. The polarization paddle in the signal arm in the H-NSOM setup was used to set the polarization of the light which was then butt-coupled into the cleaved sample. Two different sets of aperture NSOM probes were used in the experiments. In the both the sets, a single mode fiber (Corning SM-28) was used to fabricate the NSOM probe. In the first set of experiments with low spatial resolution of ~120 nm, the aperture of the NSOM probe was 200 nm. This resulted in much larger collection efficiency and increased contrast. But in order to characterize the fringes more accurately, the subsequent experiments were performed with higher spatial resolution of ~30 nm. To achieve this, the apertures of the NSOM probes used were 100 nm and 150 nm. This caused a reduction in the collection efficiency but improved the spatial resolution.

In the first set of scans, a large area of 30 μm × 30 μm was scanned. The number of scan points was 256 × 256 thus leading to a spatial resolution of ~120

nm. Both the bare rod and SCD sample were scanned using the same probe with an aperture of 200 nm and the output power of the laser was kept constant at 10 mW for both the scans. The sensitivity of the lock-in detector was maintained constant at 20 mV for both the scans. The Figs. II-23 (a, b) plot the heterodyne detector amplitude output (in Volts) proportional to the absolute value of the measured electric field. Both the results have been plotted with the same color scale also shown. Both the samples were scanned at a wavelength of 1550 nm.

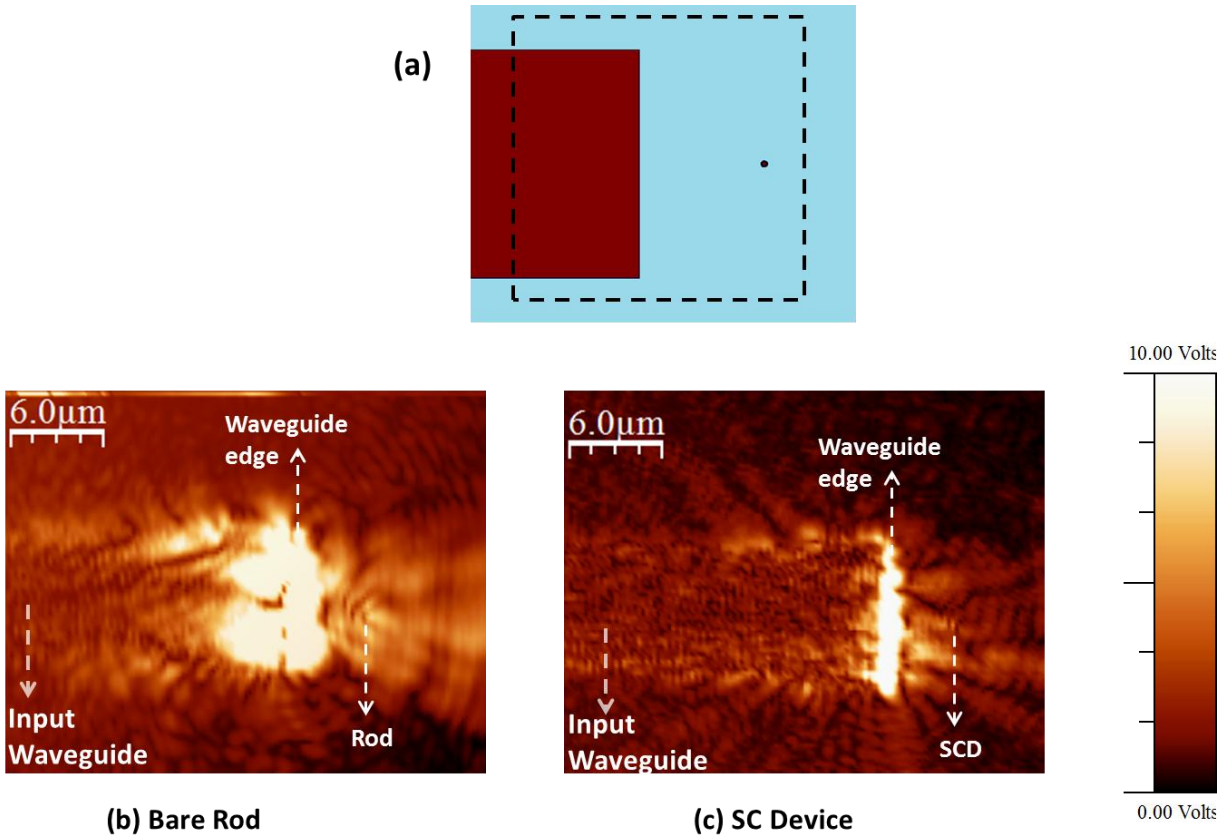

Figure II-23: (a) schematic of area scanned (b) NSOM scan results for the bare rod sample at 1550 nm (c) NSOM scan results for the SCD sample at 1550 nm

In both the cases of the bare rod (Fig. II-23 (a)) and SCD rod (Fig. II-23 (b)), the light propagation in the waveguide is clearly seen. The bright spot at the tip of the waveguide was caused by the out of plane light scattering due to the discontinuity at the waveguide edge. In the bare rod results in Fig. II-23 (a), the large light scattering due to the bare rod can be clearly seen and compared with the scattering image shown in Fig. II-21. The exaggerated bending of the fringes and the forward scattered component can be clearly distinguished. In addition, the large back-scattering also contributes to the bright spot near the edge of the waveguide. As the same probe was used to measure both samples, it is important to mention that the bare rod sample was scanned first using the probe.

In contrast, the result for the SCD in Fig. II-23 (b) does not show an exaggerated bending of the fringes as seen in the bare rod results. This indicates that the fringes produced due to scattering by SCD were different from the fringes due bare rod scattering. As the fringes are a direct consequence of the scattering properties, it could be concluded that the SCD takes on different scattering properties compared to the bare rod.

In order to investigate the effect further, we performed high resolution scans over small areas close to the rod/device. The Figs. II-24 (a, b) show the heterodyne detector amplitude output (in Volts) proportional to the absolute value of the measured electric field. Both the results have been plotted with the same color scale also shown. Both samples were scanned at the same wavelength of 1550 nm.

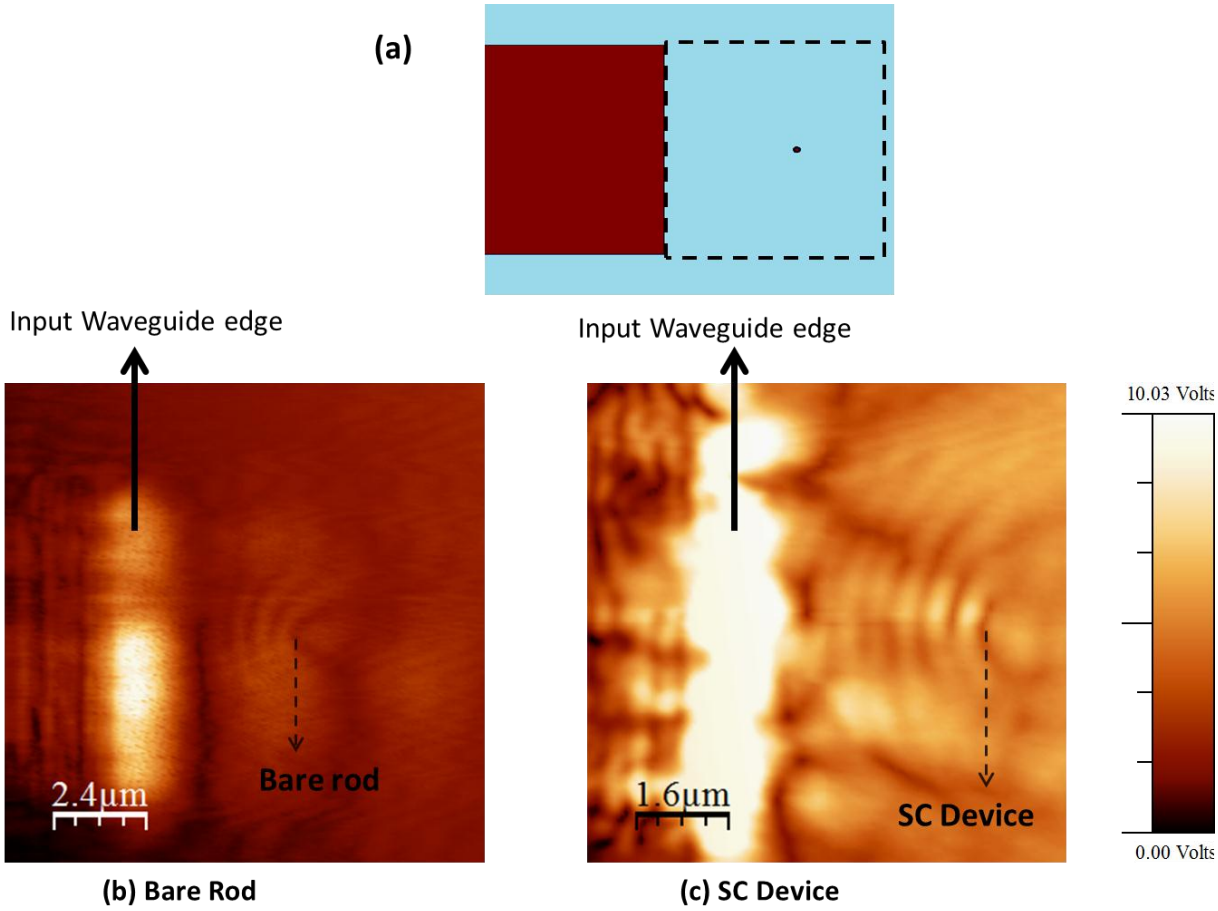

Figure II-24: (a) schematic of area scanned (b) NSOM scan results for the bare rod sample at 1550 nm (c) NSOM scan results for the SCD sample at 1550 nm

The bare rod results in Fig. II-24 (a) was obtained over the scan area of 12 µm × 12 µm. The number of points in the scan was 300 × 300 giving a scan resolution of 40 nm. The output power of the laser was 5 mW and the detector sensitivity was set to 1 mV. The SCD result in Fig. II-24 (b) was obtained over the scan area of 8 µm × 8 µm. The number of points in the scan was 256 × 256 giving a scan resolution of ~31 nm. The output power of the laser was 10 mW and the detector sensitivity was

set to 10 mV. Both the bare and device scans were performed using two different NSOM probes of apertures 150 nm and 100 nm respectively.

In order to compare with experimental results, two dimensional $|E_z|$ field plots extracted from the simulations are plotted in Figs. II-25 (a, d) for the bare rod and SC device respectively.

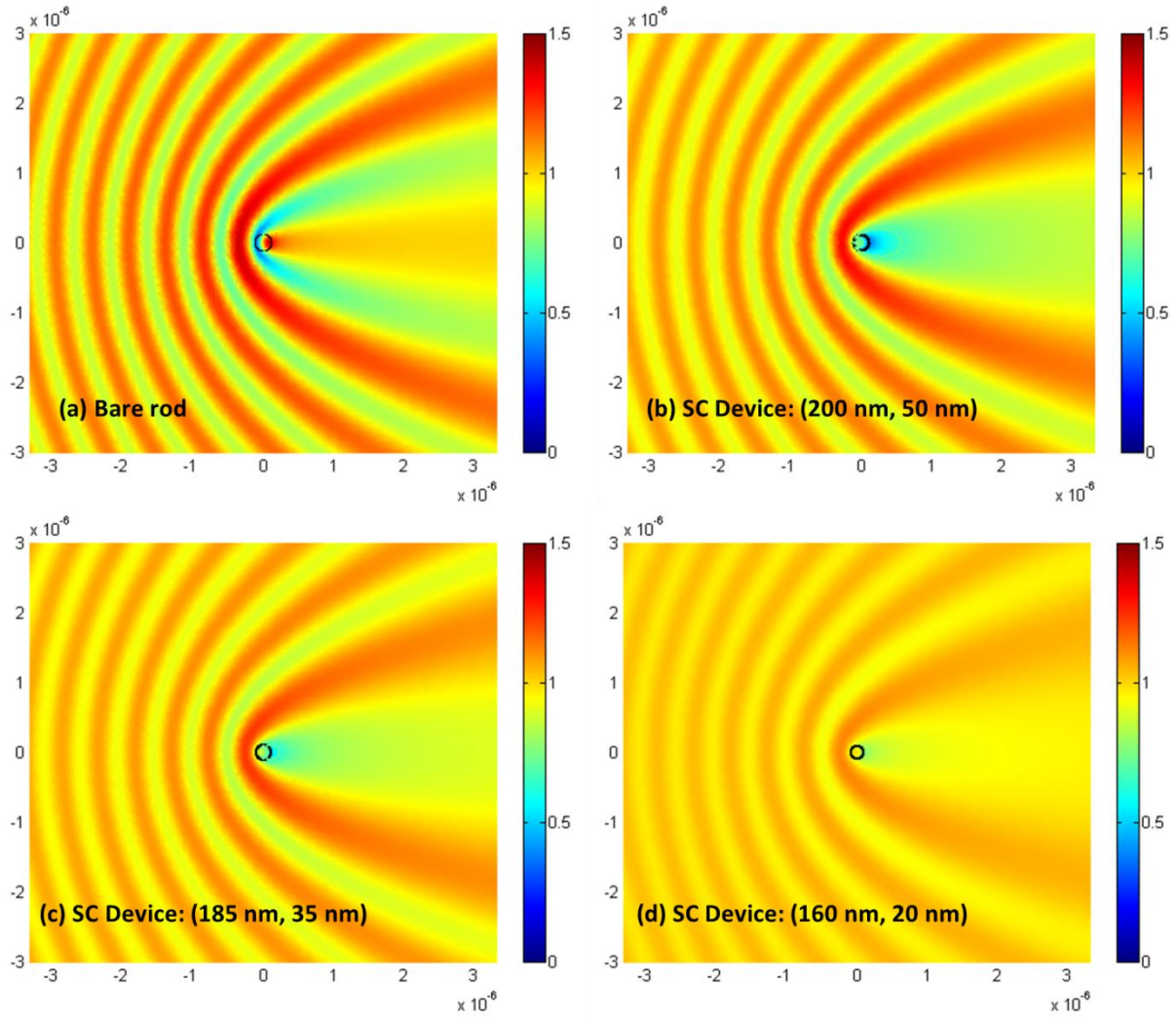

Figure II-25: Two dimensional field plots of $|E_z|$ extracted from simulations for (a) bare rod (b-d) SC Devices with measured rod diameter, grating width cases of (200 nm, 50 nm), (185 nm, 35 nm) and (160 nm, 20 nm) respectively.

Fig. II-25 (a) plots the $|E_z|$ field extracted from simulations for the bare rod of diameter 240 nm. Figs. II-25 (b-d) plot the $|E_z|$ field extracted from simulations for the SC device with measured rod diameter, grating width cases of (200 nm, 50 nm), (185 nm, 35 nm) and (160 nm, 20 nm), respectively. Additional parameters used in simulations were: silicon dioxide coating thickness of 20 nm, silicon dioxide refractive index of 1.45 and background medium index of 1.48. An observation of Fig. II-25 (a-d) reveals a difference in the curvature of the fringes between the bare and SC device cases. This difference in curvature was ascribed to the difference in scattering properties between the bare rod and SC device. As the first fringe behind the rod/SCD is the closest to the rod/SCD, we could expect that the first fringe would carry significant information in terms of curvature to help discern between the bare rod and SCD cases. Therefore, we analyze the first fringe very carefully by extracting the first fringe curve from both experiment and simulation data.

Fig. II-26 (a) plots the first fringe curves extracted from experimental data and simulations for the SC device. The simulations were performed using the measured structural parameters (rod diameter and grating width) and the results have been plotted in Figs. II-25 (b-d). The fringe curves extracted from the simulations of the rod diameter and grating width cases of (200 nm, 50 nm) and (185 nm, 35 nm) are different from the results from simulations using rod diameter and grating width case of (160 nm, 20 nm) and the fringe curve extracted from simulations using rod diameter and grating width case of (160 nm, 20 nm) agrees with the experimental data.

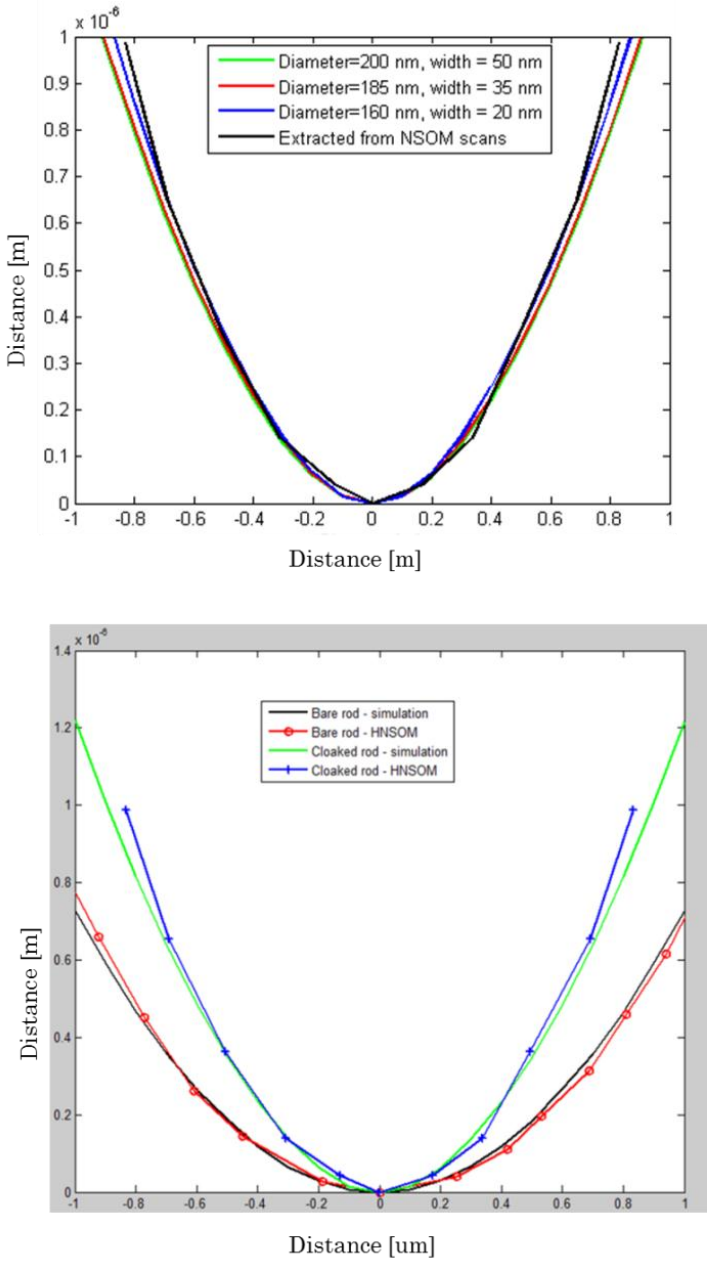

Figure II-26: (a) Comparison of first fringe curves extracted form NSOM scan data and simulations using measured structural parameters for the SC device. (b) Comparison of the first fringe curves extracted from simulation and experimental data for the bare rod and SC device

Fig. II-26 (b) plots the first fringe curves extracted from the simulation and experimental results for the bare rod and SC device. For the SC device, the fringe

curves obtained from simulations were extracted numerically from the simulation using the measured rod diameter of 160 nm and grating width of 20 nm. For the bare rod, the fringe curves were obtained from the simulations using measured bare rod diameter of 240 nm. The fringe curves obtained from experiments were manually extracted from the images in Fig. II-24 (a, b) for the bare rod and SC device respectively. Five independent manual curve extractions were performed and then arithmetically averaged to obtain the final fringe curve.

The fringe curves for both the bare rod and SC device extracted from simulation and experimental results agree well with each other and the obvious difference in curvatures confirm that the bare rod and the SCD take on different scattering properties. The fringe curves extracted from SCD simulations for parameter sets of (200 nm, 50 nm). (185 nm, 35 nm) and (160 nm, 20 nm) have a curvature parameter C roughly 2.78, 2.99 and 3.32 respectively. The curvature parameter C for bare rod fringe curves extracted from simulations is roughly 1.

Another approach to verifying the fringe information is to study cross-sectional plots passing through the center of the rod/device. A vertical cross-section plot would re-state the fringe curve comparison plots in a different way and are shown in Fig. II-27. The lines on the plot indicate the plane from which the cross-section data was extracted from the two dimensional field amplitude data. Fig. II-27 (a, b) plot the cross-sections from the $|E|$ plot obtained from simulations for the bare rod and SC device cases respectively. The distance between the peaks is ~1.5 μm for the bare rod results and ~1 μm for the SC device results. From the experimental data,

distance between the peaks is ~1.6 µm in the bare rod case and ~1 µm in the SCD case.

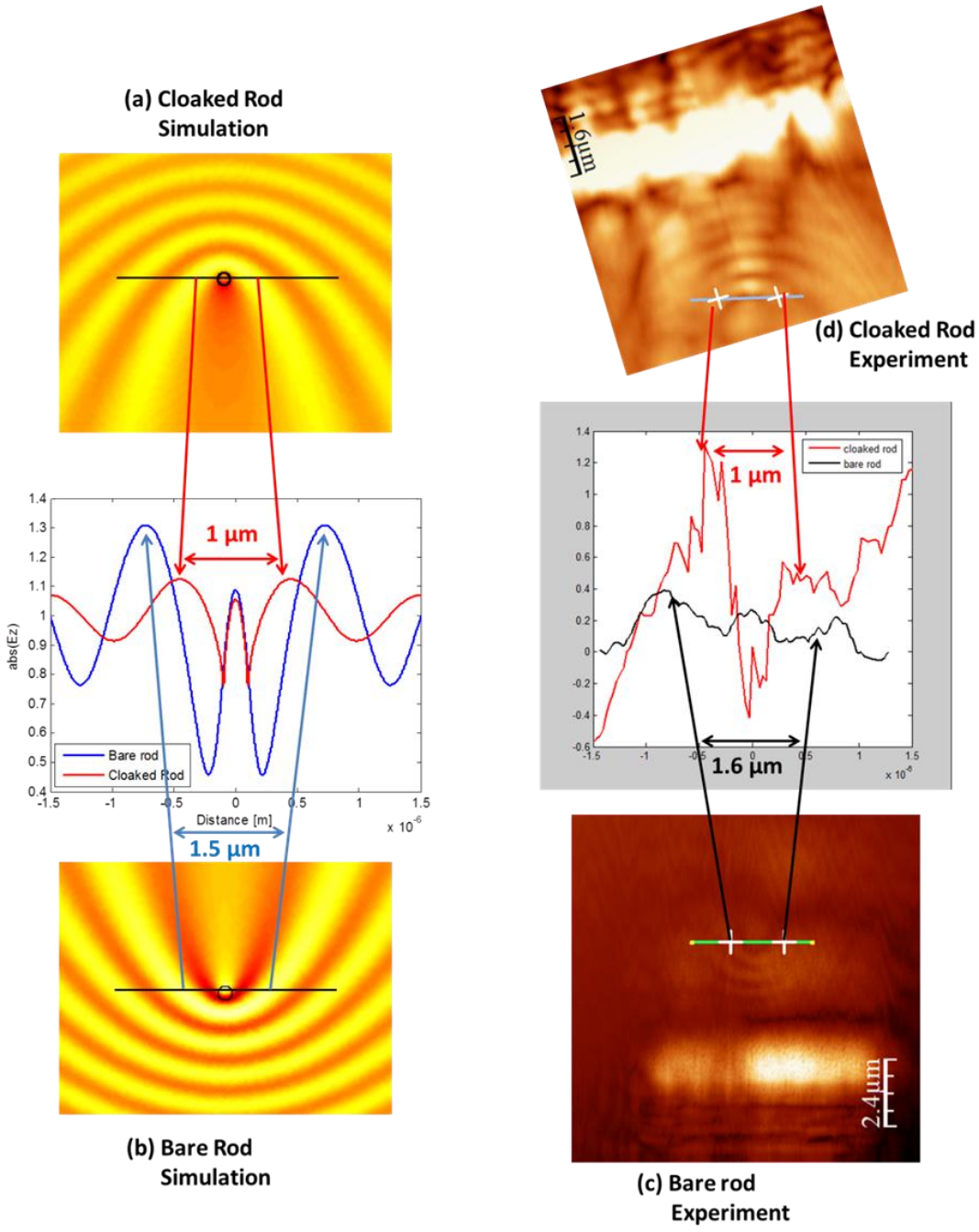

Figure II-27: Study of the cross-section plots extracted from experimental and simulation results for bare rod and SC device.

From a horizontal cross-section plot, we can obtain the distance between the rod and the first fringe. In addition, distances between the first fringe and subsequent fringes could also be estimated. The distance between the center of the rod and first fringe peak position varied between 200-400 nm between the SC device and bare rod. Since the spatial resolution used in the H-NSOM scans was about 30 nm, the fringe positions could be resolved reasonably well enough to enable comparisons with simulation data. The cross-section data extracted from simulation and experiment are compared in Fig. II-28. Fig. II-28 (a) compares the cross-section data for the SC device. Plotted together are the experimental data and the data extracted from simulations using the three measured rod diameter and grating cases. The data extracted from simulations using measured rod diameter and grating width of (160 nm, 20 nm) agreed very well the experimental data and was also much different than the simulation data using measured rod diameter and grating width cases of (200 nm, 50 nm) and (185 nm, 35 nm). These two data sets have been re-plotted in Fig. II-28 (b). Fig. II-28 (c) compares the cross-section data for the bare rod extracted from simulations and experiments. Fig. II-28 (d) compiles the simulation and experimental data for the bare rod and SC device. In general, the cross-section data obtained from simulation and experimental data are shown to have excellent agreement with each other.

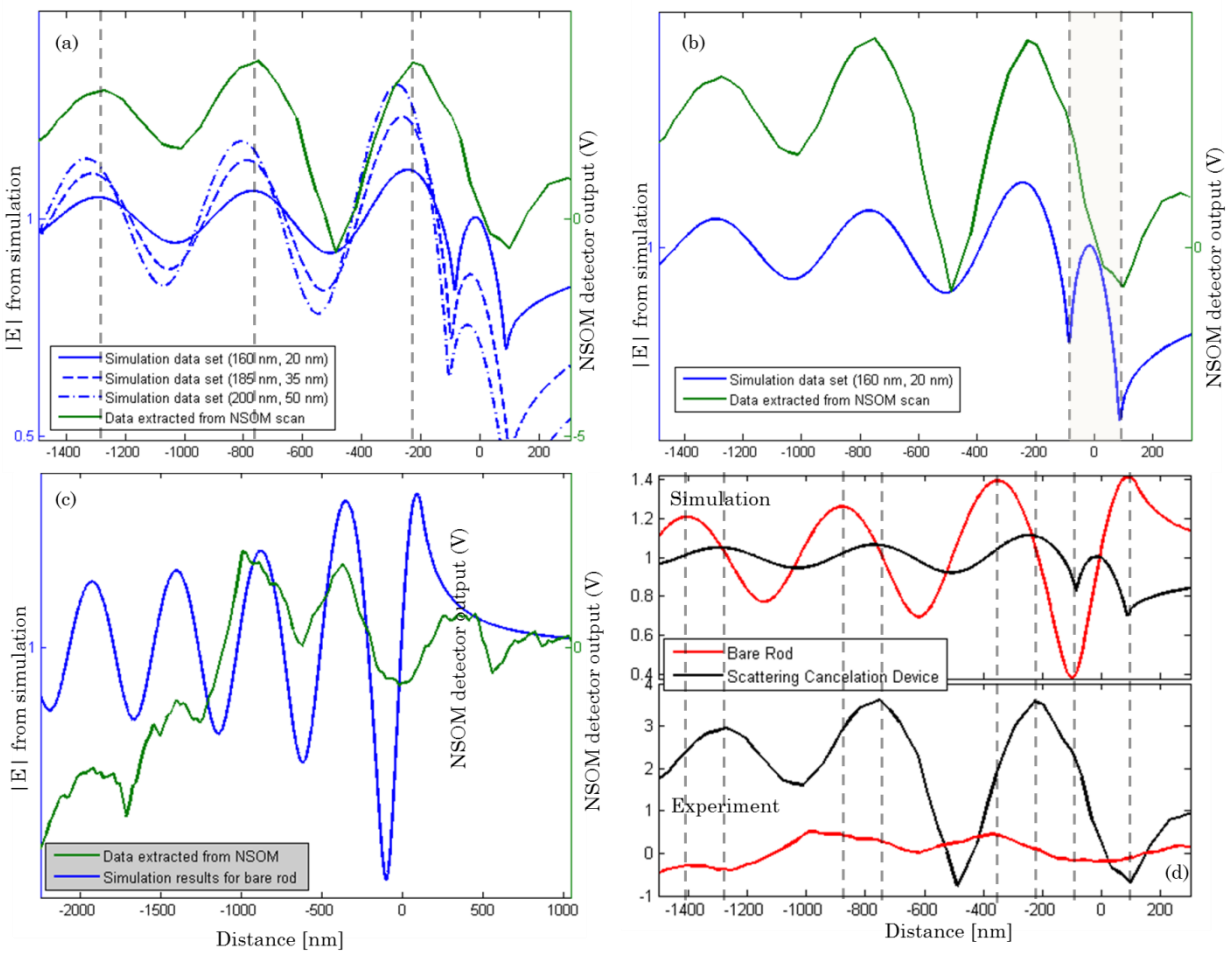

Figure II-28: Plots of cross-section data extracted from experiment and simulation data (a) Plot comparing the experimental data extracted from NSOM and simulations for the SC device (b) Plot comparing the data extracted from NSOM scans and those extracted from simulations for rod diameter 160 nm and grating width 20 nm. (c) Comparison of cross-section data extracted from simulation and experiment for the bare rod (d) Comparison of cross-section data for bare rod and SC device extracted from simulations and experiments.

In Fig II-28 (b), the sharp dips (marked by the dotted lines) in the field amplitude plots are due to the presence of the metal grating as the field value reduced at those points due to the boundary condition. The dips could be clearly observed in both the simulation and experimental cross-section data. From the

experimental data, the distance between the dips is ~200 nm and corresponds to the combined thickness of rod (average diameter 185 nm) and gold layer (average thickness of 26 nm) of 210 nm.

In order to choose the correct cross-section plane in the experiment, the topology scan was also considered. The SC device was very lightly visible in the topology scan as a slight bump and that was sufficient to help choose the correct cross-section passing through the rod. This is seen in the horizontal cross-section data extracted from bare rod H-NSOM scan shown in Fig. II-29. Fig. II-29 (a, b) plot the NSOM signal and topology signal from bare rod scan and Fig. II-29 (c, d) plot the NSOM signal and topology signal from SC device scan.

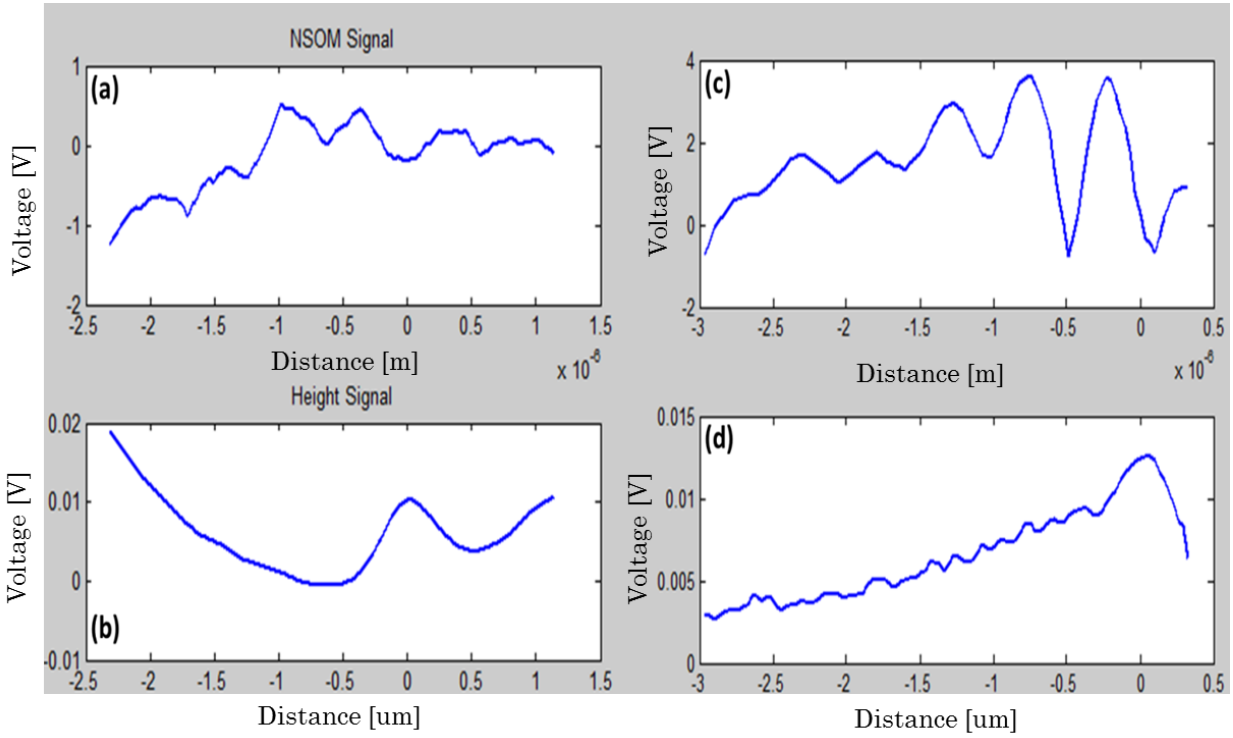

Figure II-29: Cross-sectional data extracted from NSOM and topology scan data. Fig. II-29 (a, b) plot the NSOM signal and topology signal from bare rod scan and (c, d) plot the NSOM signal and topology signal from SC device scan.

From the cross-section data for the SC device plotted in Fig. II-28 (b), we observe that there is a very slight misalignment in the first fringe position. The peak of the first fringe occurs at x ~ -250 nm from the simulation data and x ~-230 nm from the experimental data. This difference of ~20 nm between the experiment and simulation data is smaller than the spatial resolution and could be treated as experimental error. In addition, from the topology signals plotted in Figs. II-29 (b, d), it can be observed that the SU8 thickness varies non-uniformly close to the rod/SCD. This non-uniform variation in the background medium could have also caused the very slight difference in the fringe position. Despite the small difference, the data from experiments agrees well with the data extracted from simulations.

From the presented analysis, we find that the key characteristics of the first fringe extracted from simulation and experiments agree well. In particular, the contrast in fringe curvature seen between the fringe curves extracted from bare rod data and SC device data for both simulation and experimental data indicate that the bare rod and SC device both have different scattering cross-section properties. Two-dimensional simulations were performed on the SC device whose structural parameters were extracted from scanning electron micrographs on fabricated devices. These agreements between the experimental results and theoretical predictions strongly suggest that the scattering cancelation device has a reduced scattering cross-section compared to the control sample. From simulations on the structure with measured rod diameter 160 nm and grating width 20 nm, it was calculated that the SC device could reduce the scattering by up to 11 dB.

CHAPTER III

TUNABLE FANO RESONANCE IN PLASMONIC NANOSTRUCTURES

A. Introduction

The field of plasmonics is mainly concerned with the study of light interactions at metal-dielectric boundaries. The free electrons at the surfaces of metal films are coupled to the electromagnetic field and exhibit characteristic resonances. Typically, plasmonic materials have resonances in the visible frequencies as the plasma frequency of metals lies in the ultra-violet regime. The condition for existence of surface plasmons is that the real part of dielectric function of the material be less than zero, $\mathrm{Re}\{\varepsilon\}<0$ and the surface plasmon resonance would be prominent for small losses ($\mathrm{Im}\{\varepsilon\}<<-\mathrm{Re}\{\varepsilon\}$). This condition is naturally satisfied by metals at frequencies below their plasma frequencies. However, artificial electromagnetic surfaces could be engineered to mimic the behavior of surface plasmons at virtually any frequency. These artificial materials, also called as spoof or designer plasmonic materials have been demonstrated at both microwave [74, 75] and terahertz frequencies [76, 77]. Plasmonics is a very rich and well developed area of research and many texts [78, 79] and review articles have been published [80-82]. Readers are referred to the references for further information on plasmonics and its applications. In this chapter we are mainly concerned with tunable Fano resonances in plasmonic

nanostructures fabricated on flexible substrates. We present details regarding the design, fabrication and characterization of the tunable Fano resonance.

Our study is focused on the complex interactions between various plasmonic resonances. Plasmonic nanostructures may support localized surface plasmon resonances which generally depend on their shape and size [78]. The plasmonic resonance in a nanoparticle of size a could be analyzed by electrostatic approximations provided that $a << \lambda$. For example, a could be the diameter of a spherical nanoparticle or the largest side of a triangular particle. When $a << \lambda$, the incident harmonic electromagnetic field would be nearly constant across the volume of the particle and therefore the electrostatic approximation would be valid. For simplicity, we consider a spherical particle since exact solutions could be easily obtained using spherical harmonics.

Consider a homogenous, isotropic sphere placed in an arbitrary medium of permittivity ε_m. The incident harmonic field is approximated to be a uniform static electric field along the z direction shown in Fig. III-1.

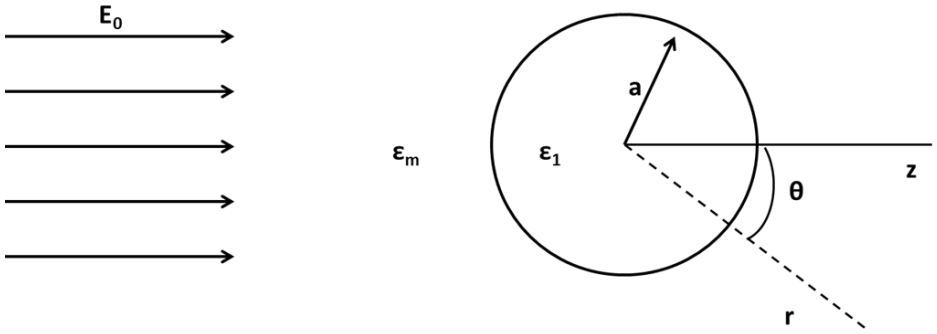

Figure III-1: Schematic of the sphere of radius a in an electrostatic field. The field is oriented along the z direction. The permittivity of the sphere is ε_1 and that of the background is ε_m.

The incident electric field is given by,

$$\mathbf{E}_0 = E_0 \hat{e}_z \tag{3.0}$$

Let the sphere have a permittivity of ε_1 and be different from the background permittivity. This induces a charge on the surface of the sphere and distorts the incident field. The scalar electric potentials in each medium would satisfy the Laplace equation

$$\nabla^2 \Phi_1(r,\theta) = 0 \ \ for\ (r < a)$$

$$\nabla^2 \Phi_2(r,\theta) = 0 \ \ for\ (r > a) \tag{3.1}$$

And the electric fields in each medium could be obtained by

$$E_1 = -\nabla \Phi_1(r,\theta)\ for\ (r < a)$$

$$E_2 = -\nabla \Phi_2(r,\theta)\ for\ (r > a) \tag{3.2}$$

where, E_1 and Φ_1 are the electric field and scalar potential inside the sphere and E_2 and Φ_2 are the electric field and scalar potential outside the sphere. Due to symmetry, the potentials are independent of the azimuthal angle ϕ. The potentials satisfy the boundary conditions at the sphere-medium interface (at $r = a$),

$$\Phi_1 = \Phi_2$$

$$\varepsilon_1 \frac{\partial \Phi_1}{\partial r} = \varepsilon_m \frac{\partial \Phi_m}{\partial r} \tag{3.3}$$

In addition, we expect that at far enough distances from the sphere, the incident field is unperturbed by the sphere.

$$\lim_{r\to\infty} \Phi_2 = -E_0 r \cos\theta = -E_0 z$$

The following functions are known to satisfy Eqn. (3.1) and (3.3)

$$\Phi_1 = -\frac{3\varepsilon_m}{\varepsilon_1 + 2\varepsilon_m} E_0 r \cos\theta \tag{3.4a}$$

$$\Phi_2 = -E_0 r \cos\theta + a^3 E_0 \frac{\varepsilon_1 - \varepsilon_m}{\varepsilon_1 + 2\varepsilon_m} \frac{\cos\theta}{r^2} \tag{3.4b}$$

The incident field creates a charge distribution on the sphere causing a dipole to be formed along the z direction. The potential of an ideal dipole with infinitesimally small separation between the charges is given by

$$\Phi = \frac{\boldsymbol{p} \cdot \boldsymbol{r}}{4\pi\varepsilon_m r^3} = \frac{p\cos\theta}{4\pi\varepsilon_m r^2} \tag{3.5}$$

where, $\boldsymbol{p}$ is the electric dipole moment.

The field outside the sphere is a superposition of incident field and field of an ideal dipole with charges given by those induced on the sphere. Therefore, we can represent the sphere as an ideal dipole at the origin

$$\boldsymbol{p} = 4\pi\varepsilon_m a^3 \frac{\varepsilon_1 - \varepsilon_m}{\varepsilon_1 + 2\varepsilon_m} \mathbf{E}_0 \tag{3.6}$$

Thus the incident field polarizes the sphere and the polarizability is given as

$$\alpha = 4\pi a^3 \frac{\varepsilon_1 - \varepsilon_m}{\varepsilon_1 + 2\varepsilon_m} \tag{3.7}$$

We have replaced a sphere in an electrostatic field by an ideal dipole whose dipole moment is found using a given polarizability. However, the actual field is time harmonic and the frequency variation enters the dipole model of Eqn. (3.7) through the frequency dependent permittivity values $\varepsilon_1(\omega)$.

The absorption and scattering cross-sections for the dipole and for a plane wave incidence are

$$C_{abs} = k\mathrm{Im}\{\alpha\} = 4\pi k a^3 \mathrm{Im}\{\frac{\varepsilon_1 - \varepsilon_m}{\varepsilon_1 + 2\varepsilon_m}\} \tag{3.8a}$$

$$C_{scatt} = \frac{8}{3}\pi a^6 k^4 \left|\frac{\varepsilon_1 - \varepsilon_m}{\varepsilon_1 + 2\varepsilon_m}\right|^2 \tag{3.8b}$$

where k is the wave number in the background medium [2, 4].

From Eqn. (3.8a) and (3.8b), we can observe that the absorption and scattering cross-sections have different dependences on a and k. For small particles and assuming a << λ, we find that absorption cross-section dominates over the scattering cross-section. However, for larger particles the scattering cross-section would dominate the absorption cross-section due the rapid scaling of the contribution from the radius term a.

An important result is derived from Eqn. (3.8b). The scattering cross-section is observed to have a zero when $\varepsilon_1 = \varepsilon_m$ and as expected, it suggests that there is no sphere present to perturb the field. However, when the denominator is zero, or when $\varepsilon_1 = -2\varepsilon_m$, the polarizability, the absorption cross-section and the scattering cross-section are at resonance and their values are limited by the imaginary part of the permittivity function $\varepsilon_1(\omega)$.

If Im{ε} = 0 or could be neglected, then the condition for resonance may be written as

$$Re\{\varepsilon_1(\omega)\} = -2\varepsilon_m \tag{3.9}$$

Eqn. (3.9) is known as the *Frohlich* condition [78] which represents the localized surface plasmon oscillation of the metal nanoparticle. For any plasmonic nanostructure, Eqn. (3.9) is rewritten as

$$Re\{\varepsilon(\omega)\} = -F(structure)\varepsilon_m \tag{3.10}$$

where $\varepsilon(\omega)$ is the frequency dependent permittivity of the plasmonic material and *F(structure)* is a function of the structure (shape and size) of the plasmonic nanostructure.

As a numerical example, we consider a gold sphere of radius 50 nm in air. The frequency dependent permittivity function was obtained from the data tabulated in [6]. The absorption and scattering cross-sections are plotted in Fig. III-2 (a). The cross-section data was obtained from numerical simulations performed using commercial finite-element software COMSOL. The peak near 520 nm is due to the surface plasmon resonance. The large values of the absorption cross-section at small wavelengths (between 300 nm to 400 nm) are caused by the large loss in gold due to inter-band absorption. As expected, due to the small size, the absorption cross-section dominates the scattering cross-section. The gold nanoparticle is seen to have a surface plasmon resonance at about 540 nm. The field plot of $|E/E_0|$ at λ=540 nm is plotted in the Fig. III-2 (b).

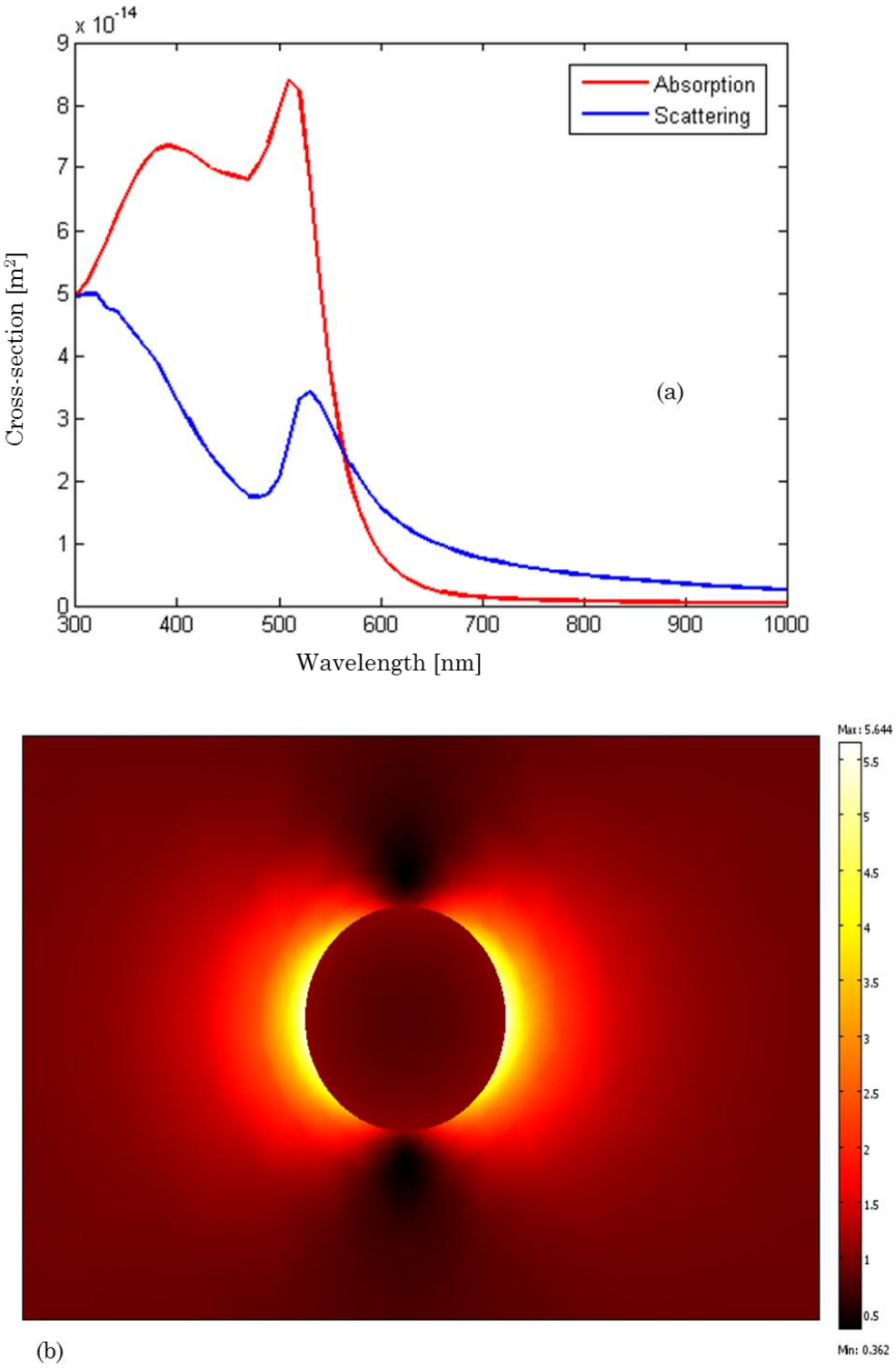

Figure III-2: (a) Plot of absorption and scattering cross-sections of a gold sphere with radius 50 nm in air. (b) Plot of $|E/E_0|$ for a gold nanoparticle of radius 50 nm in air.

The amplitude of electric field in the very close vicinity of the nanoparticle is found to be enhanced roughly 6 times when compared to the incident field amplitude. The field enhancement is a characteristic feature of any plasmonic nanostructure and is commonly referred to as the plasmonic 'hotspot'. The discovery and various applications of plasmonic hotspots have been the driving force behind many plasmonic research initiatives worldwide [80, 81]. The resonance characteristics of an individual nanoparticle are strong functions of the particle shape and size as the plasmonic nanoparticle could be thought of as a deep subwavelength cavity resonator. For example, the fundamental resonance of a nanorod is red-shifted compared to the nanosphere resonance due to a longer cavity length. As the particle sizes are increased, the electrostatic approximation breaks down and the effects of field retardation would need to be considered. Due to the retardation of the depolarizing field inside the particle, the plasmon resonance is red shifted. In addition, increasing particle size also increases the radiation damping of the plasmon resonance leading to broader resonant line widths.

Many interesting phenomena occur when multiple plasmonic resonators are coupled. Similar to many other types of coupled resonator systems, the behavior of a coupled plasmon system can be predicted using methods similar to molecular orbital theory. A heuristic analysis is presented for a dimer (two coupled particles) composed of two nanospheres in Fig. III-3. The nanospheres need not be identical as in the presented example. The system is equivalent to the standard quantum mechanical problem of the formation of a hydrogen molecule from two individual

hydrogen atoms and energy level splitting into bonding and anti-bonding orbitals. In Fig. III-3, the black arrow represents the incident field direction and the white arrow represents the dipole moment of each nanosphere. Let $\boldsymbol{p_a}$ and $\boldsymbol{p_b}$ be the net dipole moments of the anti-bonding and bonding states respectively formed by the vector sum of the individual nanosphere dipole moments.

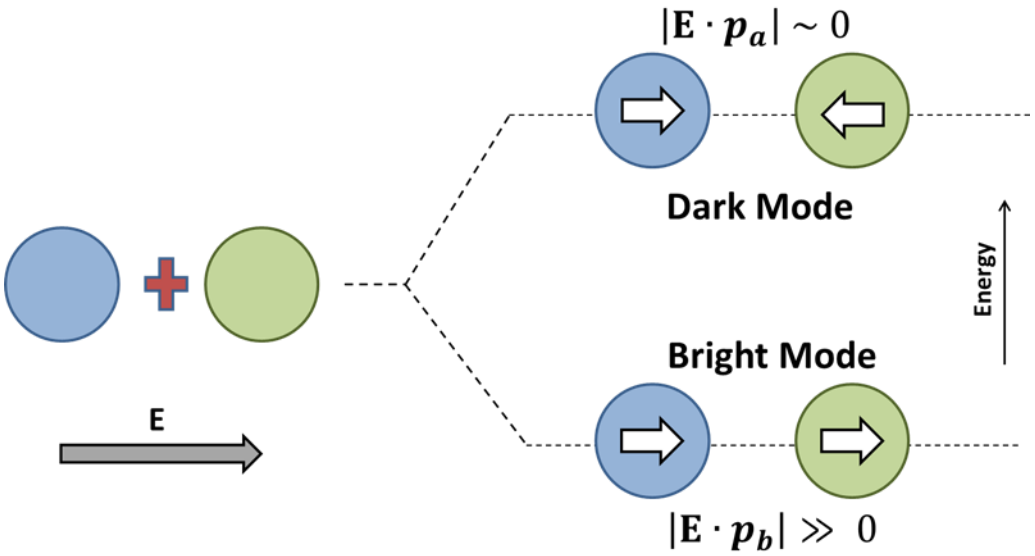

Figure III-3: Schematic for heuristic analysis for a dimer showing formation of anti-bonding and bonding modes also called as dark and bright modes respectively.

As shown in the Fig. III-3 the combination of two isolated nanospheres splits the energy level into two separate levels. The hybridization of the individual nanosphere levels leads to bonding and anti-bonding levels in the dimer [83]. In the bonding level, the individual dipole moments are in the same direction and add up. This causes a large net dipole moment for the dimer mode and is easily coupled to the incident plane wave with the same direction as the dipole causing a strong scattering peak. On the other hand, in the anti-bonding level, the individual dipole

modes are opposing each other and cancel out. This causes a weak or vanishingly small net dipole moment and hence the mode would not couple well with the incident plane wave. Hence this mode is 'dark' to the incident light and is known as a dark mode [84]. The concept of molecular orbital theory has been successfully applied to plasmonic structures and could be used to analyze complicated plasmonic nanostructures [85].

The plasmonic resonance is strongly dependent on the coupling between nanoparticles and the coupling between the individual particles is a function of the gap/spacing between the particles. As an example, a dimer structure composed of two gold spheres was studied numerically using COMSOL. The radius of each gold sphere was 50 nm and the gaps studied were 20 nm and 10 nm. The absorption and scattering cross-sections for the two gap cases are plotted in Fig. III-4.

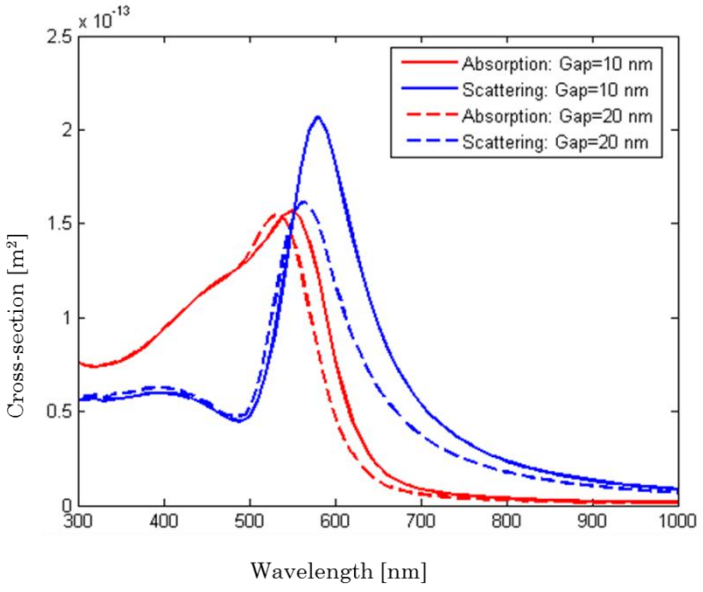

Figure III-4: Comparison of absorption and scattering cross-sections for the plasmonic dimer composed of two gold nanospheres of radius 50 nm and gaps of 10 nm and 20 nm.

The large scattering peak corresponds to the bright or bonding mode and is further verified by the field plots of Fig. III-5. The scattering peak position is a function of gap size. The bright modes for the dimer with gaps of 10 nm and 20 nm are at 565 nm and 580 nm respectively. The absorption cross-sections are smaller than the scattering cross-sections due to the larger size of the dimer system when compared with the individual particle. As expected, the dark modes are not prominently visible in the scattering spectrum for both the gap cases. Figs. III-5 (a, b) plot the field plot of $|E/E_0|$ for the gap cases of 10 nm at 565 nm and 20 nm at 580 nm respectively.

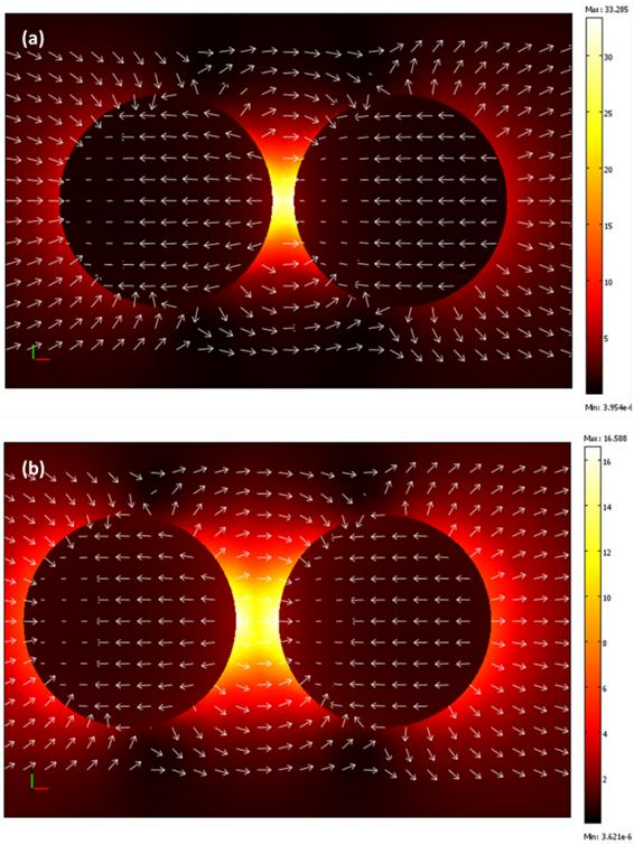

Figure III-5: Field plots of $|E/E_0|$ for the dimer system with gap (a) 10 nm at 565 nm and (b) 20 nm at 580 nm.

In the Figs. III-5 (a, b), the arrows plot the direction of the electric field. For a horizontal polarization of incident electric field, the directions of the arrows inside the spheres indicate that in both cases the dipole moments add up and lead to a large scattering as expected for a bright mode. The field enhancement factors for 10 nm and 20 nm gaps are about 34 and 17 respectively and are clearly a function of the spacing.

While it is obvious that a smaller gap could lead to larger enhancements, it can be observed that the scattering due to the dipole-like bright mode increases with decreasing gap. However, a large scattering would lead to increased extinction of the incident beam as it passes through a medium or film containing these plasmonic nanostructures. On the other hand, the dark mode would have a much lower scattering and imply an increased light transmission. Therefore, it might be useful to engineer a system with large field enhancements and low scattering cross-sections at certain wavelengths. Such nanostructure could have many potential applications in chemical and bio-sensing, optical filters and modulators among others.

B. Fano resonance

Due to its confined nature, the localized surface plasmon oscillator could be modeled well by a simple mechanical oscillator under external harmonic force [78]. The equations of motion are very similar to the constructs developed for the Lorentz oscillator model. The magnitude of the complex amplitude of the oscillation can be shown to have a functional form given by

$$L = \frac{A^2\Gamma^2}{(\omega^2 - \omega_0^2)^2 + \Gamma^2} \tag{3.11}$$

where A is a constant (scale factor) and Γ is the damping associated with a resonance frequency ω_0. The Lorenztian lineshape is the standard response in many physical systems and is a symmetric resonance. A large damping leads to a broadening of the resonance as seen in the plots of Lorenztian lineshape of Eqn. (3.11) plotted in Fig. III-6. The resonance frequency was chosen to be 10 rad/s with the constant A taken to be unity. Radiative damping is one of the primary mechanisms for the broadening of the dipolar response from plasmonic nanostructures and can be accounted for by increasing the damping/loss.

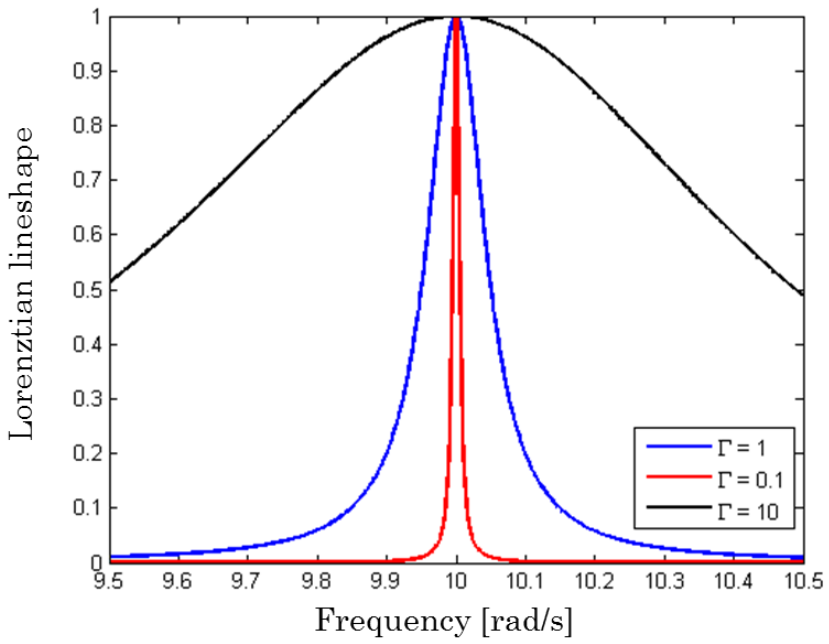

Figure III-6: Plot of the Lornztian lineshape of Eqn. (3.11) for various damping values.

In 1961, Ugo Fano discovered the asymmetric Fano resonance profile while studying the auto-ionizing states of atoms [86]. A simple classical description of the Fano resonance can be found in [87, 88] and the extension to plasmonic structures can be found in [89, 90]. Fano resonance arises from the interferences between a narrow discrete resonance and a broad spectral line. In the classical mechanics analog [88], the Fano resonance is modeled as two coupled harmonic oscillators with losses and coupling strength g. One of the oscillators models a broad spectral line (or a bright mode) with resonance frequency ω_b and a large damping γ_b (the large radiative loss of a bright mode). The other oscillator models a narrow discrete resonance (or a non-radiative dark mode) with resonance frequency ω_d and a low damping γ_d. The broad spectral line is driven by a harmonically varying external force $fexp(i\omega t)$. The model can be schematically described by the arrangement shown in Fig. III-7.

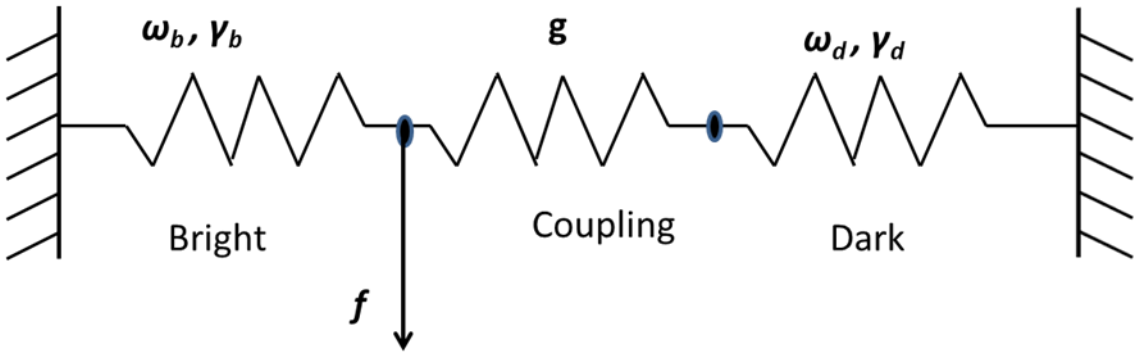

Figure III-7: Schematic of the classical model used to obtain lineshape of the Fano resonance.

In terms of these fundamental parameters, the Fano resonance line shape can be expressed as

$$F = A\frac{(\kappa + q)^2 + b}{\kappa^2 + 1} \tag{3.12}$$

where A is a constant (scale factor) and κ is the reduced frequency given by

$$\kappa = \frac{(\omega^2 - \omega_d^2 - \omega_d\Delta)}{\Gamma} \tag{3.13}$$

Δ is the resonance shift given by

$$\Delta = \frac{(\omega_d^2 - \omega_b^2)g^2}{\omega_d|C|^2} \tag{3.14}$$

C is a constant given by

$$C = (\omega_b^2 - \omega_d^2 + i\gamma_d\omega_d) \tag{3.15}$$

As usual, Γ is the resonance width,

$$\Gamma = \frac{\gamma_b\omega_d g^2}{|C|^2} \tag{3.16}$$

q is the asymmetry parameter

$$q = \frac{(\omega_d^2 - \omega_b^2)}{\omega_d\gamma_d} \tag{3.17}$$

And finally, b is the screening parameter

$$b = \frac{\gamma_d^2 q^2}{\Delta^2} \tag{3.18}$$

In Fig. III-8, we plot F as a function of ω where F is determined by Eqn. (3.12)-(3.18) for the following parameters: the bright resonance frequency was chosen to be 10 rad/s and the damping was chosen to be 1 Hz, the dark resonance frequency was chosen to be 10.1 rad/s and the damping was chosen to be 0.01 Hz and the proportionality constant was chosen to be unity. The calculations were performed for three different values of coupling strength g = 1, 2 and 4. Compared with the

Lorenztian lineshapes plotted in Fig. III-6, the Fano resonance lineshapes are seen to be highly asymmetric. In addition, increasing the coupling strength broadens the curves as well as shifts the resonant frequency. This agrees with the Eqn. (3.16) and (3.14) which show that the damping and resonance shift are proportional to the square of coupling strength. The Fano resonance is seen to be very sensitive to the coupling strength between the bright and dark modes. In plasmonic nanostructures, coupling strength is engineered by varying the gaps.

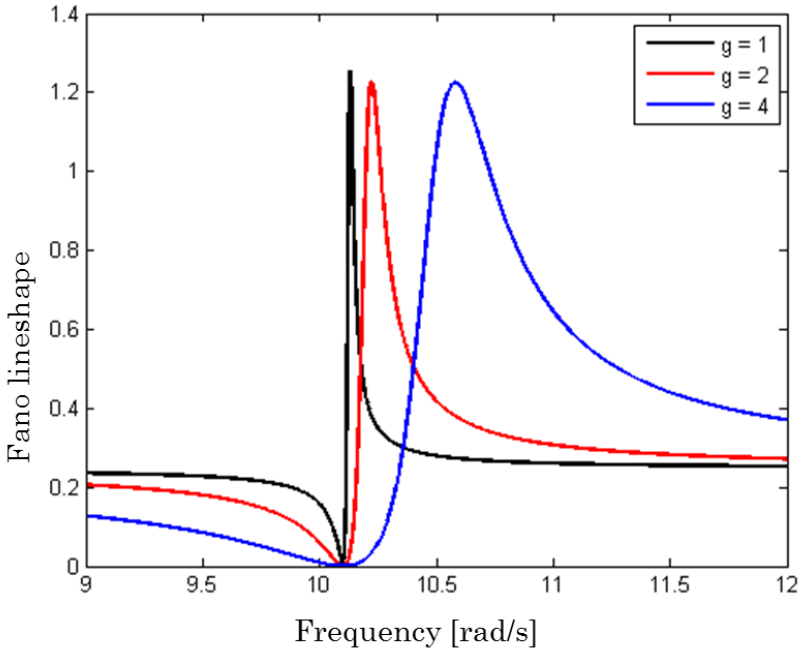

Figure III-8: Plots of Fano resonance line shapes for various coupling strengths.

C. Fano resonance in tunable plasmonic nanostructures

Complex metallic nanostructures support a collective surface plasmon resonance. In this system, the surface plasmon resonances of constituent elements couple together to form collective modes delocalized over the entire structure. The behavior of the collective plasmon modes depends strongly on the details of the

nanostructure, opening new opportunities to investigate the interaction between plasmonic nanostructures and also to engineer the nature of the resonance for various applications, for example, in sensing and nonlinear devices. Much of the current research has been directed towards metal nanoparticle aggregates in which the nanoparticle size, spacing between the nanoparticles, and symmetry of the aggregate could lead to different coupled plasmon modes [91-98]. The high sensitivity to the structural parameters is of special interest because it makes the system an excellent candidate for mechanically tunable devices. Structural tuning by mechanical stress is a natural way to achieve wide tunability in artificial electromagnetic materials, which derive their properties from structural design. Mechanical tuning has been applied to photonic crystals, which exhibit many novel properties stemming from their periodicity [99]. Recently, tunable negative index imaging by a flexible photonic crystal has been reported [100]. Similar strategies have also been applied to metamaterials in which plasmonic nanostructures were subject to mechanical stress to tune their resonances and thereby achieve a tunable metamaterial response [101]. It therefore seems only natural to explore the mechanical tuning of plasmonic nanostructures whose resonance is highly sensitive to their structural parameters, and mechanically tunable resonances have been demonstrated for a dolmen-type resonator [102] and nanoparticle dimer [103].

Fano resonances have attracted worldwide research interest recently due to their asymmetric line shape, sharp resonance, and sensitivity to a variety of parameters. Fano resonances have recently been realized in plasmonic

nanostructures and metamaterials. The reader is referred to [104] for a review of Fano resonance in plasmonic nanostructures. Due to its narrow linewidth and high sensitivity to structural and environmental parameters, Fano resonance has great potential for photonic applications such as sensing [105]. A heptamer is one of the reported plasmonic nanostructures that support a Fano resonance [94-98] and it is predicted to exhibit a very large Fano resonance spectral shift upon tuning of the surrounding media's refractive index [97]. Like the plasmonic dimers discussed earlier, Fano resonance in a heptamer is also highly sensitive to the gaps between the metal nanoparticles and the symmetry of the heptamer [97]. Therefore, the heptamer structure is a good candidate to demonstrate a tunable Fano resonance through refractive index tuning, structural tuning, and symmetry tuning. Refractive index tuning is limited by the small range of attainable refractive index changes, while mechanical tuning, which can tune the gaps between metal nanoparticles and the symmetry of the heptamer, can produce much wider tunability and is capable of tuning structural parameters and symmetry simultaneously. Symmetry breaking is of particular interest, as it could not only lead to resonance frequency shifts but also alter the fundamental characteristics of the modes, leading to dramatic changes in the optical properties. In this chapter, we discuss the Fano resonances in plasmonic heptamer structures fabricated on flexible polymers.

From the previous discussion on dimer system, it is obvious that increasing the number of particles within the plasmonic nanostructure would lead to a very

complicated mode structure. This is akin to the formation of molecules from individual atoms. Hence, the plasmonic nanostructure could be thought of as an artificial electromagnetic molecule. The spectrum of such a molecule would consist of many modes, both bright and dark. In addition, suitable engineering of the structure could lead to mode interactions thereby either creating new modes or extinguishing existing modes. As discussed earlier, dark modes have vanishingly small dipole moments and hence are not strongly excited by incident plane waves. Therefore, numerical simulation techniques such as finite element method (FEM) and finite difference time domain (FDTD) might not be able to excite the dark modes using plane waves.

Alternately, the eigenmodes of the structure could be obtained in the static limit by solving the boundary integral eigenvalue equations for the charge distribution [106, 107]. In addition, the symmetry of the heptamer structure would suggest that group representation theory could be used to correlate the symmetry of the system with that of the eigenmodes and thereby index the eigenmodes of the heptamer system. However, since this approach is valid only in the static limit, it cannot properly describe the retardation effects that must be taken into account in a system with size larger or comparable to λ. However, numerical simulation techniques such as FEM, FDTD and generalized multiparticle Mie (GMM) theory [108] do take into account the retardation effects and hence used as complementary approaches along with the electrostatic method. Description of the group theory techniques used to study the symmetry of the heptamer eigenmodes are beyond the

scope of this thesis and the readers are referred to [109] for further information and the nomenclature used.

The boundary integral eigenvalue approach is briefly described. Consider a system composed of an arbitrary array of N nanoparticles, the surface charge distribution $\sigma^j(\vec{r})$ of its j^{th} surface plasmon mode satisfies the boundary integral eigenvalue equation [106, 107]

$$\sigma^j(\vec{r}) = \frac{\lambda^j}{2\pi} \oint \sigma^j(\vec{r_q}) \frac{\vec{r} - \vec{r_q}}{\left|\vec{r} - \vec{r_q}\right|^3} \cdot \hat{n} S_q \tag{3.19}$$

where the integral is over the whole surfaces of the N nanoparticles and $\hat{n}$ is the unit vector normal to the surfaces of the N particles at point $\vec{r}$. The eigenvalue λ^j determines the system resonance frequency ω_j through the electric permittivity $\varepsilon(\omega)$ of the array by the relationship

$$Re\{\varepsilon(\omega_j)\} = \varepsilon_b \frac{1 + \lambda^j}{1 - \lambda^j} \tag{3.20}$$

where, ε_b is the electric permittivity of the medium surrounding the nanoparticles. The eigenfunction $\sigma^j(\vec{r})$ describes the self-sustained surface charge distribution of the j^{th} mode of the system. By solving eigenvalue Eqn. (3.19) numerically, we obtain the charge distribution on the heptamer structure which then allows for analysis of the symmetry of the modes.

All the fabricated heptamer structures share common fabrication procedures and are briefly discussed. The heptamers were fabricated by an electron-beam lithography and lift-off process. The fabrication procedure started with a silicon wafer with a 100 nm chromium film thermally evaporated on it. The chromium

serves as a protection layer for the PDMS membrane during the silicon dry etch process, preventing overetching and reducing undesirable cracks in the PDMS membrane. A bilayer of a polymethyl methacrylate (PMMA) resist and copolymer was coated on top of the chromium layer, and electron beam lithography was carried out to define the heptamer structure. Gold was then thermally evaporated onto the patterned resist, and the final gold heptamer structure was obtained by lift-off. A monolayer of (3-mercaptopropyl-) trimethoxysilane (MPTS) was deposited on the gold surface to function as an adhesion promotion layer and to improve contact between gold and PDMS. PDMS with a thickness of 850 μm was spin-coated on the heptamer structure to completely cover the heptamer structure and was cured at 100 °C for 2 hours. Finally, the silicon substrate was completely dry etched by SF_6-based reactive ion etching, leaving the heptamer embedded PDMS membrane with chromium protection layer at the bottom. After removal of 100 nm chromium layer, a completely freestanding PDMS membrane with the embedded heptamer structure was obtained.

D. Fano resonance in circular heptamer

The gold heptamer structure was composed of seven gold nanocylinders embedded in a flexible polydimethylsiloxane (PDMS) membrane. Thanks to the high elasticity of the PDMS membrane, the gaps between the gold nanocylinders could be accurately tuned by mechanically stretching the PDMS membrane, leading to tuning of the Fano resonance. The gold heptamer was designed to have seven gold nanocylinders with a diameter of 150 nm and height of 80 nm. The gap

between cylinders was designed to be 30 nm. For reliable optical characterizations, large arrays of gold heptamers were fabricated covering an area of 400 × 400 μm^2.

Fig. III-9 (a) shows a schematic diagram of a free-standing PDMS membrane with an embedded array of heptamers. Scanning electron microscopy (SEM) confirmed that high-quality heptamers were successfully fabricated with structural parameters close to the design values. Figs. III-9 (b-d) show the SEM images of the fabricated heptamer array. From the high magnification SEM image shown in Fig. III-9 (c), the diameter of the gold cylinder was measured to be 147 nm. Fig. III-9 (c) also shows that the heptamer structure was fabricated in such a way that its vertical dimensions were 3.7% smaller than the design values. As a result, the gaps between the cylinders were 33 nm along the horizontal direction and 28 nm along the diagonal. The heptamers were subsequently stretched along the horizontal direction shown in Fig. III-9 (c). The optical extinction spectra were taken for two orthogonal polarizations: parallel and perpendicular to the direction of mechanical stress. The original heptamer structure is isotropic and thus should exhibit identical spectra for the two polarizations. However, due to the slight anisotropy of the actual fabricated heptamer, there was a slight shift in spectra for the two orthogonal polarizations.

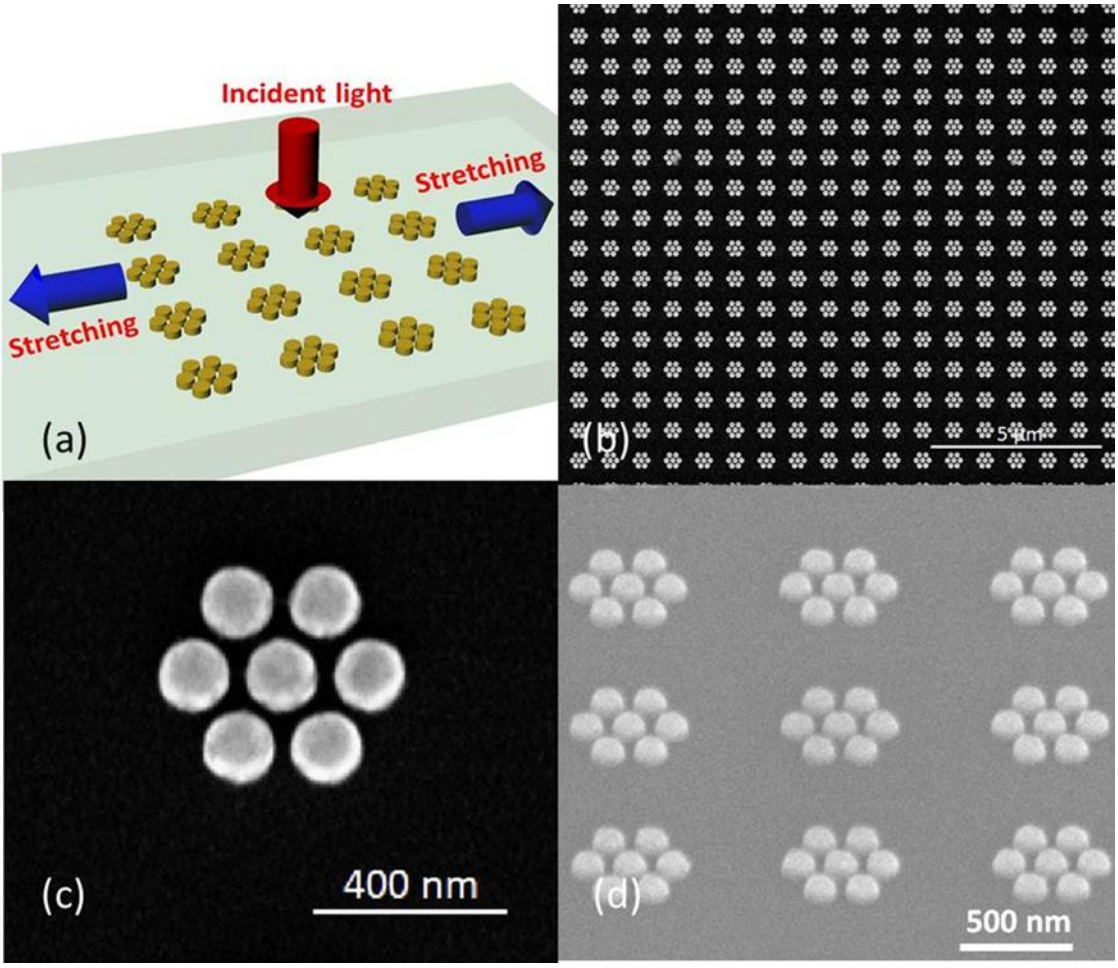

Figure III-9: Schematic showing arrays of gold heptamer structures embedded in PDMS substrate (b) Low magnification SEM image showing arrays of gold heptamers (c) High magnification SEM image showing top view of single gold heptamer (d) Tilted view of gold heptamer

As shown in Fig. III-10, the position of the Fano resonance, which presented itself as a dip in the extinction spectrum, was 829 nm for the *x* polarization, while the *y* polarization showed a dip at 838 nm. To confirm the small split was due to the imperfect fabrication, which resulted in 3.7% smaller dimensions along the *y* direction, numerical simulations using the commercial software COMSOL were

carried out. Fig. III-10 shows that the simulations accounting for the vertical shrinkage in the actual fabricated structure precisely reproduced the Fano resonance positions of experimentally measured spectra. Overall, the agreement between the simulation and experiment was excellent.

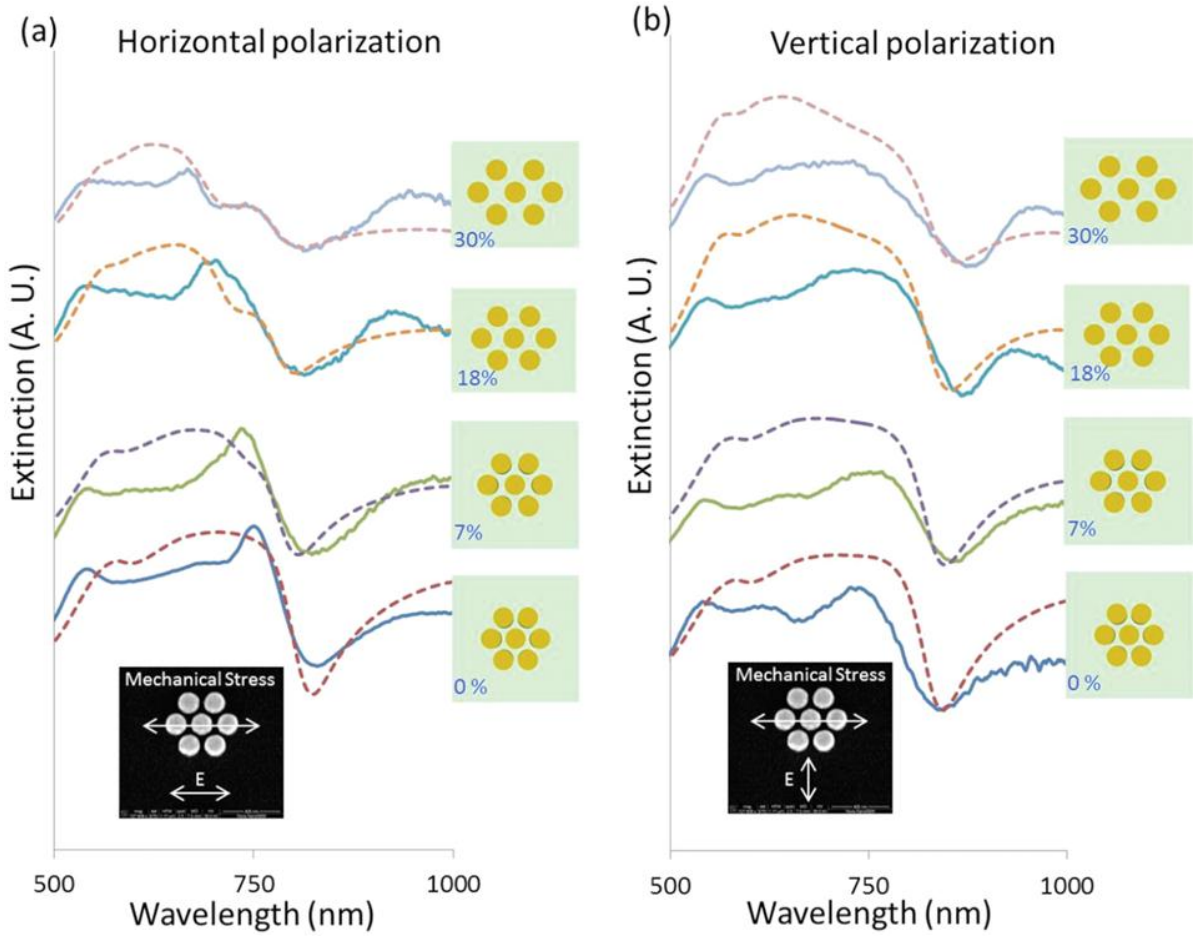

Figure III-10: Experimentally measured and simulated extinction spectra for mechanical stress along the horizontal direction with (a) horizontal polarization (b) vertical polarization of incident light

The mechanical stress lowers the symmetry and lifts the degeneracy, producing distinct behaviors for the two mutually orthogonal polarizations. Fig. III-10 (a)

shows experimentally measured and simulated extinction spectra at the induced mechanical strain values of 0%, 7%, 18%, and 30% with polarization parallel to the mechanical stress (*x* direction), as indicated in the inset of Fig. III-10 (a). The Fano resonance exhibited a moderate blue shift from 829 to 814 nm. Here, the mechanical strain is defined as the percent change in the center-to-center spacing between adjacent gold cylinders along the *x* direction. The strain values were measured indirectly by recording the changes in the length of the heptamer array, which could be directly imaged by optical microscopy and these strain values were used for numerical simulations. Fig. III-10 (b) shows the experimental and simulation spectra for the polarization perpendicular to the mechanical stress. In this case, the Fano resonance redshifted significantly from 838 to 874 nm. In addition to the spectral shifts in the opposite directions, the extinction spectra for the *x* polarization showed an additional feature at a shorter wavelength when the heptamer is under mechanical stress. This feature is noticeable at all strain values in simulations and also visible in experimental spectra for strain values of 18% and 30%. In contrast, this feature is clearly absent in all simulated and experimental spectra for *y* polarizations.

To gain insight into the observed behavior, we analyze the symmetry of the eigenmodes obtained from the boundary integral eigenvalue calculations. The heptamer structure has the symmetry of point group D_{6h}. Consequently, the eigenmodes can be indexed by the irreducible representations of D_{6h}. As per conventional nomenclature of irreducible representations (detailed in [109]), *A* and

B always refer to one-dimensional representations, *E* refers to two-dimensional representations and *T* refers to three-dimensional representations. The subscripts *g* and *u* indicate odd and even representations under symmetry. Each representation is associated with certain transformation properties which guide the symmetry behavior of the representation. The transformation properties of all irreducible representations within a given point group are summarized in a character table found in all texts on group representation theory. For example, Appendix C of [109] presents the character table for all 32 crystallographic point groups. The eigenmodes (charge distribution) of the heptamer structure are indexed by the irreducible representations of the point group D_{6h}. The transformation and hence symmetry properties of each eigenmode can then be found from the corresponding entry in the character table.

Assuming the modes are excited by normally incident light with definite in-plane polarization, only the optically active in-plane modes are considered. Among the irreducible representations of D_{6h}, only E_{1u} has a net dipole moment and thus optically active. Furthermore, we consider only the two lowest energy E_{1u} modes in the unstressed gold heptamer structure as all higher order modes are masked off by strong absorption by gold. In the first column of Fig. III-11, we show the charge distribution of the two lowest energy E_{1u} modes in an unstressed gold heptamer structure composed of seven identical gold spheres where the sphere diameter is 150 nm and gap between the spheres is 25 nm. Here the modes shown in Fig. III-11 (a, b) belong to the lowest energy E_{1u} mode, and (d) and (e) to the second lowest E_{1u}

mode. The E_{1u} irreducible representation is a two-dimensional representation, and thus the E_{1u} modes are doubly degenerate with two orthogonal states having a net dipole moment in the *x* and *y* directions, respectively.

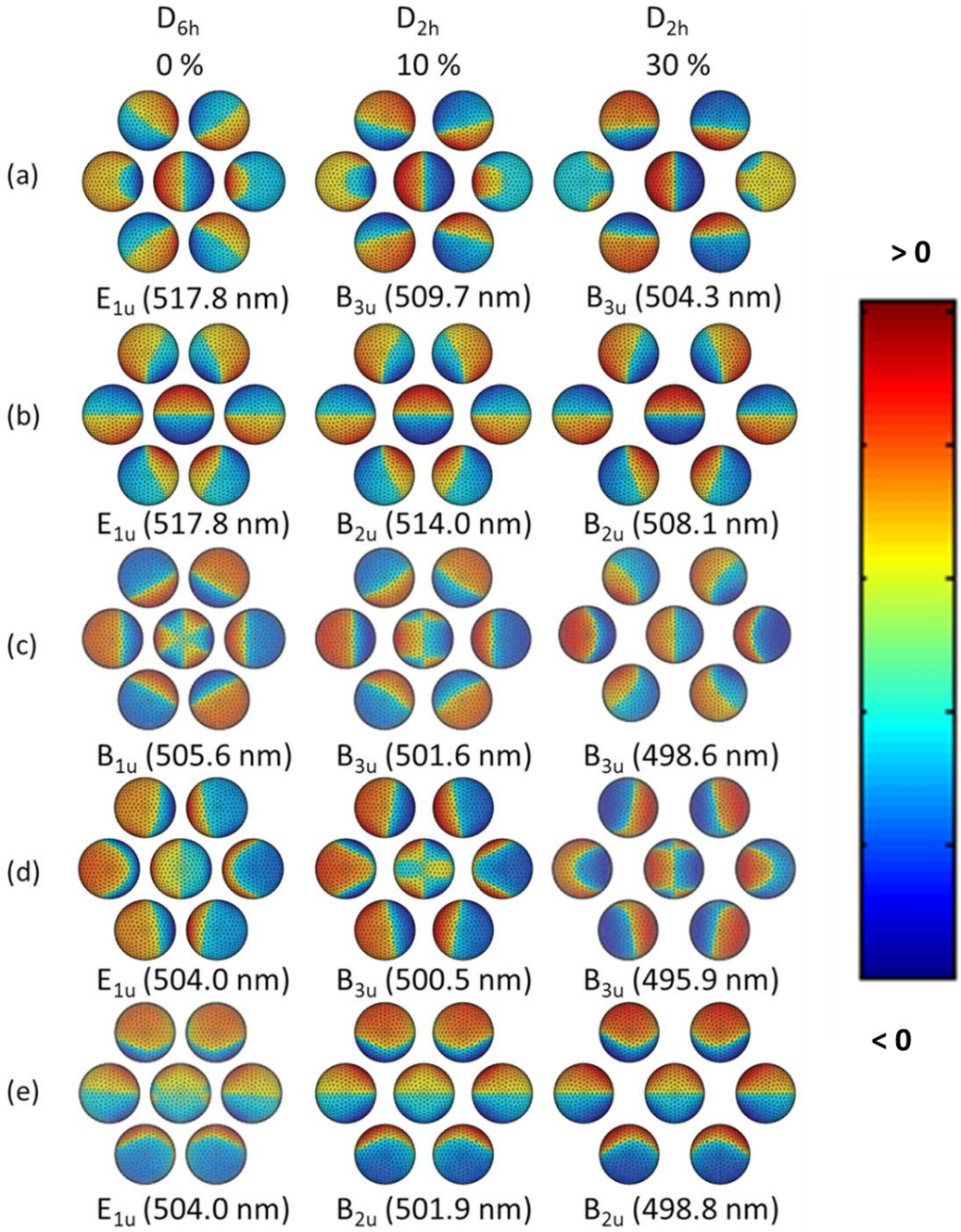

Figure III-11: Evolution of charge distribution in circular heptamer with uniaxial stress along the x direction.

Accordingly, the four charge distributions shown in the first column of Fig. III-11 possess a net dipole moment where (a) and (d) are *x*-dipoles and (b) and (e) are *y*-dipoles. Depending on the energy and the relative alignment of the dipole moment of the center sphere to those of the six satellite spheres, the E_{1u} modes can be classified as dark or bright modes. The lower energy E_{1u} mode shown in Fig. III-11 (a, b) is a dark mode where the dipole moment of the center particle aligns against the dipole moments of satellite particles, making the total dipole moment small. On the other hand, the higher energy E_{1u} mode shown in Fig. III-11 (d, e) is a bright mode where the dipole moments align together and add up. The energies of these two E_{1u} modes were found to be 2.394 and 2.459 eV or 517.8 and 504.0 nm, respectively. These mode energy values would be accurate only for heptamers made of very small nanoparticles, as the boundary integral eigenvalue calculations are valid in the static limit only. For larger sizes, retardation effects will shift and broaden the modes. The resultant overlap and interference between the two modes lead to a Fano resonance. The bright mode will broaden much more significantly than the dark mode, resulting in a Fano resonance that manifests itself in the form of a dip in the extinction spectrum, as observed in Fig. III-10.

When the heptamer is under uniaxial mechanical stress, the symmetry of the system is lowered to D_{2h}. The doubly degenerate E_{1u} mode splits into two non-degenerate modes belonging to B_{2u} and B_{3u} irreducible representations of the point group D_{2h}. Fig. III-11 shows the evolution of charge distribution as the mechanical stress is applied along the *x* direction. It clearly shows the original doubly

degenerate modes split into *x*-dipole (B_{3u}) and *y*-dipole (B_{2u}) modes. Remarkably, the nature of the modes is mostly preserved. That is, the bright E_{1u} mode splits into bright B_{2u} and B_{3u} modes, while the dark E_{1u} mode spawns dark B_{2u} and B_{3u} modes. Also, all modes shift to shorter wavelengths with increasing mechanical strain values. However, the B_{3u} modes, which have dipole moment along the direction of mechanical stress, shift more than the B_{2u} modes with dipole moment perpendicular to the mechanical stress. This leads to the polarization dependence, as the B_{3u} modes interact with *x*-polarized light and B_{2u} with *y*-polarized light. Therefore, as the heptamer is stretched along the *x* direction, *x*-polarized light would show resonance features in the shorter wavelengths than the *y*-polarized light. Even when the retardation effects are included and the resonance peaks broaden and shift, this general behavior survives and leads to the experimental observation seen in Fig. III-10.

The scattering spectra for *x* polarization also show an additional dip at shorter wavelengths. The additional dip is apparent in the spectra for 18% and 30% strain for *x* polarization but is clearly missing in all spectra for *y* polarization. This can be explained by observing that the optically inactive B_{1u} mode in the unstressed heptamer becomes an optically active B_{3u} mode under uniaxial stress along the *x* direction. As shown in Fig. III-11 (c), the charge distribution plots reveal that this B_{3u} mode is also a dark mode where the dipole moment of the center sphere aligns antiparallel against those of the satellite spheres, thereby producing a second Fano dip in the scattering spectra. In contrast, there are no other modes of the unstressed

heptamer evolving into the B_{2u} mode within the wavelength range investigated, and thus we do not see any additional dip for the *y* polarization. Further details on the circular heptamer can be found in [110].

E. Fano resonance in nanorod heptamer

The tuning of Fano resonance in circular heptamer showed that optical response of the structure could be controlled by symmetry tuning of the heptamer structure. The symmetry of the constituent nanoparticle could also be varied in order to achieve tuning of optical response. To maintain the D_{6h} symmetry of the heptamer, only the six satellite particle symmetries can be tuned while the center particle would still need to be a circular nanocylinder. In circular nanoparticles, the dipole mode is doubly degenerate while this degeneracy is lifted in nanorods due to the inherent anisotropy of nanorods. This is shown schematically in Fig. III-12 where the white colored arrows represent the radial modes and gold colored arrows represent azimuthal modes. Therefore, we analyze heptamer structures composed of hexagonal arrangement of nanorods around a central circular nanoparticle as shown in Fig. III-12. Irrespective of the rod orientation, the eigenmodes of the nanorod heptamer structure can still be indexed by the irreducible representations of D_{6h} as they still maintain the D_{6h} symmetry. We study the azimuthal nanorod structure with the orientation of the nanorods shown in Fig. III-12.

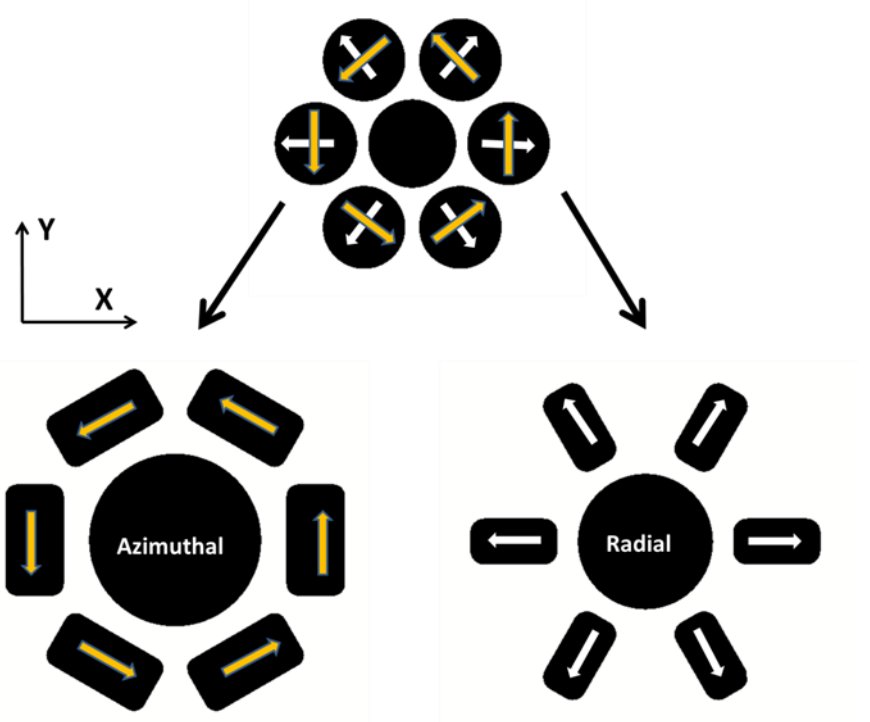

Figure III-12: **S**chematic showing the splitting of doubly degenerate modes in circular heptamer to azimuthal and radial modes in nanorod heptamer.

The gold heptamer structure was composed of six gold nanorods surrounding a central nanocylinder and the heptamer was designed to be embedded in a flexible membrane. Similar to the circular heptamer, the gaps between the gold nanoparticles could be accurately tuned by mechanically stretching the PDMS membrane, leading to tuning of the Fano resonance. The azimuthal gold heptamer was designed to have six gold nanorods, each with a length of 95 nm, width of 50 nm and gold thickness of 40 nm. The center nanocylinder was designed to have a diameter of 147 nm and gold thickness of 40 nm. The gap between the edges of center nanocylinder and nanorod was designed to be 22 nm.

Extinction and absorption cross-sections were calculated from COMSOL simulations of the nanorod heptamer with the structural parameters given above. In the simulations, the heptamers were stretched along the horizontal (*x*-axis) direction shown in Fig. III-12. The extinction and absorption spectra were calculated for two orthogonal polarizations: parallel and perpendicular to the direction of mechanical stress. Like in circular heptamer, the mechanical stress produces distinct behaviors for the two mutually orthogonal polarizations. Fig. III-13 shows simulated extinction and absorption spectra at the induced mechanical strain values of 0 %, 13 %, 26 %, and 42 %. Fig. III-13 (a, b) plots the extinction and absorption spectra with polarization parallel to the mechanical stress (*x* direction). The Fano resonance exhibited a moderate blue shift from 745 to 700 nm. Fig. III-13 (c, d) plots the extinction and absorption spectra with polarization perpendicular to the mechanical stress (*x* direction). The Fano resonance is found to slightly red shift from 745 to 760 nm.

In addition to the spectral shifts in the opposite directions, the absorption spectra for both the parallel and perpendicular polarization showed additional features at shorter wavelengths when the heptamer was under mechanical stress. This feature is noticeable at strain values of 26 % and 42 % and can be clearly observed from the absorption spectra plotted in Fig. III-13 (b, d) for parallel and perpendicular polarization respectively. In both the absorption spectra for parallel and perpendicular polarization, there appears a small absorption peak at $\lambda \sim 520$ nm and this corresponds to the characteristic transverse resonance of the localized

surface plasmon associated with the width of the gold nanorod and therefore this resonance is ignored. In addition, the absorption spectra for perpendicular polarization showed a feature at roughly 620 nm for mechanical at strain values of 26 % and 42 %.

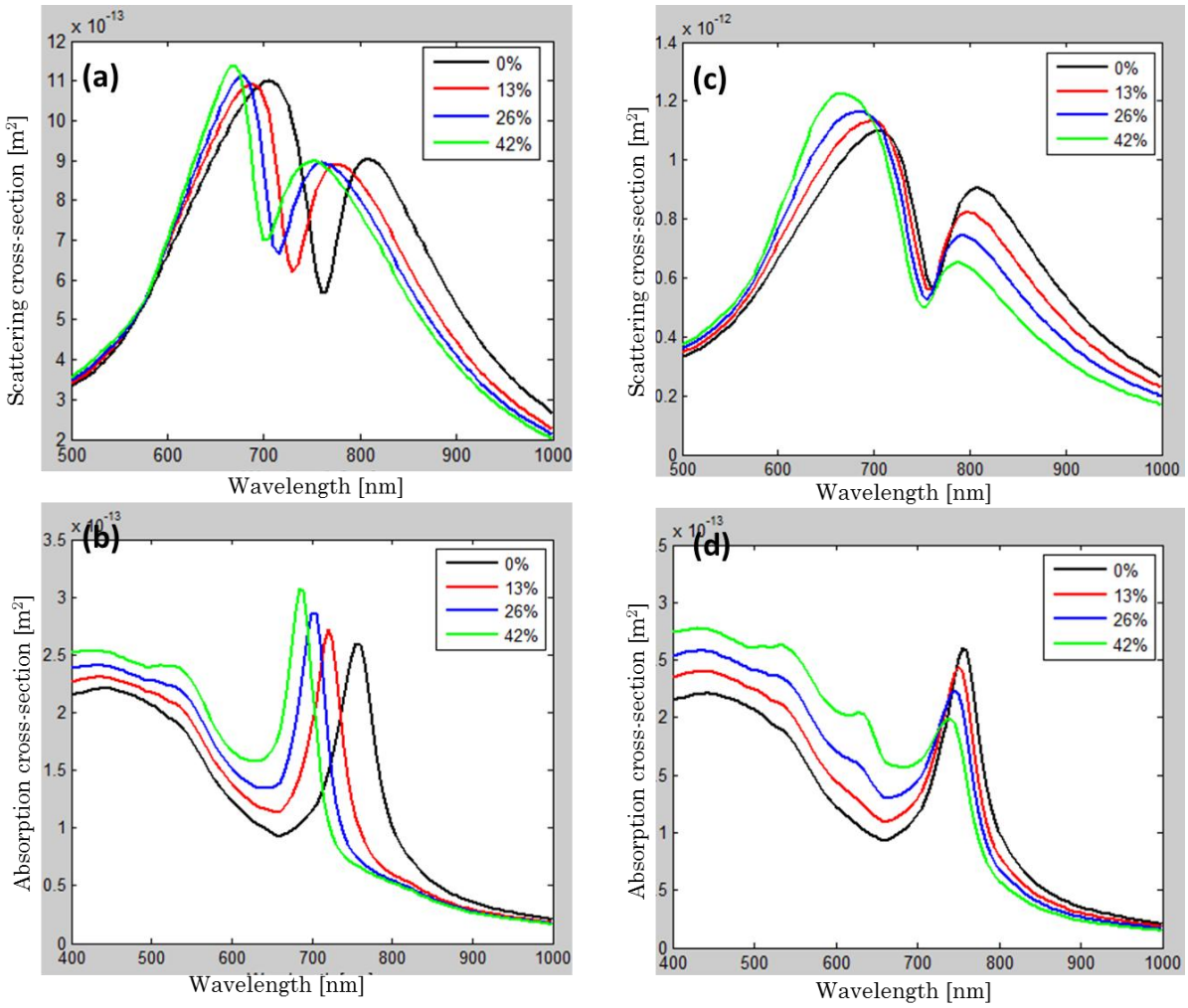

Figure III-13: Simulated extinction and absorption spectra for the azimuthal nanorod heptamer. (a) and (c) plot the extinction spectra for parallel and perpendicular polarizations respectively while (b) and (d) plot the absorption spectra for parallel and perpendicular polarizations respectively.

To gain insight into the observed behavior, we analyze the symmetry of the eigenmodes obtained from the boundary integral eigenvalue calculations. Like the circular heptamer, the nanorod heptamer structure too has the symmetry of point group D_{6h}. Assuming the modes are excited by normally incident light with definite in-plane polarization, only the optically active in-plane modes are considered. In the first column of Fig. III-14, we show the charge distribution of the two lowest energy E_{1u} modes in an unstressed gold nanorod heptamer structure with the same structural dimensions that were used in COMSOL simulations and mentioned earlier. Here, the modes shown in Fig. III-14 (a, b) belong to the lowest energy E_{1u} mode, and (d) and (e) to the second lowest E_{1u} mode.

Similar to the charge distributions obtained for the circular heptamer and plotted in Fig. III-11, the four charge distributions shown in the first column of Fig. III-14 possess a net dipole moment where (a) and (d) are y-dipoles and (b) and (e) are *x*-dipoles. The lower energy E_{1u} mode shown in Fig. III-14 (a, b) is a dark mode where the dipole moment of the center particle aligns against the dipole moments of satellite particles, making the total dipole moment small. On the other hand, the higher energy E_{1u} mode shown in Fig. III-14 (d, e) is a bright mode where the dipole moments align together and add up. This is similar to the behavior of the lower energy E_{1u} mode in the circular heptamer. In both the circular and nanorod heptamer cases, the lower energy E_{1u} mode is always a dark mode.

In the circular heptamer, the energies of the lower and higher energy E_{1u} modes were found to be 2.394 and 2.459 eV or 517.8 and 504.0 nm, respectively. In the

nanorod heptamer, the higher energy E_{1u} mode was found to be 2.134 eV or 581.0 nm. But, the energy of the lower energy E_{1u} mode seemed to depend on the orientation of the dipole. The energy of the *x*-dipole was 1.890 eV or 656 nm and the energy of the *y*-dipole was slightly lower at 1.884 eV or 658 nm.

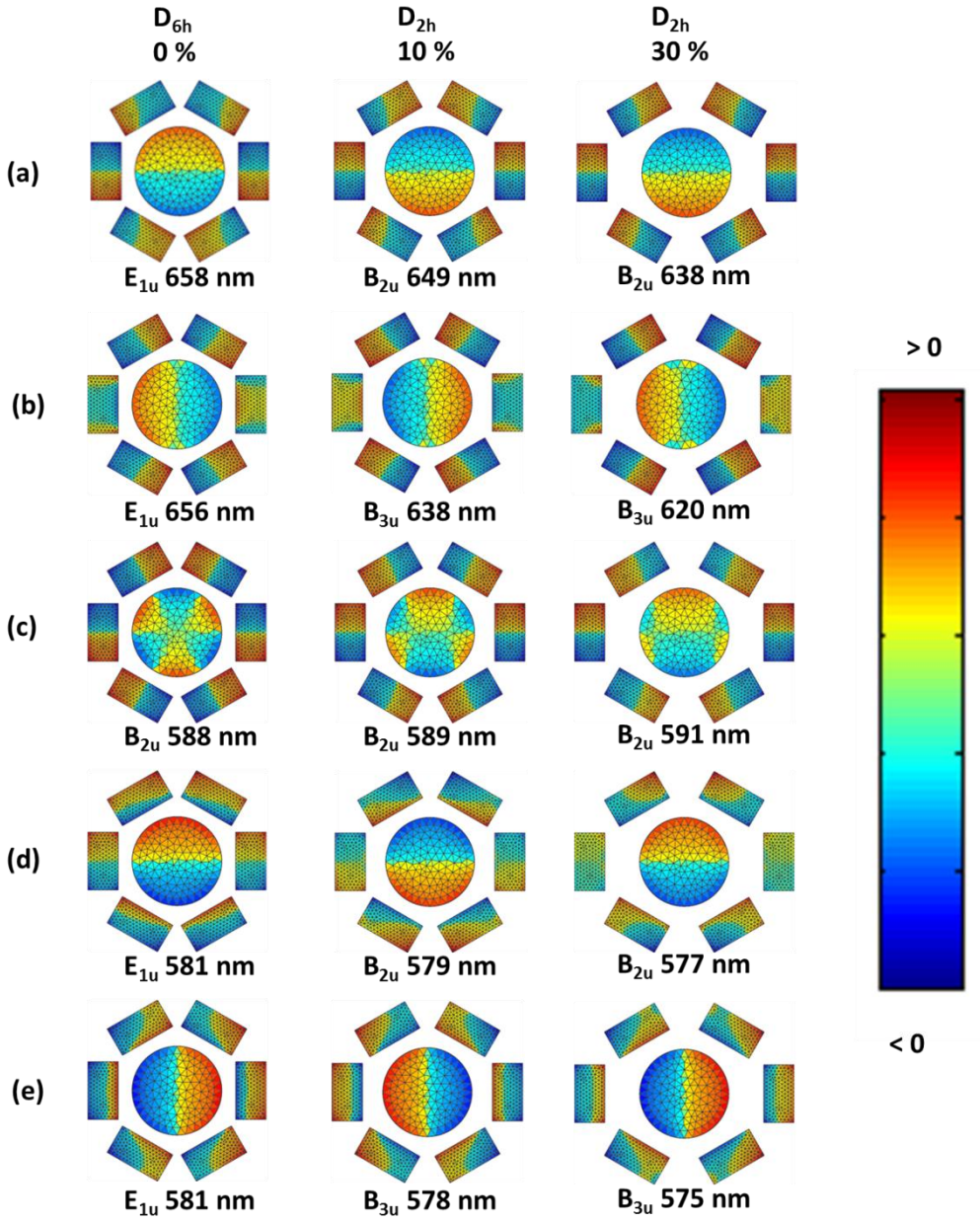

Figure III-14: Evolution of charge distribution for nanorod heptamer with uniaxial stress along the x direction.

However, from the extinction and absorption spectra plotted in Fig. III-13, the Fano resonance position coincided at 745 nm for both parallel and perpendicular polarizations. The small discrepancy in the energy could be caused due to numerical errors while computing the eigenmodes especially due to the sharp corners of the nanorods. The COMSOL simulation model avoided sharp corners by chamfering the edges of the nanorod.

The calculated mode energy values would be accurate only for heptamers made of very small nanoparticles, as the boundary integral eigenvalue calculations are valid in the static limit only. As discussed earlier, retardation effects will shift and broaden the modes for larger heptamer sizes and the resulting overlap and interference between the two modes leads to a Fano resonance. The bright mode will broaden much more significantly than the dark mode, resulting in a Fano resonance that manifests itself in the form of a dip in the extinction spectrum, as observed in Fig. III-13.

When the heptamer is under uniaxial mechanical stress, the symmetry of the system is lowered to D_{2h}. The doubly degenerate E_{1u} mode splits into two non-degenerate modes belonging to B_{2u} and B_{3u} irreducible representations of the point group D_{2h}. Fig. III-14 shows the evolution of charge distribution as the mechanical stress is applied along the *x* direction. The original doubly degenerate modes split into *x*-dipole (B_{3u}) and *y*-dipole (B_{2u}) modes and the nature of the modes is mostly preserved. That is, the bright E_{1u} mode splits into bright B_{2u} and B_{3u} modes, while the dark E_{1u} mode spawns dark B_{2u} and B_{3u} modes. This is very similar to the

behavior of Fano resonance observed in the circular heptamer under mechanical stress. Both the dark and bright B_{2u} and B_{3u} modes shift to shorter wavelengths with increasing mechanical strain values. Again, similar to the behavior observed in circular heptamer, the B_{3u} modes, which have dipole moment along the direction of mechanical stress, shift more than the B_{2u} modes, with dipole moment perpendicular to the mechanical stress. This leads to the polarization dependence similar to that observed in the circular heptamer. Even when the retardation effects are included and the resonance peaks broaden and shift, this general behavior survives and leads to the behavior of Fano resonance seen in Fig. III-13.

As mentioned earlier, the absorption spectra for *y* polarization show an additional feature at shorter wavelengths for 26 % and 42 % strain for *y* polarization only. This can be explained by observing that the optically inactive B_{2u} mode in the unstressed heptamer becomes an optically active B_{2u} mode under uniaxial stress along the *y* direction. The energy of this mode increases slightly with *x* stretching from 2.109 eV or 588 nm in the unstressed heptamer to 2.098 eV or 591 nm for the heptamer with 30 % mechanical strain. In addition, from Fig. III-14, the mode is seen to have a *y*-dipole and therefore interacts with the *y* polarization. The nanorod heptamer differs from the circular heptamer in the behavior of this optically active mode. In the circular heptamer, the optically inactive B_{1u} mode in the unstressed heptamer becomes an optically active B_{3u} mode under uniaxial stress along the *x* direction. The energy of the mode decreases under mechanical stress

and the mode is seen to have an x-dipole and thereby interacts with the x polarization.

The fabrication procedures for the nanorod heptamer were similar to those used to fabricate the circular heptamer. The targeted design took the structural parameters used to obtain the simulation results presented so far. Similar to the circular heptamer sample, a large array of gold heptamers were fabricated covering an area of 400 X 400 μm^2. Figs. III-15 (a, b) show the scanning electron micrograph (SEM) images of the fabricated nanorod heptamer array. From the high magnification SEM image shown in Fig. III-15 (b), the central nanocylinder was found to be slightly ellipsoidal in shape.

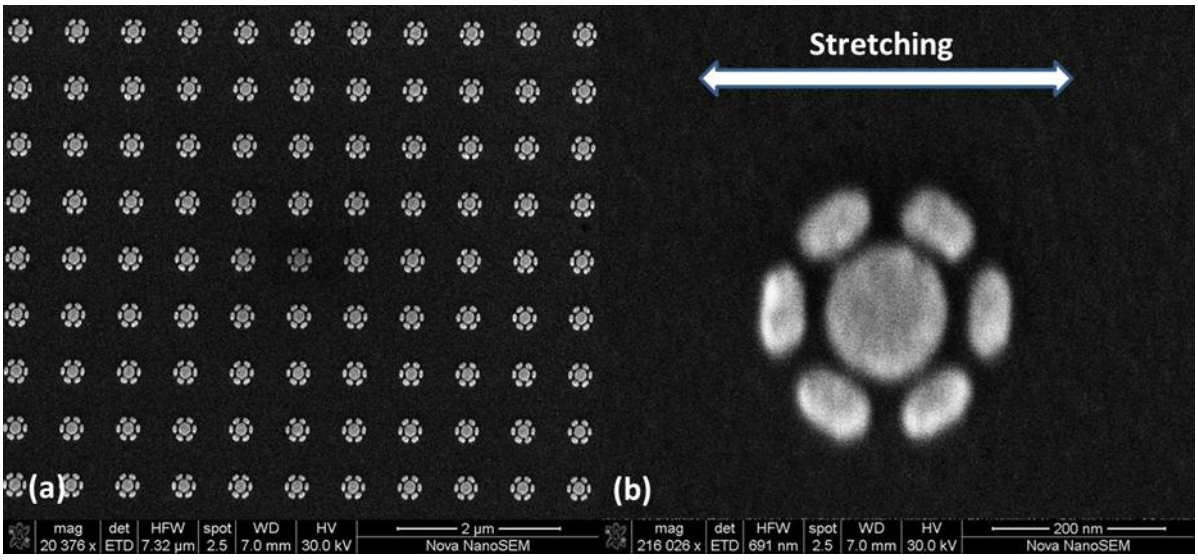

Figure III-15: Scanning electron micrographs of (a) low magnification image showing the array of gold nanorod heptamers (b) high magnification image showing the individual nanorod heptamer.

. The measured diameter along the horizontal direction was 140 nm and was 156 nm along the vertical direction. The width of all the rods was about 49 nm whereas the height varied among the rods from 100 nm to 92 nm. The gaps between the nanorods and central particle were 29 nm along the horizontal direction and 16 nm along the diagonal. The heptamers were subsequently stretched along the horizontal direction shown in Fig. III-15 (b). The optical extinction spectra were taken for two orthogonal polarizations: parallel and perpendicular to the direction of mechanical stress. The extinction spectrum for original nanorod heptamer design had strong polarization dependence as plotted in Fig. III-13. However, due to the structural variations of the actual fabricated heptamer structure, there was a shift in spectra for the two orthogonal polarizations.

As shown in Figs. III-16 (a, c), the position of the Fano resonance, which presented itself as a dip in the extinction spectrum, was 745 nm for the *x* polarization, while the *y* polarization showed a dip at 790 nm. Fig. III-16 (a) shows experimentally measured extinction spectra at the induced mechanical strain values of 0%, 10% and 20% with polarization parallel to the mechanical stress (*x* direction). The Fano resonance exhibited a moderate blue shift from 745 to 715 nm. Fig. III-16 (c) shows the experimentally measured spectra for the polarization perpendicular to the mechanical stress. The Fano resonance also exhibited a moderate blue shift from 790 to 765 nm. To confirm the small split was due to the imperfect fabrication, numerical simulations using COMSOL were performed. Fig. III-16 (b, d) shows that the simulations accounting for the fabrication imperfections

in the actual fabricated structure reproduced the Fano resonance positions of experimentally measured spectra. Overall, the agreement between the simulation and experiment was excellent.

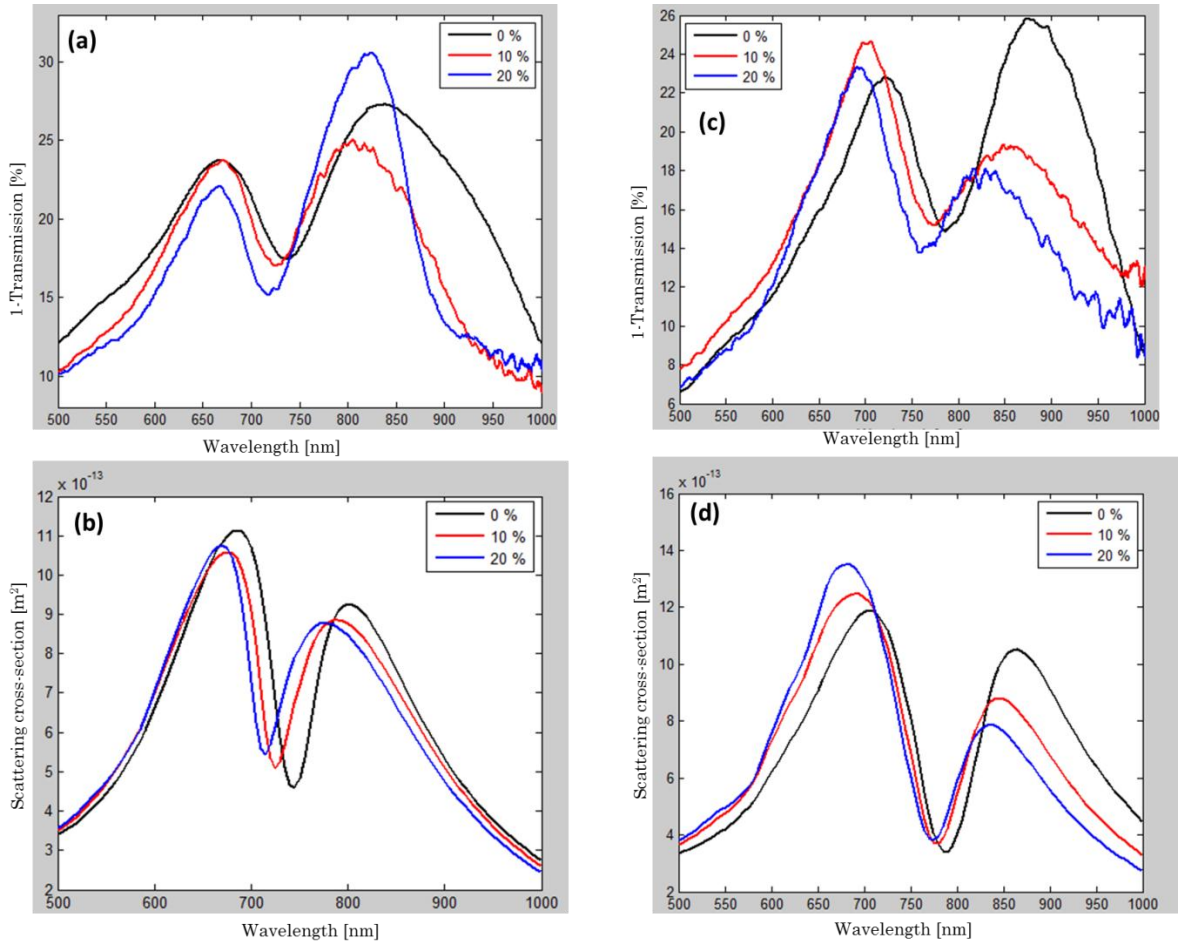

Figure III-16: Experimentally measured and simulated extinction spectra for nanorod heptamer with mechanical stress along the horizontal direction. (a) and (c) plot the experimental spectra for parallel and perpendicular polarizations and (b) and (b) plot the simulated spectra for the parallel and perpendicular polarizations.

If in the azimuthal nanorod heptamer, the nanorod orientation were to be changed from azimuthal direction to radial direction, then we could obtain the

radial nanorod heptamer structure as shown in Fig. III-12. Simulations were performed to study the optical responses of the radial nanorod heptamer for structural parameters similar to those used to fabricate the azimuthal nanorod heptamer. The structural parameters were varied widely and it was found that the radial nanorod heptamer did not support a Fano resonance for structural parameters similar to those used to fabricate the azimuthal nanorod heptamer. Extinction and absorption cross-section calculated using COMSOL simulations are plotted in Fig. III-17 for the parallel polarization of incident light. Figs. III-17 (a, b) plot the extinction and absorption cross-sections obtained from COMSOL simulations of radial nanorod heptamer structure with constant rod length of 95 nm, width of 50 nm and thickness of 40 nm. Although the diameter of the central nanocylinder was varied, the gap between the edges of nanocylinder and nanorod were kept constant at 22 nm. Despite the large variations in diameter of central nanoparticle, the radial nanorod structure does not support a Fano resonance. Figs. III-17 (c, d) plot the extinction and absorption cross-sections obtained from COMSOL simulations of radial nanorod heptamer structure with constant rod length of 95 nm, width 50 nm and gold thickness 40 nm. The gap between the nanorod and central nanoparticle were widely varied and it was found that the radial nanorod heptamer structure did not support Fano resonance.

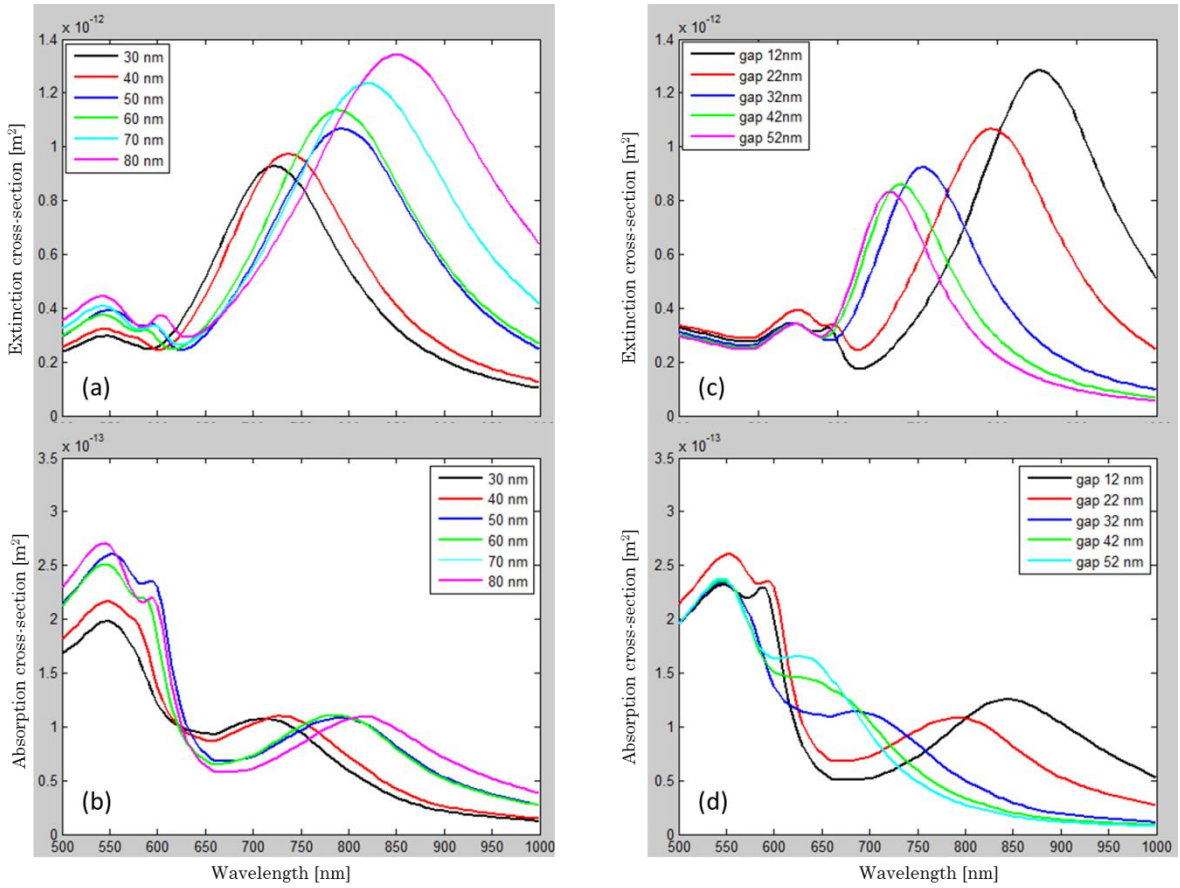

Figure III-17: Simulated extinction and absorption spectra for the azimuthal nanorod heptamer. (a) and (b) plot the extinction spectra and absorption spectra for nanorod structure with varying central nanocylinder diameter respectively while (c) and (d) plot the extinction and absorption spectra for varying gap respectively.

The observation from simulation studies were confirmed experimentally. Radial nanorod heptamer structure was fabricated with following structural parameters: rod length 105 nm, rod width 60 nm, central nanocylinder diameter 97 nm, gap 32 nm and gold thickness 40 nm. Scanning electron micrographs of the fabricated structure are shown in Fig. III-18 (b). The heptamers were subsequently stretched along the horizontal direction shown in the inset of Fig. III-18 (b) and the optical

extinction spectra were recorded for polarization parallel to direction of mechanical stress. Fig. III-18 (a) plots the measured extinction spectra for mechanical strain values of 0 %, 13 %, 21 % and 32 %. It can be observed that the radial nanorod heptamer structure did not support Fano resonance thus confirming the theoretical predictions.

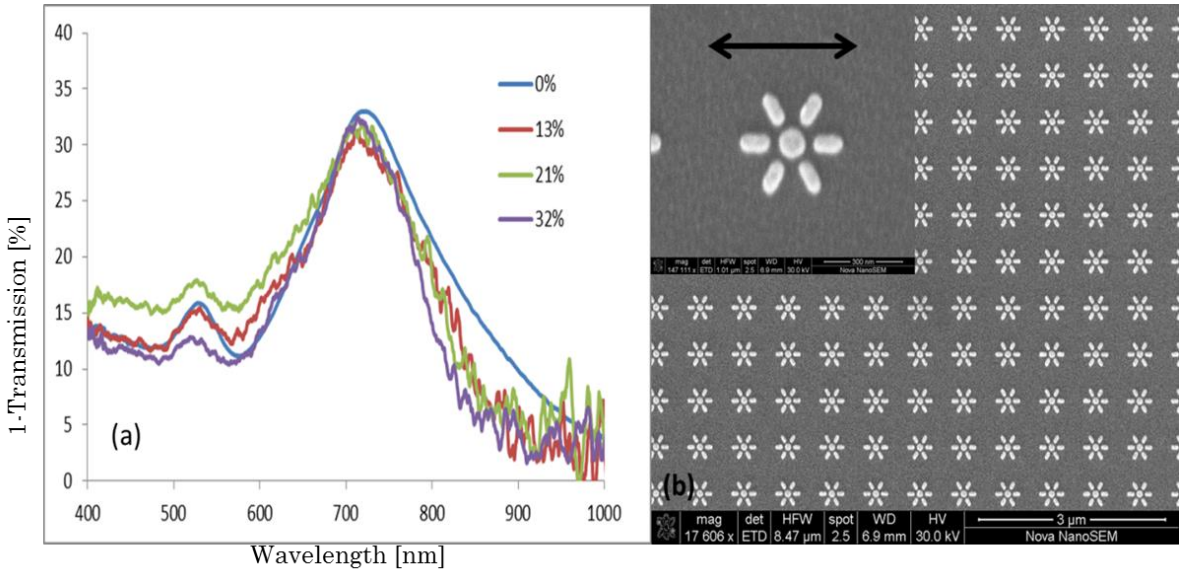

Figure III-18: (a) Plot of experimentally measured extinction spectra for parallel polarization of light (b) SEM images of fabricated radial nanorod heptamer structures with inset showing high magnification image of the nanorod structure.

As shown in Fig. III-12, the modes in the circular nanocylinder particles were decomposed into azimuthal and radial modes. Further, the inherent anisotropy of nanorods was used to split the radial and azimuthal modes in the circular heptamer structure to azimuthal and radial modes in nanorod heptamer structure. From the results presented so far, it is observed that the circular heptamer and azimuthal nanorod heptamer both support Fano resonance while the radial heptamer did not

support Fano resonance. Therefore, the resonance in the circular heptamer is composed mainly of the azimuthal component. In addition to symmetry tuning caused by mechanical stress, the Fano resonance in heptamer structures could also be tuned by engineering the orientation of the nanoparticles constituting the satellite nanoparticle structure.

Assuming an ideal heptamer structure with no fabrication defects, the doubly degenerate E_{1u} mode of the D_{6h} representation ensures that the heptamer structure exhibits identical optical responses for both the *x* and *y* polarizations thereby rendering it polarization insensitive. Therefore, the heptamer structure is an excellent candidate not only to achieve Fano resonance but also to be able to tune the Fano resonance in multiple ways (refractive index, structure and symmetry).

In conclusion, the Fano resonance in the plasmonic heptamer structures fabricated on flexible substrate was dynamically tuned by application of uniaxial stress. The various features observed in the spectra of both the unstressed heptamer and heptamer under uniaxial stress were explained using group representation theoretical methods. The Fano resonance in the unstressed heptamer was due to the interaction between the two E_{1u} modes. When uniaxial stress was applied, the shift in the Fano dip was dependent on the polarization dependence of the *x*-dipole (B_{3u}) and *y*-dipole (B_{2u}) modes. Finally, application of large mechanical stress caused the optically inactive mode to become an optically active mode and the character of this mode varied between the circular and nanorod heptamers. Except for some details, the characteristics of the Fano resonance in the

azimuthal nanorod heptamer structure are found to be qualitatively similar to the behavior of the Fano resonance in circular heptamer. Radial nanorod heptamer structure did not support a Fano resonance. These results clearly show that novel optical responses could be created by engineering of plasmonic nanostructures. Fano resonance could have potential applications in chemical and bio-sensing, optical filters, non-linear optics, fast optical switching and modulation among others.

CHAPTER IV

CONCLUSIONS AND FUTURE WORK

A. Conclusions

The rapid progress in theoretical understanding of plasmonic nanostructures coupled with advances in nanofabrication technologies has unveiled an array of interesting optical phenomena. These unusual optical phenomena could be engineered by controlling the structural geometry and symmetry in addition to the material properties of the nanostructure and its surroundings.

In this thesis, we presented a scattering cancelation device operating at 1550 nm and composed of a silicon nanorod covered by a plasmonic material. The plasmonic material was made up of eight symmetrically placed gold nano grating structure embedded in a thin film of silicon dioxide. The principle of operation of the device was analyzed using Mie theory and the influence of key parameters on the performance was discussed. The structure was fabricated using a combination of top-down nanofabrication techniques such as electron beam lithography and focused ion beam milling. The fabrication procedures were discussed and the presented scanning electron micrographs taken during various stages of the fabrication process confirmed that the dimensions of the device during each stage was close to the initial design specifications obtained from numerical simulations. In addition to the scattering cancelation sample, a control sample consisting of a bare silicon

nanorod was also fabricated. The diameter of the bare rod was measured to be 240 nm. The optical responses of the scattering cancelation device and the bare rod were directly visualized at 1550 nm using heterodyne-NSOM operating in the collection mode. The visualized optical responses consisted of interference fringes formed by the incident wave and the wave scattered by the object. The fringes were characterized by their curvature and distances from the center of the device/bare rod. The experimental data were carefully analyzed and key fringe parameters such as curvature and distance from center of device/rod agreed well with theoretical predictions extracted from numerical simulations which took into account the variations in structural dimensions due to fabrication imperfections. The results from numerical simulations also indicated that the scattering due to scattering cancelation device was suppressed by about 11 dB when compared to scattering from the bare silicon rod. The good agreement of experimental data with those obtained from numerical simulations validated the design principles and our implementation. My contribution to this work involved the design and simulations of the reduced scattering device, setup of the heterodyne NSOM system followed by optical characterization of the samples using the H-NSOM system and analysis of experimental data.

We also presented tunable Fano resonance in plasmonic nanostructures fabricated on flexible substrates and the Fano resonance was dynamically tuned by application of uniaxial mechanical stress. The plasmonic nanostructures consisted of gold heptamers whose structural parameters were obtained by performing

extensive numerical simulations using COMSOL. To complement the COMSOL simulations, eigenmodes of the structure were obtained in the static limit by solving the boundary integral eigenvalue equations for the charge distribution in the heptamer. Two different gold heptamer structures were fabricated: circular heptamer and nanorod heptamer. The circular heptamer consisted of six gold nanocylinders arranged in a hexagonal arrangement around a central gold nanocylinder. The nanorod heptamer replaced the outer six nanocylinders in the circular heptamer with nanorods while retaining the central nanocylinder. Both the circular and nanorod heptamers were fabricated using electron beam lithography and embedded into a thick PDMS membrane using procedures described in the thesis. The Fano resonances in the fabricated devices were optically characterized for various applied uniaxial mechanical stress. The spectral features that were observed in experiments were correlated with data obtained from numerical simulations and the observed spectral behaviors were explained using group theoretical methods. The experimental results agreed well with the data obtained from numerical simulations and it was shown that symmetry could be a powerful tuning mechanism in plasmonic nanostructures. The heptamer structure could be used in applications such as chemical and bio-sensing, fast optical modulators and optical filters. The unusual optical properties exhibited by plasmonic nanostructures could be combined with mechanical tunability and could serve as a platform for dynamically tunable nanophotonic devices such as sensors and tunable filters. My contribution to this work involved design and simulation studies of

circular and nanorod heptamer structures and involved in optical characterization of fabricated heptamer nanostructures.

B. Possible Future work

The research work on scattering cancelation device structure presented in this thesis clearly validates the design principles and the present implementation. However, it could be useful to calculate the scattering cross-section obtained from experimental data. In the thesis, we mentioned that the device and bare rod samples were fabricated on two different wafers. Therefore, the uncertainties in butt-coupling efficiency for the two different wafers and variations in NSOM probe collection efficiencies over multiple probes prevented us from computing the scattering cross-section from experimental data. Future work could possibly attempt to calculate the scattering cross-sections of device and bare rod from experimental data. Such a measurement could be possible if both the device and bare rod were fabricated on the same sample and illuminated by the same waveguide. For example, the input waveguide could be split into two new waveguides using a T junction and the two new waveguides could be used to illuminate the bare rod and scattering cancelation device simultaneously for the same but-coupling efficiency. If the two rods were placed close enough, then they could be visualized by NSOM in a single scan thereby enabling the accurate computation of scattering cross-sections from experimental data. In addition, the present concept could be extended to achieve practical devices such as reduced visibility detectors. For example, the silicon nanorod could be doped to create a PN

junction which could be used as an optical detector at visible frequencies. Some part of the plasmonic nanostructure (such as one of the gold grating in this case) could function as electrical contacts. By creating a row of such detectors, each tuned to a different wavelength, it might be possible to construct an on-chip spectrometer for chemical and biomedical applications.

The Fano resonance in gold heptamer structures presents excellent opportunities for practical applications in sensing and optical modulators. The addition of mechanical tuning further improves the offerings of such a structure. The gold heptamer structures could be used to implement electro-optic modulators due to the large field enhancements coupled with the narrow Fano linewidths. Due to the large field enhancement in the gaps between nanoparticles, the optical non-linearity materials such as Kerr non-linearity would be greatly enhanced. Such plasmon enhanced optical nonlinearity could be used for all optical switching and modulators. Materials exhibiting the optical Kerr effect can be characterized by their second-order nonlinear refractive index n_2. For most natural materials the value of n_2 is in the range 10^{-18} to 10^{-20} m^2/W. Therefore, in order to obtain refractive index n variations in the order of 0.01 would require large beam irradiances in the order of several hundred GW cm^{-2}. The field enhancement in most plasmonic materials is highly dependent on the gap and values of $|E/E_0|$ of several 100's could be readily achieved giving intensity enhancements in order or 10^4 to 10^5 thereby reducing the required beam irradiance or increasing the achievable refractive index variation for a fixed beam power. Compared to nanoparticle aggregate systems with

broad scattering peaks, Fano resonance has a narrow and asymmetrical linewidth thereby reducing the refractive index variations required to cause a tuning of the resonance position. In addition, Fano resonance has a lower scattering than the background ensuring higher transmitted beam power. Therefore, Fano resonance could be an ideal candidate to implement devices such as optical modulators and switches.

REFERENCES

1. D. J. Griffiths, "Introduction to Electrodynamics", 2nd Edn., Prentice-Hall, New Jersey (1989)

2. C.F. Bohren and D.R. Huffman, "Absorption and Scattering of Light by Small Particles", John Wiley & Sons, New York (1983)

3. M. Kerker, "The scattering of light, and other electromagnetic radiation", Academic Press, New York (1969)

4. E. D. Palik, "Handbook of Optical Constants of Solids" Academic Press, New York (1985

5. M. Fox, "Optical Properties of Solids", Oxford University Press, Oxford (2001)

6. P. B. Johnson and R. W. Christy, "Optical Constants of the Noble Metals", Phys. Rev. B **6**, 4370–4379 (1972)

7. A. D. Rakic, A. B. Djurišic, J. M. Elazar, and M. L. Majewski, "Optical Properties of Metallic Films for Vertical-Cavity Optoelectronic Devices," Appl. Opt. **37**, 5271-5283 (1998)

8. E. Abbe, "Beiträge zur Theorie des Mikroskops und der Mikroskopischen Wahrnehmung," Archiv für Mikroskopische Anatomie, **IX**, 413-68 (1873)

9. Lord Rayleigh, “On the theory of optical images with special reference to the optical microscope,” Phil. Mag., **5** (42), 167-195 (1896)

10. E. H. Synge, "Method for extending microscopic resolution into the ultramicroscopic region," Philosophical magazine, **6**, 356 (1928).

11. J. A. O’Keefe, "Resolving Power of Visible Light," J. Opt. Soc. Am. **46**, 359 (1956).

12. E. A. Ash and G. Nicholls “Super-resolution Aperture Scanning Microscope,” Nature **237**, 510-512 (1972).

13. D. W. Pohl, W. Denk, and M. Lanz, “Optical stethoscopy: image recording with resolution λ/20,” Appl. Phys. Lett., **44**, 651 (1984)

14. A. Lewis, M. Isaacson, A. Harootunian, “Development of a 500Å spatial resolution light microscope: I. light is efficiently transmitted through λ/16 diameter apertures,” Ultramicroscopy, **13**, 227 (1984)

15. L. Novotny and B. Hecht, “Principles of Nano-Optics,” Cambridge University Press, Cambridge (2006)

16. G. A. Valaskovic, M. Holton, and G. H. Morrison, “Parameter control, characterization, and optimization in the fabrication of optical fiber near-field probes,” Appl. Opt. **34**, 1215–1228 (1995).

17. D. R. Turner, "United States patent 4,469,554," in AT&T Bell laboratories. Murray Hill, New Jersey, USA (1983).

18. N. Tsumori, M. Takahashi, Y. Sakuma, and T. Saiki, "Experimental study of near-field light collection efficiency of aperture fiber probe at near-infrared wavelengths," Appl. Opt. **50**, 5710-5713 (2011)

19. Nanonics Imaging Limited, Israel. [www.nanonics.co.il]

20. J.B. Pendry, D. Schurig, and D. R. Smith, "Controlling electromagnetic fields", Science, **312**, 1780–2 (2006)

21. U. Leonhardt, "Optical Conformal Mapping", Science **312**, 1777 (2006)

22. D. Schurig, J. J. Mock, B. J. Justice, S. A. Cummer, J.B Pendry, A. F. Starr, and D.R. Smith, "Metamaterial electromagnetic cloak at microwave frequencies", Science **314**, 977–80 (2006)

23. W. Cai U.K. Chettiar, A.V. Kildishev and V.M. Shalaev, "Optical cloaking with metamaterials", Nat. Photon., **1** 224–7 (2007)

24. M. Kerker, "Invisible bodies", J. Opt. Soc. Am. **65**, 376–9 (1975)

25. A. Alu and N. Engheta, "Achieving transparency with plasmonic and metamaterial coatings", Phys. Rev. E **72** 016623 (2005)

26. P. Alitalo, O. Luukkonen, L. Jylha, J. Venermo, and S. A. Tretyakov, "Transmission-Line Networks Cloaking Objects From Electromagnetic

Fields," Antennas and Propagation, IEEE Trans., vol.**56**, no.2, pp.416-424, (2008)

27. P. Alitalo, F. Bongard, Jean-Francois Zürcher, J. Mosig, and S.A. Tretyakov, "Experimental verification of broadband cloaking using a volumetric cloak composed of periodically stacked cylindrical transmission-line networks", Appl. Phys. Lett. **94**, 014103 (2009)

28. G.W. Milton and N.A. Nicorovici, "On the cloaking effects associated with anomalous localized resonance", Proc. R. Soc. A **462** 3027–59 (2006)

29. N.A.P Nicorovici, G.W Milton, R.C. McPhedran and L.C. Botten, " Quasistatic cloaking of two-dimensional polarizable discrete systems by anomalous resonance", Opt. Express **15** 6314–23 (2007)

30. G.W. Milton, M. Briane and J.R. Willis, "On cloaking for elasticity and physical equations with a transformation invariant form", New J. Phys. 8 248 (2006)

31. J. Li, and J. B. Pendry, "Hiding under the carpet: a new strategy for cloaking", Phys. Rev. Lett. **101**, 203901 (2008)

32. U. Leonhardt and T. Tyc, "Broadband Invisibility by Non-Euclidean Cloaking", Science **323**, 110–112 (2009)

33. J. Valentine, J. Li, T. Zentgraf, G. Bartal and X. Zhang, "An optical cloak made of dielectrics", Nat. Mater. **8**, 568- 571 (2009)

34. L. H. Gabrielli, J. Cardenas, C. B. Poitras and M. Lipson, “Silicon nanostructure cloak operating at optical frequencies”, Nat. Photon. **3**, 461-463 (2009)

35. J. H. Lee, J. Blair, V. A. Tamma, Q. Wu, S. J. Rhee, C. J. Summers and W. Park, “Direct visualization of optical frequency invisibility cloak based on silicon nanorod array”, Optics Express **17**, 12922-12928 (2009)

36. V. A. Tamma, J. Blair, C. J. Summers, and W. Park, "Dispersion characteristics of silicon nanorod based carpet cloaks," Opt. Express **18**, 25746-25756 (2010)

37. H. F. Ma and T. J. Cui, “Three-dimensional broadband ground-plane cloak made of metamaterials”, Nature Communications **1**, 1-6 (2010).

38. T. Ergin, N. Stenger, P. Brenner, J. B. Pendry and M. Wegener, “Three-Dimensional Invisibility Cloak at Optical Wavelengths”, Science **328**, 337-339 (2010)

39. M. Gharghi, C. Gladden, T. Zentgraf, Y. Liu, X. Yin, J. Valentine, and X. Zhang, “A Carpet Cloak for Visible Light”, Nano Letters **11** (7), 2825-2828 (2011)

40. B. Zhang, Y. Luo, X. Liu, and G. Barbastathis, “Macroscopic Invisibility Cloak for Visible Light”, Phys. Rev. Lett., **106**, 033901 (2011)

41. X. Chen,Y. Luo, J. Zhang, K. Jiang, J.B. Pendry and S. Zhang, "Macroscopic Invisibility Cloaking of Visible Light", Nat. Comm., **2**, 176 (2010)

42. H. Chew and M. Kerker, "Abnormally low electromagnetic scattering cross sections," J. Opt. Soc. Am. **66**, 445-449 (1976)

43. J.-C, Sureau, "Reduction of scattering cross section of dielectric cylinder by metallic core loading," Antennas and Propagation, IEEE Trans. , vol.**15**, no.5, pp.657-662, (1967)

44. W.K. Kahn and H. Kurss, "Minimum-scattering antennas", IEEE Trans. Antennas Propag. **13** 671–5 (1965)

45. P.S. Kildal, A.A. Kishk and A. Tengs, "Reduction of forward scattering from cylindrical objects using hard surfaces", IEEE Trans. Antennas Propag. **44** 1509–20, (1996)

46. A. Alu and N. Engheta, "Plasmonic materials in transparency and cloaking problems: mechanism,robustness, and physical insights", Opt. Express **15** 3318–32, (2007)

47. A. Alu and N. Engheta, "Cloaking and transparency for collections of particles with metamaterial and plasmonic covers", Opt. Express **15** 7578–90, (2007)

48. A. Alu and N. Engheta, "Multi-frequency optical invisibility cloaks with layered plasmonic shells", Phys. Rev. Lett. **100** 113901, (2008)

49. E. Kallos, C. Argyropoulos, Y. Hao, and A. Alu, "Comparison of frequency responses of cloaking devices under non-monochromatic illumination", Physical Review B, Vol. **84**, No. 4, 045102, (2010)

50. S. Tricarico, F. Bilotti1, A. Alu, and L. Vegni, "Plasmonic cloaking for irregular objects with anisotropic scattering properties", Phys. Rev. E **81**, 026602 (2010)

51. M. Silveirinha, A. Alu, and N. Engheta, "Cloaking Mechanism with Antiphase Plasmonic Satellites", Physical Review B, Vol. **78**, 205109, (2008)

52. A. Alu, N. Engheta, "Cloaking a Sensor", Phys. Rev. Lett. **102**, 233901 (2009)

53. A. Alu, N. Engheta, "Cloaking a receiving antenna or a sensor with plasmonic metamaterials", Metamaterials, Vol. **4**, Iss. 2–3, pp.153-159, (2010)

54. A. Alu and N. Engheta, "Cloaked near-field scanning optical microscope tip for noninvasive near-field imaging,". Phys. Rev. Lett. **105**, 263906 (2010)

55. F. Bilotti, S. Tricarico, F. Pierini, and L. Vegni, "Cloaking apertureless near-field scanning optical microscopy tips", Opt. Lett. **36**, 211-213 (2011)

56. S. Tricarico, F. Bilotti, and L. Vegni, "Reduction of optical forces exerted on nano-particles covered by scattering cancellation based plasmonic cloaks," Physical Review B, **82**, 045109 (2010)

57. M. G. Silveirinha, A. Alù, and N. Engheta, "Parallel Plate Metamaterials for Cloaking Structures," Phys. Rev. E **75**, 036603 (2007)

58. M. G. Silveirinha, A. Alu, and N. Engheta, "Infrared and optical invisibility cloak with plasmonic implants based on scattering cancellation", Phys. Rev. B **78**, 075107 (2008)

59. B. Edwards, A. Alu, M. G. Silveirinha, and N. Engheta, “Experimental Verification of Plasmonic Cloaking at Microwave Frequencies with Metamaterials”, Phys. Rev. Lett. **103**, 153901 (2009)

60. D. Rainwater, A. Kerkhoff, K. Melin, J. C. Soric, G. Moreno and A. Alu, “Experimental verification of three-dimensional plasmonic cloaking in free-space”, New J. Phys. **14**, 013054, (2012)

61. F. Bilotti, S. Tricarico and L. Vegni, “Electromagnetic cloaking devices for TE and TM polarizations”, New J. Phys. **10**, 115035, (2008)

62. F. Bilotti, S. Tricarico and L. Vegni, "Plasmonic Metamaterial Cloaking at Optical Frequencies," Nanotechnology, IEEE Trans., vol.**9**, no.1, pp.55-61, (2010)

63. A. Monti, F. Bilotti, and A. Toscano, "Optical cloaking of cylindrical objects by using covers made of core–shell nanoparticles," Opt. Lett. **36**, 4479-4481 (2011)

64. S. Muhlig, M. Farhat, C. Rockstuhl, and F. Lederer, “Cloaking dielectric spherical objects by a shell of metallic nanoparticles”, Phys. Rev. B **83**, 195116 (2011)

65. J. Brown, “Artificial dielectrics having refractive indices less than unity”, Proc IEE, **100**,51–62, (1953)

66. W. Rotman, “Plasma simulation by artificial dielectrics and parallel-plate media”, IRE, Trans Antennas Propag **10**,82–95 (1962)

67. K.E. Golden, “Plasma simulation with an artificial dielectric in a horn geometry”, IEEE, Trans Antennas Propag **13**:587–594 (1965)

68. J.B. Pendry, A.J. Holden, W.J. Stewart and I. Youngs, “Extremely low frequency plasmons in metallic mesostructures”, Phys Rev Lett **76**:4773–4776, (1996)

69. E.F. Kuester and C.L. Holloway, "Comparison of approximations for effective parameters of artificial dielectrics," Microwave Theory and Techniques, IEEE Trans., vol.**38**, no.11, pp.1752-1755, (1990)

70. J. Valentine, J. Li, T. Zentgraf, G. Bartal, and X. Zhang, “An optical cloak made of dielectrics”, Nature Mater. **8**, 568–571 (2009)

71. W.C.L. Hopman, et al., “Focused ion beam milling strategies of photonic crystal structures in silicon”, in Proc. ECIO2007, Copenhagen, Denmark, April 2007, paper FA2.

72. Private Communication with MicroChem Corp., USA (http://www.microchem.com/)

73. J. Shamir, Optical Systems and Processes, PP.161, SPIE Press, Bellingham, (1999)

74. J. B. Pendry, L. Martin-Moreno, and F. J. Garcia-Vidal, “Mimicking Surface Plasmons with Structured Surfaces,” Science **305**, 847–848 (2004)

75. A. Hibbins, B. Evans, and J. Sambles, “Experimental Verification of Designer Surface Plasmons,” Science **308**, 670–672 (2005).

76. C. R. Williams, S. R. Andrews, S. A. Maier, A. I. Fernndez-Domnguez, L. Martn-Moreno, and F. J. Garca-Vidal, “Highly confined guiding of terahertz surface plasmon polaritons on structured metal surfaces,” Nat. Photonics **2**, 175–179 (2008).

77. S. A. Maier, S. R. Andrews, L. Mart´in-Moreno, and F. J. Garc´ia-Vidal, "Terahertz Surface Plasmon-Polariton Propagation and Focusing on Periodically Corrugated Metal Wires," Phys. Rev. Lett. **97**, 176,805-1–4 (2006).

78. H. Raether, "Surface plasmons on smooth and rough surfaces and on gratings", Vol. 111, Springer tracts in modern physics, Springer, Berlin, (1988)

79. S.A. Maier, "Plasmonics: fundamentals and applications", Springer, Berlin, (2007)

80. E. Ozbay, "Plasmonics: Merging photonics and electronics at nanoscale dimensions", Science **311**, 189-193 (2006)

81. M. I. Stockman, "Nanoplasmonics: past, present, and glimpse into future," Opt. Express **19**, 22029-22106 (2011)

82. M. I. Stockman, "Nanoplasmonics: The physics behind the applications," Phys. Today **64**, 39–44 (2011)

83. P. Nordlander and, C. Oubre, E. Prodan, K. Li and, and M. I. Stockman, "Plasmon Hybridization in Nanoparticle Dimers", Nano Lett., **4** (5), 899-903 (2005)

84. S. Zhang, D. A. Genov, Y. Wang, M. Liu, and X. Zhang, "Plasmon-Induced Transparency in Metamaterials", Phys. Rev. Lett. **101**, 047401 (2008)

85. E. Prodan, C. Radloff, N. J. Halas and P. Nordlander, "A Hybridization Model for the Plasmon Response of Complex Nanostructures", Science **17**, Vol. 302 no. 5644 pp. 419-422, (2003)

86. U. Fano, “Effects of configuration interaction on intensities and phase shifts”, Phys. Rev. **124**, 1866–1878 (1961).

87. C. L. G. Alzar, M. A. G. Martinez, and P. Nussenzveig, “Classical analog of electromagnetically induced transparency”, Am. J. Phys. **70**, 37 (2002).

88. Y. S. Joe, A. M. Satanin, and C. S. Kim, “Classical analogy of Fano resonances”, Phys. Scr. **74**, 259 (2006).

89. B. Gallinet and O. J. F. Martin, “Ab initio theory of Fano resonances in plasmonic nanostructures and metamaterials”, Phys. Rev. B **83**, 235427 (2011)

90. V. Giannini, Y. Francescato, H. Amrania, C. C. Phillips, and S. A. Maier, “Fano Resonances in Nanoscale Plasmonic Systems: A Parameter-Free Modeling Approach”, Nano Lett. **11** (7), 2835-2840 (2011)

91. T. Pakizeh and M. Kall, “Unidirectional Ultracompact Optical Nanoantennas”, Nano Lett. **9**, 2343–2349 (2009).

92. L.V. Brown, H. Sobhani, J.B. Lassiter, P. Norlander and N.J. Halas, “Heterodimers: Plasmonic Properties of Mismatched Nanoparticle Pairs”, ACS Nano, **4**, 819–832. (2010)

93. Z. Zhang, A. Weber-Bargioni, S. Wu, S. Dhuey, S. Cabrini and P.J. Schuck, “Manipulating Nanoscale Light Fields with Asymmetric Bowtie Nano-Colorsorter”, Nano Lett. **9**, 4505–4509, (2009)

94. J. B. Lassiter, H. Sobhani, J.A. Fan, J. Kundu, F. Capasso, P. Nordlander, and N.J. Halas, “Fano Resonance in Plasmonic Nanoclusters: Geometrical and Chemical Tunability”, Nano Lett., **10**, 3184–3189, (2010)

95. M. Hentschel, M. Saliba, R. Vogelgesang, H. Giessen, A. P. Alivisatos and N. Liu, "Transition from Isolated to Collective Modes in Plasmonic Oligomers", Nano Lett., **10**, 2721–2726, (2010)

96. J.A. Fan, C.H. Wu, K. Bao, J.M. Bao, R. Bardhan, N.J. Halas, V. Manoharan, P. Nordlander, G. Shvets, and F. Cappasso, "Self-Assembled Plasmonic Nanoparticle Clusters", Science **328**, 1135–1138, (2010)

97. N.A. Mirin, K. Bao and P. Nordlander, "Fano Resonances in Plasmonic Nanoparticle Aggregates", J. Phys. Chem. A **113**, 4028–4034, (2009)

98. K. Bao, N.A. Mirin, and P. Nordlander, "Fano Resonances in Planar Silver Nanosphere Clusters", Appl. Phys. A: Mater. Sci. Process., **100**, 333–339. (2010)

99. W. Park and J.-B. Lee, "Mechanically Tunable Photonic Crystal Structure", Appl. Phys. Lett. **85**, 4845–4847 , (2004)

100. Y. Cui, V.A. Tamma, J.-B. Lee and W. Park, "Mechanically Tunable Negative-Index Photonic Crystal Lens", IEEE Photonics J., **2**, 1003–1012, (2010)

101. J. Y. Ou, E. Plum, L. Jiang, and N.I Zheludev, "Reconfigurable Photonic Metamaterials", Nano Lett. **11**, 2142–2144, (2011)

102. I.M. Pryce, K. Aydin, Y.A. Kelaita, R.M. Briggs and H.A. Atwater, "Highly Strained Compliant Optical Metamaterials with Large Frequency Tunability", Nano Lett. **10**, 4222–4227, (2010)

103. F. Huang and J.J. Baumberg, "Actively Tuned Plasmons on Elastomerically Driven Au Nanoparticle Dimers", Nano Lett. **10**, 1787–1792, (2010)

104. B. Luk'yanchuk, N.I. Zheludev, S.A. Maier, N.J. Halas, P. Nordlander, H. Giessen and C.T. Chong, "The Fano resonance in plasmonic nanostructures and metamaterials", Nat. Mater. **9**, 707– 715, (2009)

105. K.A. Tetz, L. Pang, and Y. Fainman, "High-Resolution Surface Plasmon Resonance Sensor Based on Linewidth-Optimized Nanohole Array Transmittance", Opt. Exp. **31**, 1528–1530, (2009)

106. I.D. Mayergoyz, D.R. Fredkin and Z. Zhang, "Electrostatic (Plasmon) Resonances in Nanoparticles", Phys. Rev. B **72**, 155412, (2005)

107. D.E. Gomez, K.C. Venron and T.J. Davis, "Symmetry Effects on the Optical Coupling between Plasmonic Nanoparticles with Applications to Hierarchical Structures", Phys. Rev. B **81**, 075414, (2010)

108. Y. I. Yu and B.A. Gustafson, "A Generalized Multiparticle Mie-Solution: Further Experimental Verification", J. Quantum Spectrosc. RA. **70**, 395. (2001)

109. M. Tinkham, "Group Theory and Quantum Mechanics", McGraw-Hill, New York, (1964)

110. Y. Cui, J. Zhou, V.A. Tamma and W. Park, "Dynamic tuning and symmetry lowering of Fano resonance in plasmonic nanostructure", ACS Nano, **6** (3), 2385-93, (2012)